THE FREQUENCY OF TROPICAL PRECIPITATING CLOUDS AS OBSERVED BY THE TRMM PR AND ICESAT/GLAS

A Thesis

by

SEAN PATRICK CASEY

Submitted to the Office of Graduate Studies of
Texas A&M University
in partial fulfillment of the requirements for the degree of

MASTER OF SCIENCE

August 2007

Major Subject: Atmospheric Sciences

THE FREQUENCY OF TROPICAL PRECIPITATING CLOUDS AS OBSERVED BY THE TRMM PR AND ICESAT/GLAS

A Thesis

by

SEAN PATRICK CASEY

Submitted to the Office of Graduate Studies of
Texas A&M University
in partial fulfillment of the requirements for the degree of

MASTER OF SCIENCE

Approved by:

Chair of Committee,	Andrew E. Dessler
Committee Members,	Courtney Schumacher
	Anthony M. Filippi
Head of Department,	Richard E. Orville

August 2007

Major Subject: Atmospheric Sciences

ABSTRACT

The Frequency of Tropical Precipitating Clouds as Observed by the TRMM PR and ICESat/GLAS. (August 2007)

Sean Patrick Casey, B.S., University of Washington

Chair of Advisory Committee: Dr. Andrew E. Dessler

Convective clouds in the tropics can be grouped into three categories: shallow clouds with cloud-top heights near 2 km above the surface, mid-level congestus clouds with tops near the 0°C level, and deep convective clouds capped by the tropopause. This trimodal distribution is visible in cloud data from the Geoscience Laser Altimeter System (GLAS), carried aboard the Ice, Cloud, and land Elevation Satellite (ICESat), as well as in precipitation data from the Tropical Rainfall Measuring Mission (TRMM) Precipitation Radar (PR). Fractional areal coverage (FAC) data is calculated at each of the three levels to describe how often optically thick clouds or precipitation are seen at each level. By dividing the FAC of TRMM PR-observed precipitation by the FAC of thick GLAS/ICESat-observed clouds, the fraction of clouds that are precipitating is derived. The tropical mean precipitating cloud fraction is low: 3.7% for shallow clouds, 6.5% for mid-level clouds, and 24.1% for deep clouds. On a regional basis, the FAC maps created in this study show interesting trends. The presence of nonphysical answers in the PCF graphs, however, suggest that greater study with more precise instruments is needed to properly understand the true precipitating cloud fraction of the tropical atmosphere.

ACKNOWLEDGEMENTS

I would first like to thank my committee chair, Dr. Andrew E. Dessler, for his guidance and support, as well as his assistance in familiarizing me with the ICESat/GLAS data used in this study. Also, I'd like to thank Dr. Courtney Schumacher for her help and assistance with the TRMM PR data, as well as to thank her and Dr. Anthony M. Filippi for providing guidance as members of my thesis committee. Dr. Sun Wong provided proofreading support for the journal article that preceded this thesis, as well as the occasional insane cat picture to get me through the day.

Support for this research was received from NASA EOS/IDS grant NNG04GH67G and NASA Earth System Science Fellowship NNX06AF64H, both to Texas A&M University. Many thanks go to Janice Blum and Bridget West of the Texas A&M Research Foundation for their assistance with the ESS fellowship.

Some data used in this study were acquired as part of the Tropical Rainfall Measuring Mission (TRMM). The algorithms were developed by the TRMM Science Team and the data were processed by the TRMM Science Data and Information System (TSDIS) and the TRMM Office; they are archived and distributed by the Goddard Earth Sciences Data and Information Services Center (GES DISC). TRMM is an international project jointly sponsored by the Japan National Space Development Agency (NASDA) and the U.S. National Aeronautics and Space Administration (NASA) Office of Earth Sciences. ICESat/GLAS data were obtained from the National Snow and Ice Data Center.

Finally, I'd like to thank my family and friends, whether local, national, or international, for being my rock and my strength. I never would have made it this far without your love and support.

Some of the information contained within this thesis is also contained in an article that has been submitted with revisions to the *Journal of Geophysical Research*. This article, written with co-authors Andrew Dessler and Courtney Schumacher, should be in press within the year.

TABLE OF CONTENTS

LIST OF TABLES

LIST OF FIGURES

CHAPTER I

INTRODUCTION

The capping processes behind tropical shallow and deep convection are well documented and understood (Figure 1). Shallow convective clouds, with cloud-top heights near 2 km, are prominent in large portions of the ocean, mostly notably in the trade-wind regions outside of the Inter-Tropical Convergence Zone (ITCZ) [*LeMone and Meitin*, 1984]. Some of these clouds precipitate [*Short and Nakamura*, 2000; *Schumacher and Houze*, 2003b], but they are generally blocked from precipitation development by large-scale subsidence and the trade inversion layer present. *Johnson et al.* [1996] noted that a trade wind stable layer was seen frequently over the warm pool of the western Pacific, in conjunction with trade cumulus clouds. *Malkus and Riehl* [1964] also noted trade wind convective clouds oriented along the wind vectors in the west Pacific.

Deep cumulonimbus clouds, capped from further vertical development by the tropopause, are driven by surface-level convergence and heating in the ITCZ near the equator [*Yanai et al.*, 1973] as well as surface heating over the continents; by definition, these clouds precipitate at some stage in their evolution. Not only are these clouds important contributors to the rainfall budget of the Tropics, but their role in tropical heat and energy balance is also vital. *Riehl and Simpson* [1979] determined that around 2000

This thesis follows the style of *Journal of Geophysical Research*.

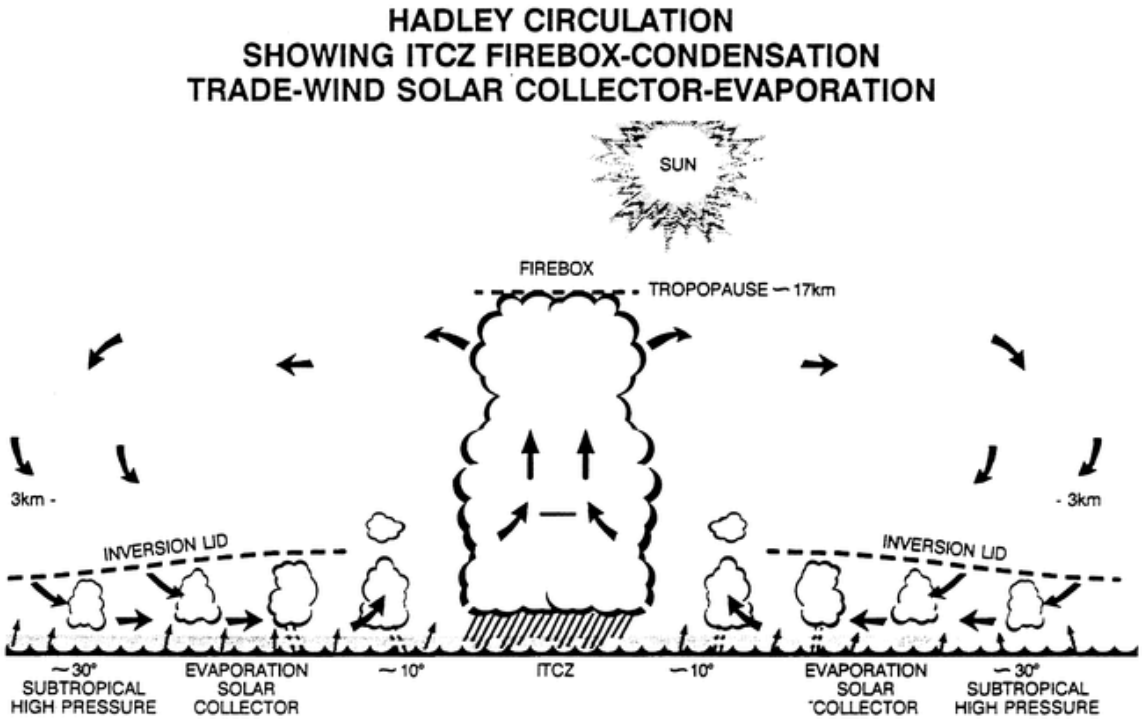

Figure 1: Bimodal view of tropical convective precipitation. From *Simpson* [1992].

of these "hot towers" are needed daily to provide the vertical transport necessary to satisfy the energy balance of the equatorial region.

While *Johnson et al.* [1999] recognized the important role that these two cloud types play in the tropical atmosphere, they also sought to bring attention to a third cloud type: cumulus congestus clouds, with cloud tops near 5 km above the surface (Figure 2). The following two sections seek to summarize the evidence for a 5 km, 0°C cloud peak as well as the possible mechanisms differentiating these clouds from shallow or deep convection.

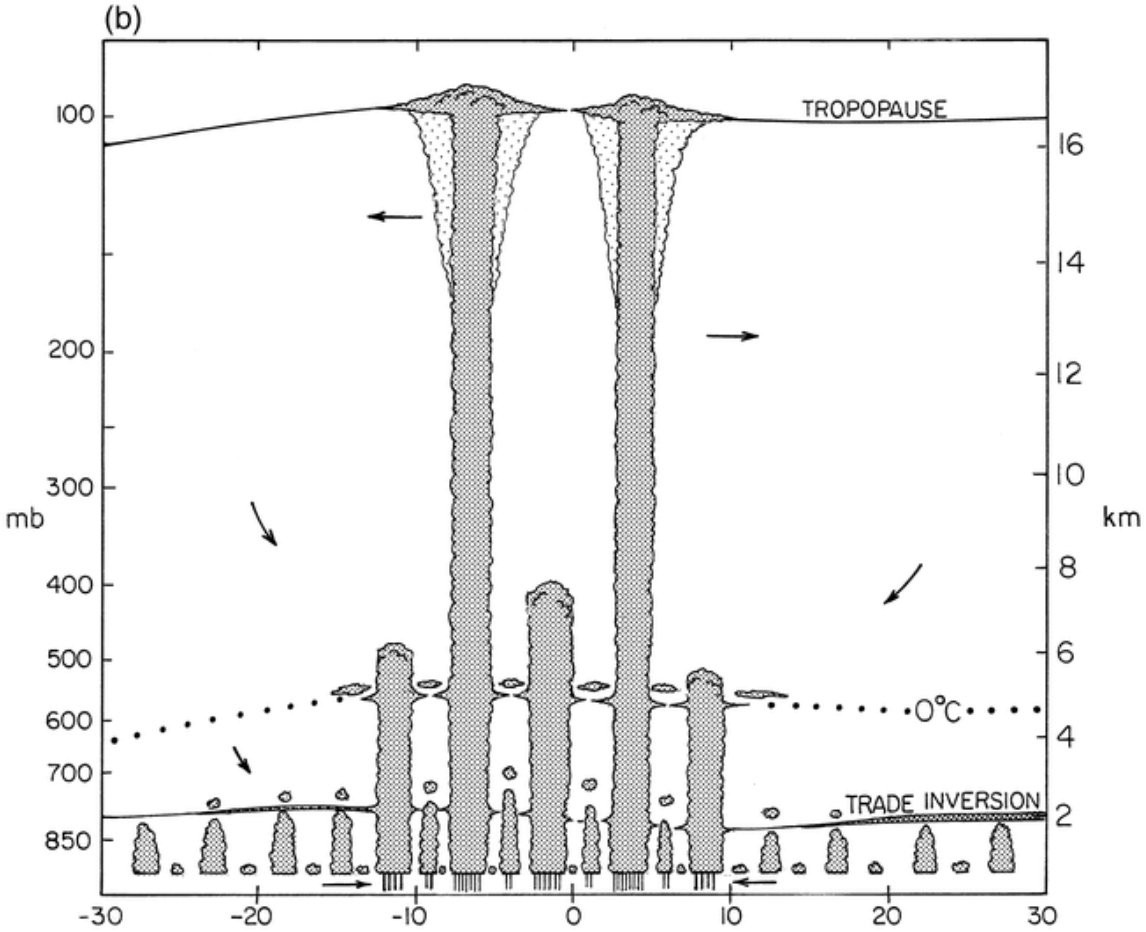

Figure 2: Trimodal view of tropical convective precipitation. From *Johnson et al.* [1999].

A. Evidence for a 0°C congestus cloud peak

Congestus clouds have been studied relatively little, but their role is important for tropical cloud and precipitation development. *Johnson et al.* [1999] noted that congestus clouds accounted for 57% of the precipitating convective clouds during the Tropical Ocean Global Atmosphere Coupled Ocean-Atmosphere Response Experiment (TOGA COARE), contributing 28% of total rainfall. The abundance of congestus clouds was also apparent within the Global Atmosphere Research Program (GARP) Atlantic

Tropical Experiment (GATE) data as well. *Houze and Cheng* [1977] noted that precipitation from areas with radar-echo tops between 4 and 9 km accounted for 45% of the total precipitation (Figure 7 of *Houze and Cheng* [1977]).

Zuidema [1998] noted that a cloud coverage minimum between 800 and 600 mb (located between the shallow and congestus cloud peaks) was common in the warm pool for all weather conditions. In terms of mesoscale precipitation features, *Malkus and Riehl* [1964] observed warm pool populations of congestus clouds moving at large angles to the low-level wind, along the mid-level shear vectors. Similar rainbands were observed during TOGA COARE by *Hildebrand* [1998]. These rainbands consisted of small convective cell clusters aligned with the 0-5 km shear vector. This suggests that mid-level flow and vertical shear is important for determining the direction of propagation of congestus clouds. In terms of seasonal variations, *Johnson et al.* [1999] found significant variance with respect to the 30-60-day intraseasonal oscillation (ISO) (also referred to as the Madden-Julian Oscillation (MJO) [*Madden and Julian*, 1994]), with high populations of congestus clouds occurring before deep convection and increased mesoscale organization.

Johnson et al. [1996] reported that congestus clouds were often associated with a stable layer near the 0°C level. This stable layer is separate from, but often coexists with, the trade stable layer mentioned earlier. As convection reached the 0°C level, high levels of detrainment and moisture profile perturbations were noted. *Hildebrand* [1998] also noted that this stable layer prevented further convection of shear-parallel rainbands and led to outflow at 5-7 km.

Congestus clouds serve a dual purpose in the atmosphere [*Johnson et al.*, 1999]. Some of these clouds, usually on the shallower end of the congestus spectrum, serve to moisten and precondition the atmosphere for deep convection. Others, the deeper congestus clouds, are significant contributors to the tropical rainfall total. Both of these groups of clouds are producers of midlevel clouds such as altostratus [*Johnson et al.*, 1996], which modulate tropical radiative heating.

Cumulus congestus clouds have moderate shortwave and longwave albedos, also making them important in terms of radiative heating balance [*Jensen and Del Genio*, 2006]. However, these clouds are not well simulated in global climate models (GCMs). The mechanisms behind cumulus congestus clouds, in terms of what limits their height, is still a topic of some debate.

B. Explanations for a 0°C congestus cloud peak

Redelsperger et al. [2002] summarized the three main explanations for the limitations on cloud-top height for cumulus congestus clouds; convective available potential energy (CAPE), melting effects at the 0°C stable layer, and dry intrusions.

1. Convective available potential energy (CAPE)

CAPE is the amount of buoyant energy available for vertical acceleration of an air parcel. Larger values of CAPE are associated with higher upper limits on updraft vertical velocity during storm growth. Thus, higher values of CAPE could be associated with higher clouds, suggesting that congestus clouds are the result of lower CAPE

values. In addition, *Lucas et al.* [1994] separated CAPE profiles into two groups: "fat" profiles with high low-level buoyancy and lower levels of neutral buoyancy, and "skinny" profiles with small buoyancy distributed through a greater depth. For congestus clouds, "fat" CAPE profiles would provide for vigorous convection, but would not rise as high in the atmosphere.

The theoretical explanations connecting CAPE to cloud-top height, however, are not matched by the data. *Redelsperger et al.* [2002] and *Jensen and Del Genio* [2006] noted only weak correlations between low-level CAPE and increasing convective cloud-top height. Thus, both studies concluded that CAPE was not a major limiting factor of congestus cloud-top height.

2. The 0°C stable layer—melting effects

Much of the work on congestus clouds in the 1990s focused on the relation between congestus clouds and a 0°C stable layer [*Johnson et al.*, 1996]. These shallow layers were marked by increased stability in the vertical temperature profile (or inversions in some cases) and a reversal in the specific humidity profile.

Johnson et al. [1996] separated these stable layers into two categories: anomalously cool-moist conditions below the 0°C level and anomalously warm-dry conditions above. The anomalously cool-moist conditions occurred within or near precipitating systems, suggesting they were caused by melting ice particles falling through the 0°C level. This cools the environment below the melting level, causing an increase in stability.

While these processes may serve to explain congestus clouds with tops below the 0°C level, they do not explain the capping process behind congestus clouds with tops above the 0°C level. *Zuidema* [1998] and *Jensen and Del Genio* [2006] noted that congestus overshooting this level could begin to glaciate, increasing parcel buoyancy due to latent heat release. This overshooting should allow the cloud to grow to the tropopause. Yet the high number of congestus clouds above the melting level suggests a different limitation on congestus cloud-top height.

3. Dry air intrusions

More recently, work has focused on the anomalously warm-dry conditions noted by *Johnson et al.* [1996]. Dry air from aloft in higher latitudes enters the Tropics and subsides in long filaments hundreds of kilometers in width. *Yoneyama and Parsons* [1999] related these intrusions to Rossby wave breaking and tracked the source back to mid-latitude baroclinic waves. *Waugh and Polvani* [2000] analyzed 20 years of meteorological data and found that intrusions from Rossby waves along the subtropical jet were frequent during the boreal winter, with eight events per winter over both the Pacific and Atlantic Oceans and six strong intrusions over the Pacific Ocean per winter. While the lower and middle atmosphere recovered to moist conditions within a week [*Parsons et al.*, 2000], the upper atmosphere remained anomalously dry for ten to twenty days.

Redelsperger et al. [2002] analyzed the effects of a dry intrusion observed during TOGA COARE using a cloud-resolving model. Following the intrusion, moisture in the

lower and middle troposphere recovered due to clouds rising into the dry air mass. Moistening occurred on the edges of the clouds due to lateral mixing. The model also showed that the most common mode of convection was congestus clouds ~4-6 km in height, and the authors related the cloud-top height to thermal inversions. Analysis of the buoyancy suggests that the dry air intrusion decreased parcel buoyancy, controlling the cloud-top. Water loading effects on cloud-top height, however, were secondary, with only a weak relationship between above-cloud relative humidity and cloud top.

Takemi et al. [2004] utilized data from the Research Vessel *Mirai* over the tropical western Pacific from 1999-2001, and analyzed the observed radiosonde profiles using a cloud-resolving model. This study also noted a strong correlation between congestus clouds and dry intrusions, with the 0°C stable layer and static stability having less of an impact.

Jensen and Del Genio [2006] studied soundings from the Atmospheric Radiation Measurement (ARM) research facility at Nauru Island and coupled these with a parcel model. This study also showed that a drying of the midtroposphere was more of a factor in limiting congestus cloud-top height than the 0°C stable layer.

C. Precipitation efficiency

Much work has focused on the geographical distribution of tropical clouds and precipitation, but little analysis has determined the fraction of clouds at each level that actually yield precipitation. While the concepts behind the main precipitation processes

are known (cloud formation, nucleation, condensation, collision, coalescence, deposition), the efficiency of clouds forming precipitate is unknown.

Braham [1952] defined precipitation efficiency as the ratio of the amount of condensed water that reaches the ground to the mass of vapor entering the cloud. He found this efficiency to be 10% for tropical thunderstorms in Florida. *Houghton* [1968] noted this low natural precipitation efficiency, while also noting that this could only be increased artificially under very specific conditions.

Hardy [1963] analyzed different drop-size distributions in order to determine which is more effective in increasing the precipitation efficiency of clouds. He used a distribution originally suggested by *Marshall and Palmer* [1948] of

$$N_D = N_0 \exp\left(-\Lambda D\right),$$

where D is drop diameter, $N_D dD$ the number of drops between D and D+dD in diameter, N_0 the value of N_D at D=0, and Λ is the slope distribution factor given by

$$\Lambda\left(R\right) = 41R^{-0.21}$$

where R is the rainfall rate. Using this distribution, he determined that distributions with a higher slope factor, similar to clouds and precipitation formed from orographic lifting, were more efficient.

More recently, *Shusse and Tsuboki* [2006] analyzed cumulonimbus clouds during the Global Energy and Water Cycle Experiment (GEWEX) Asian Monsoon Experiment (GAME) Huaihe River Basin Experiment (HUBEX) using a similar definition of precipitation efficiency to that used by *Braham* [1952], and found that less than 10% of water vapor is converted into precipitation and returned to the ground.

This thesis seeks to report on the fractional areal coverage (FAC) of both clouds and precipitation, and to use this data to determine the fraction of precipitating clouds in the Tropics on a regional basis. Chapter II describes the data and analysis methods used in this study. Chapter III looks at coincident scan data between the satellites used, to compare data that is known to be concurrent. Finally, Chapter IV computes regional FAC values, from which the precipitating cloud fraction (PCF) can be computed.

CHAPTER II

METHODOLOGY

A. Data

Cloud observations are from the Geoscience Laser Altimeter System (GLAS), carried aboard the Ice, Cloud, and land Elevation Satellite (ICESat) [*Zwally et al.*, 2003; *Spinhirne et al.*, 2005]. ICESat was launched in 2003 and is polar orbiting with an inclination of 94°. GLAS is a nadir-viewing, diode-pumped Nd:YAG laser operating in the near-infrared (1064 nm) and visible (532 nm), allowing it to view many layers of clouds, including overlapping clouds [*Mahesh et al.*, 2004; *Dessler et al.*, 2006]. *Wang and Dessler* [2006] used GLAS data to note that multilayer clouds were present nearly 35% of the time in the tropics, an important consideration when creating the algorithm for this analysis. GLAS operates at 40 pulses per second with 70-m footprints separated along the track by 170 m; in this study, I use GLAS data averaged over one-fifth second, giving the data a horizontal resolution of 1.4 km.

Precipitation data are from the Tropical Rainfall Measuring Mission's (TRMM) Precipitation Radar (PR), the first quantitative spaceborne precipitation radar [*Kummerow et al.*, 1998]. The TRMM satellite was launched in 1997 and orbits with an inclination of 35°. The PR operates at 13.8 GHz with a 5-km nadir field-of-view and a 245-km swath width during the period of interest (i.e., after the 2001 boost).

In this thesis, I will use data from GLAS (Version 26) and the PR (Version 6) obtained from 26 September to 18 November 2003 and between 20°N and 20°S. The

GLAS operates only intermittently to conserve laser performance, and this period, known as the "Laser 2A" period, contains some of the best GLAS cloud data.

B. Analysis method

For each GLAS profile, the lowest detectable cloud-top height was counted only if the underlying surface was not detected (i.e., the cloud has optical depth > 3). This was done to exclude cirrus and thin altostratus. GLAS has a vertical resolution of 76.8 m; however, the cloud heights were grouped into vertical bins of 250 m to correspond with the nadir vertical resolution of the PR. It should be noted that the vertical resolution of the PR off nadir is greater than 250 m, though this issue has a minor effect on the results of this study.

The PR 2A23 product provides echo-top height of the upper boundary of precipitation, as well as a rain-type classification, which is based on an algorithm comparing the vertical and horizontal distribution of radar reflectivity [*Steiner et al.*, 1995]; [*Awaka et al.*, 1997]. Convective rain-types are noted by large vertical and small horizontal structures of high reflectivity, whereas stratiform raintypes are identified by more horizontally homogeneous regions of weak to moderate reflectivity and often include the presence of a brightband around the melting level [*Houze*, 1981].

This analysis method requires separating precipitation events identified by the PR into stratiform and convective. Table 1 summarizes the rain-type classification by the TRMM PR. For this study, I consider rain flags of 100, 120, and 130 as stratiform precipitation, while rain flags of 200, 210, 272 and 291 are considered convective. Rain

Table 1: Definitions of TRMM PR raintype, classification and conditions according to online documentation and *Schumacher and Houze* [2003b]. The right-most column specifies the raintype's classification in terms of this paper. V=vertical structure, H=horizontal structure, BB=bright band, sf=stratiform, and conv=convective.

Raintype	**Meaning**	**Conditions**	**Classification**
100	Stratiform certain	V=sf (BB exists) H=sf	Stratiform
120	Probably stratiform	V=other (BB possible) H=sf	Stratiform
130	Maybe stratiform	V=sf (BB exists) H=conv	Stratiform
140	Maybe stratiform or maybe transition or something else	V=other (no BB) H=sf	Convective
152	Maybe stratiform	V=other H=sf Shallow non-isolated	Convective by nature, categorized as Stratiform (see Section 4)
160	Maybe stratiform, but rain hardly expected near surface	V=other (BB possible) H=sf	Discarded
170	Maybe stratiform, but rain hardly expected near surface	V=other (no BB) H=sf	Discarded
200	Convective certain	V=conv (no BB) H=conv	Convective
210	Convective certain	V=other H=conv	Convective
271	Convective	V=other H=conv Shallow isolated	Convective
272	Convective	V=other H=conv Shallow non-isolated	Convective
291	Convective	V=other H=sf Shallow isolated	Convective
300	Others	V=other H=other	Discarded
313	Others	V=other H=other Shallow isolated	Discarded

flag 152, listed as "maybe stratiform" with the designation shallow non-isolated in the online documentation, is considered convective based on the arguments in *Schumacher and Houze* [2003b] that shallow rain in the tropics is formed by warm rain processes and is therefore convective in nature. Rain flag 140 is listed as "maybe stratiform or maybe transition or something else". However, visual analysis of coincident scans (to be discussed in Section 3) showed similar structure and cloud/precipitation relations to that of convective precipitation; as such, this rain-type was considered convective for this analysis. Rain flags 160 and 170 were not included in this study, as these raintypes signify precipitation that does not reach the surface.

Figure 3a shows the fractional occurrence of lowest visible cloud-top heights as viewed by GLAS during the Laser 2a period. This data indicates a trimodal cloud-top distribution with cloud peaks at 1.5, 5.75, and 14 km, similar to the GLAS analysis of *Dessler et al.* [2006]. The PR analysis in Figure 3b shows shallow and mid-level peaks in the convective echo tops at 2 and 5.5 km; however, the deep convective precipitation peak is not clearly visible. Echo top height has been observed to be distributed lognormally [*Houze and Cheng*, 1977; *Cetrone and Houze*, 2006], such that any deep convective precipitation peak would be small regardless. In addition, due to power constraints, the PR has a minimum detectable reflectivity of ~18 dBZ post-boost [*Kummerow et al.*, 1998; *Takahashi and Iguchi*, 2004], making it difficult to sense small ice particles. By assuming that some of the shallow and mid-level echo tops correspond to deeper echo with reflectivities less than 18 dBZ, the trimodal nature of tropical precipitation is consistent with the PR data.

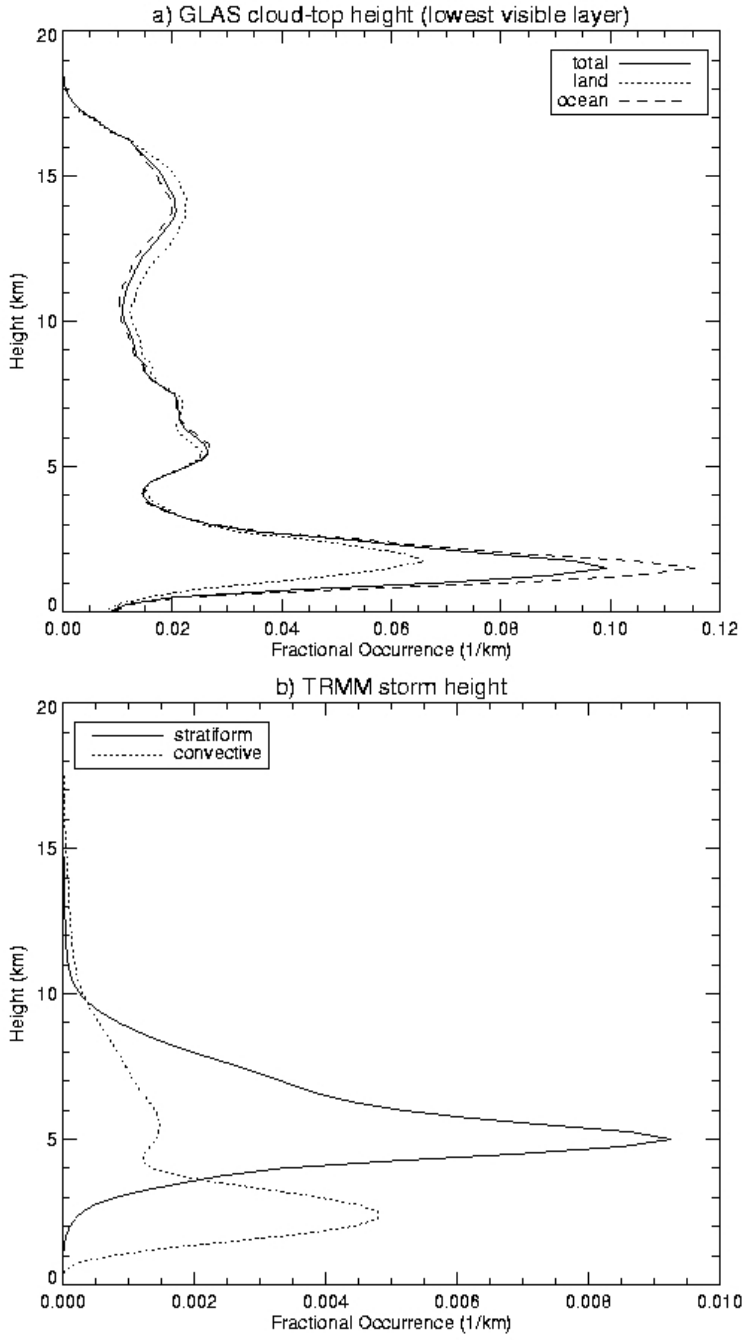

Figure 3: Fractional occurrence of a) lowest visible cloud-top heights within 0.5 km of each graphed height across the Tropics from 20°S-20°N, including separation into land and ocean, b) precipitation echo-top heights within 0.5 km of each graphed height across the same region, and c) reproduction of convective curve from 3b, with land-ocean separation included. Stratiform and convective echoes in 3b are separated using the rain-type differentiation used in the TRMM 2A23 data product with modification suggested by *Schumacher and Houze* [*Schumacher and Houze*, 2003b].

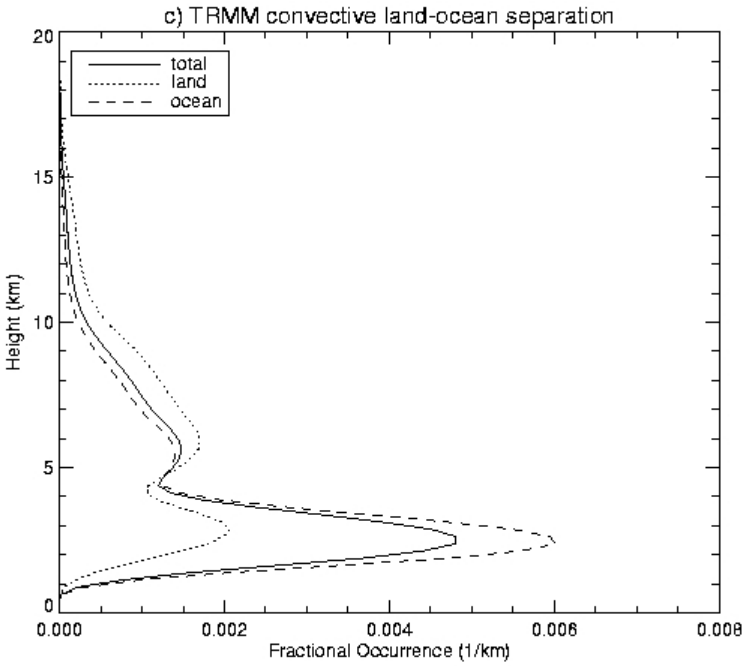

Figure 3 *(continued).*

Figure 3b also shows a sharp echo top peak near 5 km in the stratiform precipitation data, corresponding to the climatological 0ºC level in the tropics. Ice particles falling through this level aggregate and melt, greatly increasing their visibility to the PR. Large amounts of ice not visible to the PR likely populate the stratiform region above the 0°C level and would be evident with a more sensitive radar. The stratiform peak differs from the convective peak around 5.5 km in that the convective peak is assumed to more accurately represent the height of precipitate in the cloud, with little or no precipitate present above the echo-top height except in some cases of deep convection.

Figures 3a and 3c separate the cloud and convective echo-top heights, respectively, into land and ocean occurrences. In Figure 3a, it is clear that shallow clouds are more common over the oceans than the land surfaces, with smaller variations

in mid-level and deep cloud populations. Figure 3c shows that shallow precipitation is also more likely over the oceans than land, while convective mid- and upper-level precipitation is more likely over land. The separation for stratiform rain is not shown, as these curves showed little land-ocean difference.

While *Johnson et al.* [1999] did not analyze deep stratiform precipitation, it is an important component in tropical rainfall [*Schumacher and Houze*, 2003a]. In addition, on a cloud-by-cloud basis, the GLAS cloud-top heights obtained at a given time cannot be separated into convective and stratiform. Thus, this analysis must take into account stratiform precipitation to relate the precipitating cloud fraction of deep clouds properly. Shallow stratiform rain resulting from weak, large-scale lifting is rarely observed in the tropics, so the implicit assumption in this work is that all of the stratiform rain observed by the PR between 20°S and 20°N originates from deep convection (see also *Houze* [1997]).

This work attempts to compute the fraction of shallow, mid-level, and deep clouds that precipitate. It is important to note that *Johnson et al.* [1999] considers only convective clouds, which have bases at low levels. However, because of limitations in the data available, one cannot discriminate, for example, between congestus and altocumulus. Therefore, this study classifies clouds exclusively by their cloud-top height.

CHAPTER III

COINCIDENT SCAN ANALYSIS

In order to verify these assumptions regarding the correspondence between TRMM precipitation heights and GLAS cloud heights, first I analyzed coincident scans between the cloud-viewing GLAS satellite and the radar-carrying TRMM satellite. The precessional nature of the TRMM satellite's orbit allowed for near-coincident scans between the two satellites 488 times during the Laser 2a period. This thesis defines a "near-coincident scan" as a scan along the GLAS satellite path for which the TRMM PR viewed the same region on the earth's surface within ± 15 minutes. This time interval was chosen to limit inclusion of data following major changes in the local cloud and rain structure, yet also expand the possible coincident cases.

Of the 488 coincidences, GLAS detected clouds in 424 cases, and of these, the TRMM PR detected rain in 98 cases. Fifty-three of these 98 cases were located between 20°S and 20°N. Analysis was limited to that latitude range in order to remove possible contamination from mid-latitude storms. Figure 4a shows an example horizontal cross-section of the two satellite swaths obtained over the eastern Democratic Republic of the Congo on 20 October 2003. Much of the precipitation comes from storms with PR-measured heights of 5-6 km, though two large and many other small convective centers with heights greater than 10 km are also apparent. The dotted line, representing the corresponding GLAS swath, passes through one of these large convective centers.

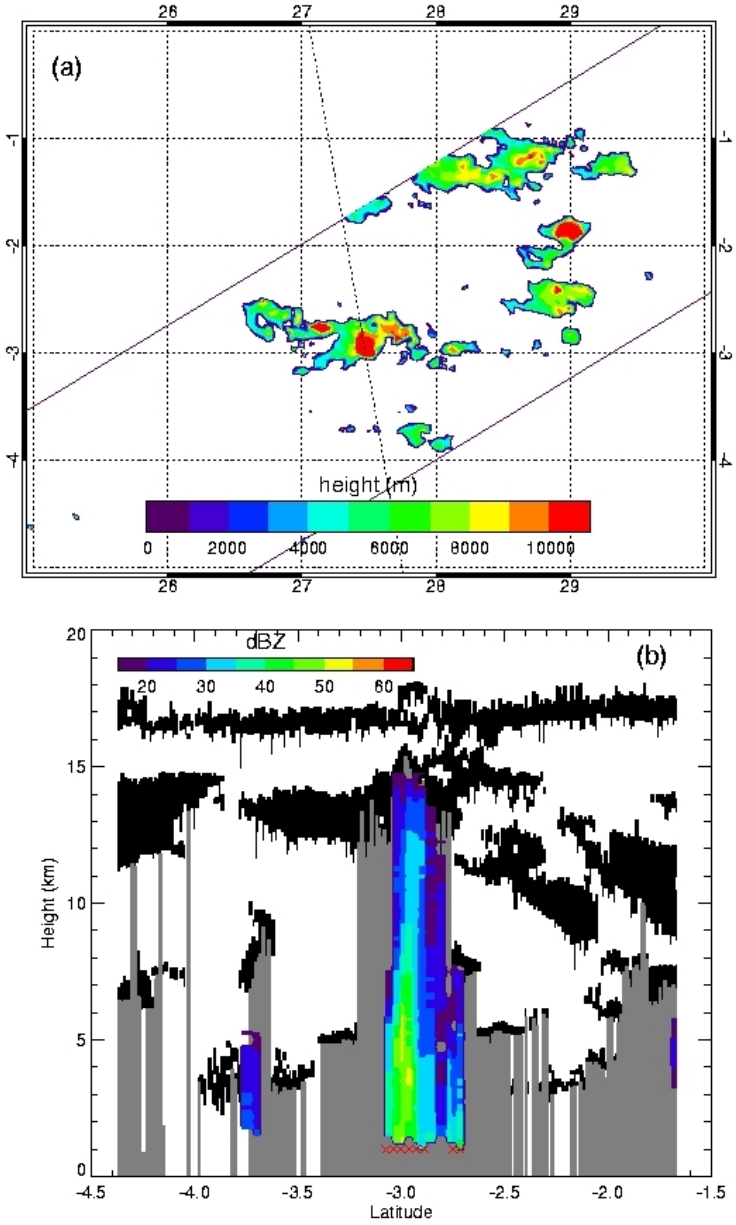

Figure 4: a) Horizontal scan and b) cross-section of a sample coincident case from 20 October 2003 over the eastern Democratic Republic of the Congo. The thick dotted line in 4a is the path of the GLAS satellite (processing south to north), and the wide horizontal path is the TRMM satellite (processing west to east). Contoured is the storm height, or the height of the precipitation as viewed by the TRMM satellite. In 4b, black areas represent clouds, and grey areas mark where the GLAS satellite returned no signal after extinguishing. Red X's below parts of the precipitation designate areas flagged by the TRMM raintype algorithm as convective precipitation, with the non-marked areas flagged as stratiform precipitation.

Figure 4b shows a vertical cross-section along the GLAS track where it coincides with the TRMM path. Throughout this particular cross-section, the height of the precipitation top is lower than the highest GLAS cloud top; this shows GLAS's higher sensitivity and ability to view multiple layers of clouds. In addition, the two areas flagged as "convective" (marked underneath by red Xs) contain precipitation heights close to those of the cloud height, whereas the three areas flagged as stratiform precipitation (unmarked) contain larger distances between the GLAS cloud top and the PR precipitation top. This is consistent with the assumption that for stratiform precipitation, GLAS will measure significantly higher clouds than the PR. In this scan, it is also clear that not every cloud pixel, even those pixels for which the GLAS laser is extinguished, contains precipitation. These particular clouds may form precipitate in the future, or may have formed precipitate in the past, but when they were scanned, no precipitation was present.

Additional coincident scans and cross-sections can be seen in the Appendix of this thesis. For the 53 coincident scans between 20°S and 20°N containing clouds and precipitation, each pixel with both cloud and precipitation reaching the ground were analyzed (Figure 5a). A peak is apparent around 5 km height in the TRMM data, while the largest peak in the GLAS data is located near 15-16 km.

Figure 5b shows histograms for the pixels flagged as stratiform by the TRMM PR algorithm. It is clear that the peaks in Figure 5a at 5 km for TRMM and 15-16 km for GLAS are due to stratiform precipitation, as the peaks in the two figures coincide. Eighty percent of GLAS cloud heights in Figure 5b are greater than 10 km in height.

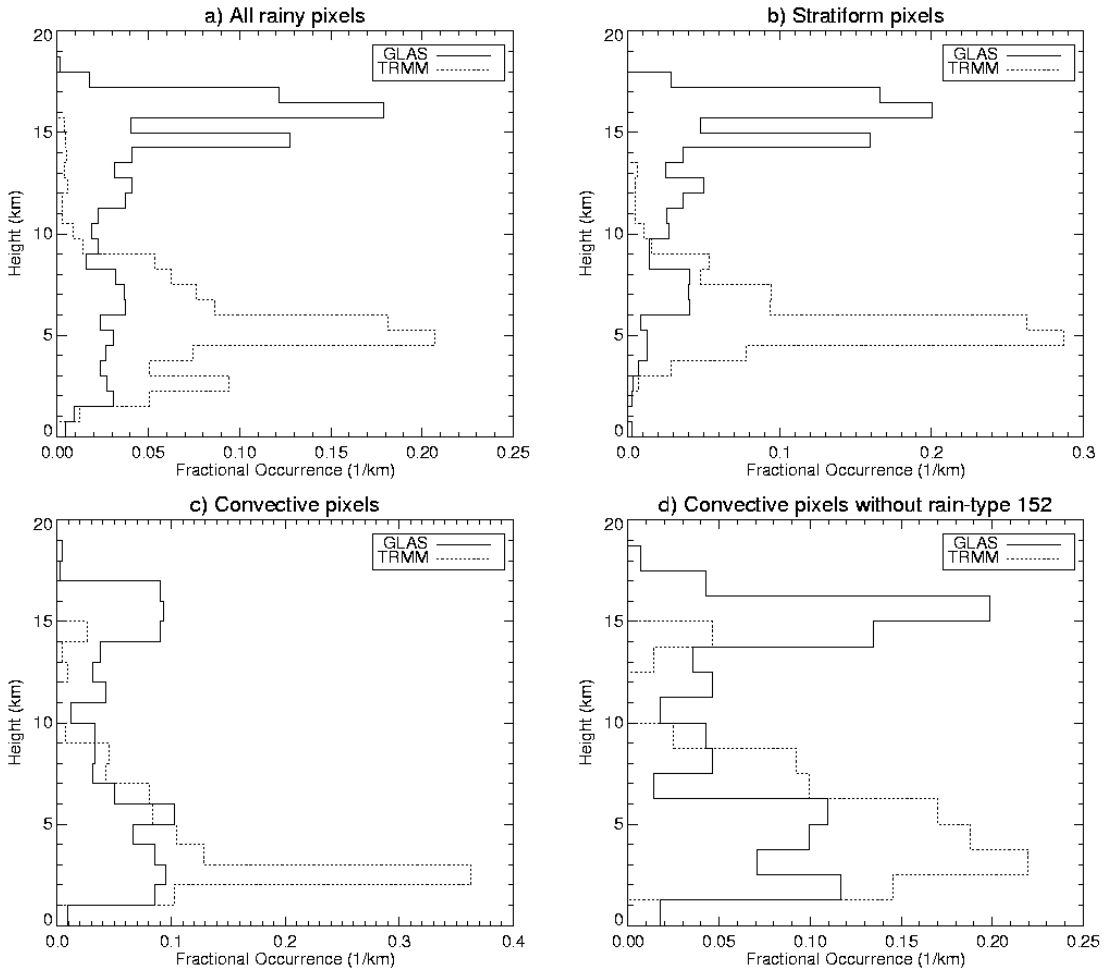

Figure 5: Histograms of coincident GLAS cloud-top (solid) and TRMM echo-top (dotted) heights for a) all pixels containing near surface precipitation, b) stratiform pixels, c) convective pixels, and d) convective pixels with rain-type 152 removed.

Therefore, though some spread exists, it is acceptable to assume that most of the stratiform precipitation tops coincide with deep clouds, regardless of the measured precipitation height.

The convective cloud histogram (Figure 5c) shows more uniformity in GLAS cloud height. The relatively large amount of deep clouds and lack of high-altitude precipitation tops suggest that there exist areas where what are viewed as deep clouds

correspond to more shallow precipitation. A large portion of this was due to the inclusion of rain flag 152 (shallow non-isolated precipitation) in the convective category. While rain type 152 is associated with warm rain convective formation processes, it is often found on the edges of deeper convection and/or larger mesoscale precipitation events; cloud outflow from deeper precipitation would in this case overlay these shallow convective events. 61% of the convective peak between 2 and 3 km is due to shallow non-isolated rain. As such, the higher cloud tops associated with these pixels (> 10 km) are likely due to the anvil of neighboring cells overlaying these shallow cells.

Figure 5d also shows convective precipitation, only with rain flag 152 removed. More agreement is noted between the cloud and precipitation histograms; the shallow precipitation peak is not as prominent as compared to Figure 5c. However, the major precipitation peak at shallow heights still does not correspond with the major cloud peak at deep heights. This issue was taken into account in calculation of fractional areal coverage, to be discussed in Chapter IV.

CHAPTER IV

TROPICAL PRECIPITATING CLOUD FRACTION

The tropical region, defined in this paper as 20°S-20°N, was divided into a grid with resolution of 2.5° × 2.5°. Data from every overpass by the satellites were relegated to the appropriate grid cell. The data for each grid cell were further separated into three height categories: shallow, mid-level, and deep.

For the GLAS data, cloud tops below 5 km were counted as shallow, tops between 5-10 km were counted as mid-level, and tops above 10 km were counted as deep. For pixels with multiple cloud layers, the lowest detected cloud-top height was used. As discussed by *Dessler et al.* [2006], the existence of multiple cloud layers and the fundamental limitation that the GLAS is unable to see through clouds with optical depths greater than 3-4 mean that mid- and low-level clouds will potentially be undercounted.

Consistent with this discussion, 40% of the convective coincident scans (Figure 5d) showed precipitation-top heights much lower than the associated cloud-top heights (i.e., shallow echo-top height and mid-level cloud-top height, etc.), suggesting that precipitating clouds may be located below a thick cloud that extinguishes the GLAS beam. To account for this potential undercount, the fraction of clouds at any given level was adjusted using the assumption that the fraction was uncorrelated with the fraction of clouds at higher levels [*Wang et al.*, 1995; *Bergman and Salby*, 1996; *Dessler et al.*, 2006]. Thus, the fraction of mid-level clouds (M_a) was calculated to be the fraction of

clouds seen at midlevels (M_0) plus the fraction of clouds seen as extinguishing in the deep category (D_0) times M_0;

$$M_a = M_0 + M_0 D_0 .$$

Similarly, the fraction of shallow clouds (S_a) was calculated as follows:

$$S_a = S_0 + S_0 M_0 + S_0 D_0 ,$$

where S_0 is the fraction of clouds seen at shallow levels.

These corrected estimates for mid- and low-level clouds should be considered an upper limit for the actual shallow and mid-level cloud populations. This is because deep convective clouds (which make up some of the extinguishing cloud population) extend throughout most of the troposphere and therefore preclude the existence of mid and low level clouds, and that it is likely that shallow cloud populations decrease as deep convection increases. The total number of counts for each category was then divided by the total number of scans over the specific grid to yield the fractional areal coverage (FAC) of each cloud type (Figure 6).

Average cloud FAC values derived from the GLAS across the Tropics were as follows: 23.5% for shallow clouds, 11.5% for mid-level clouds, and 10.9% for deep clouds. As shown in Figure 6a, shallow clouds occur up to 100% of the time in the stratus regions off the western coasts of South America and Africa. Mid-level clouds (Figure 6b) appear to be most prominent (>30% occurrence) over the Andes of South America, possibly because of orographic lifting, as well as over central Africa, the Indian Ocean, New Guinea, and Brazil. The ITCZ is prominent in both the mid-level and deep cloud (Figure 6c) coverage data. High percentages (>20%) of deep tropical

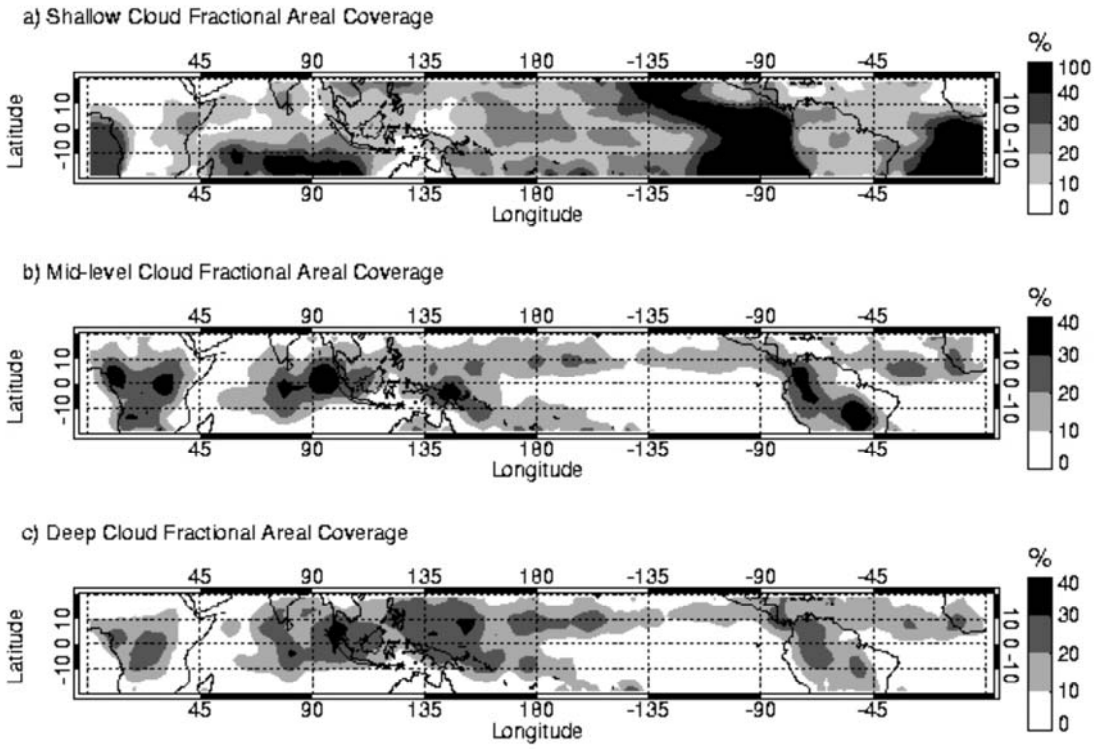

Figure 6: Tropical cloud fractional areal coverage based on cloud-top height, separated into a) shallow (0-5 km), b) mid-level (5-10 km), and c) deep (10 km+).

cloud areal coverage are also noticeable over central Africa, the western Pacific Ocean, and South America. These results are similar to those obtained by *Dessler et al.* [2006], which uses a different methodology than this study; *Dessler et al.* included all clouds and analyzed fractional coverage in terms of cloud-top potential temperature instead of height. While shallow clouds tend to be dominant over the oceans, mid-level and deep clouds tend to be associated with the continents, with the exception of the large deep-cloud populations over the ITCZ and warm pool of the western Pacific.

For the PR data, a 1-km offset was assumed between the cloud top and echo top heights, allowing for cloud development above the levels at which precipitation is visible

to the PR. Thus, convective pixels with echo tops below 4 km were counted as shallow, between 4-9 km as mid-level, and above 9 km as deep. All stratiform data points for the TRMM PR data were included as deep precipitation, as explained in Section 2. In addition, shallow non-isolated rain type 152 is also included as corresponding to deep clouds, as explained in Section 3. Fractional areal coverage of each precipitation type was computed using the same method as for the GLAS data.

Figure 7 shows the geographical variation in precipitation FAC for each height. Mid-level and deep echo occurrence show continental maxima, while regions of precipitation maxima in all three height categories appear to be the Indian Ocean, the ITCZ and the South Pacific Convergence Zone. The oceanic regional patterns visible in Figure 7 are similar to those in Figure 7c of *Petty* [1995], though the fractional areal coverage differs in magnitude due to differences in methodology. In comparison with cloud areal coverage, mean values for precipitation FAC were much smaller: 0.5% for shallow, 0.6% for mid-level, and 3.2% for deep precipitation. Shallow cloud FAC approaches 100% in some areas, yet Figure 7a shows that shallow precipitation FAC reaches a maximum of 1.4%. The corresponding maxima for cloud and precipitation FAC for mid-level clouds are 40% and 2%, respectively, and for deep clouds 40% and 12%, respectively.

In addition, cloud coverage does not necessarily correlate to precipitation coverage. For example, the stratus regions off of South America and Africa have high cloud coverage but near zero precipitation coverage. Meanwhile, the northern Indian Ocean sees less than 20% shallow cloud FAC, yet has relatively high levels of shallow

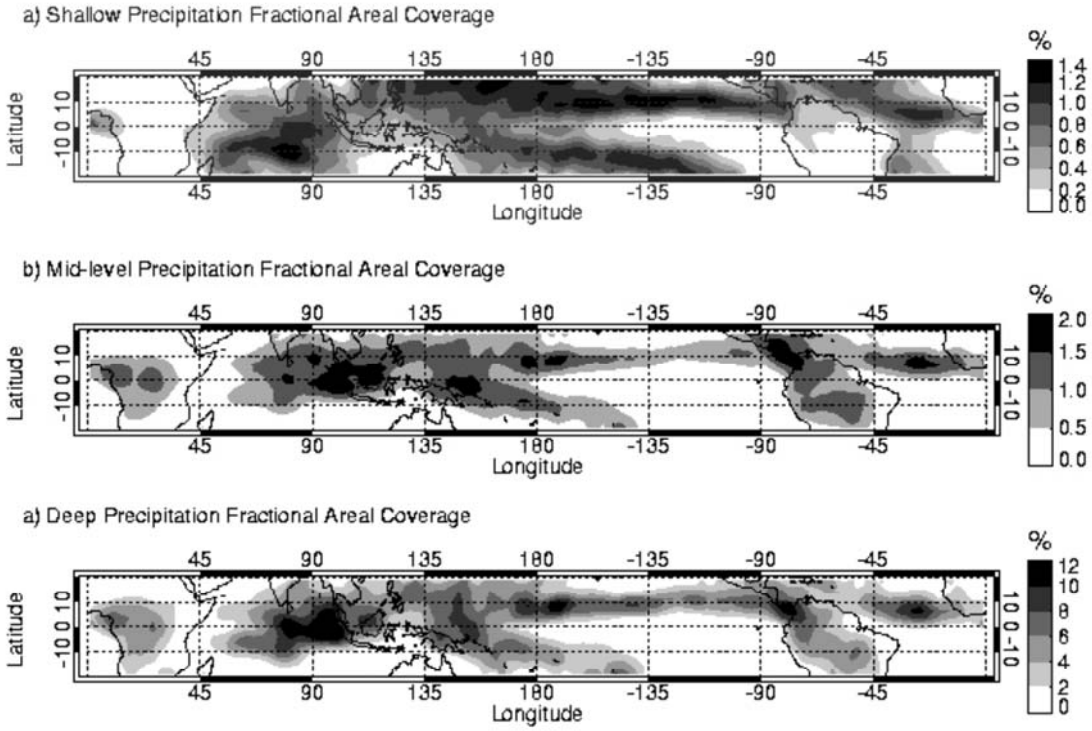

Figure 7: Tropical precipitation fractional areal coverage defined by echo-top height and precipitation type, separated into a) shallow (convective pixels, 0-4 km), b) mid-level (convective pixels, 4-9 km) and c) deep (convective pixels, 9 km+ and all stratiform pixels).

precipitation FAC, suggesting that the relatively low occurrence of shallow clouds in this region is associated with more efficient convective processes, further described in the discussion for Figure 8.

Figure 8 shows the computed tropical precipitating cloud fraction (PCF), obtained by dividing the precipitation FAC (Figure 7) at each level by the cloud FAC at the same pixel and level (Figure 6). Preliminary computations of this step yielded non-physical answers (i.e., PCF values of greater than 100%) for certain grid points. These

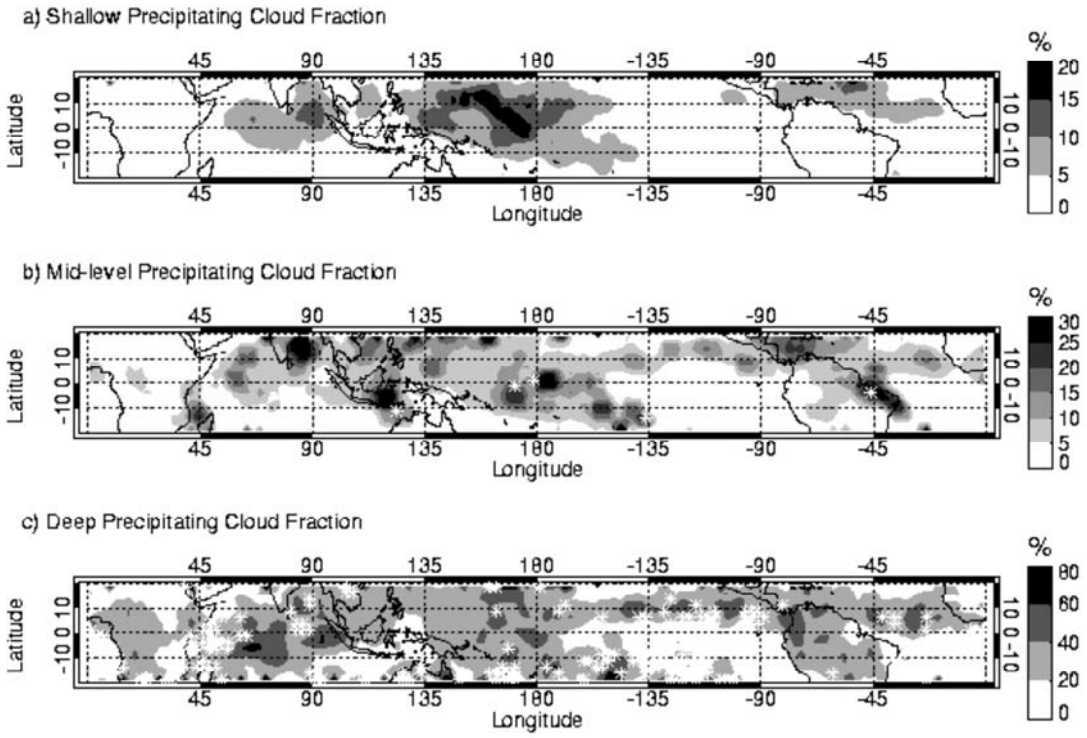

Figure 8: Tropical precipitating cloud fraction, or the fractional areal coverage for precipitation divided by the fractional areal coverage for clouds, separated into a) Shallow, b) Mid-level, and c) Deep categories. White stars represent grids where PCF greater than 100% was calculated; these values were not included in the contouring of the figures.

points are shown in Figure 8 as white asterisks. Considering the tropics as a whole, the mean PCFs for each category across the 20°S-20°N region were 3.7% for shallow clouds, 6.5% for mid-level clouds, and 24.1% for deep clouds. These values seem to compare well with the low precipitation efficiencies, defined as ratio of the amount of condensed water that reaches the ground to the mass of vapor entering the cloud, found by *Braham* [1952] and *Houghton* [1968]. The data also suggest that deep clouds are more likely to rain (i.e., have a higher PCF) than shallow and mid-level clouds.

Figure 8a shows that shallow clouds tend to be more efficient at producing rain over the Indian Ocean, West Pacific, and West Atlantic. Warm sea surface temperatures (SST) are common over these areas, leading to enhanced boundary-layer heating. The mid-level PCF (Figure 8b) shows higher efficiencies over the Bay of Bengal, West Pacific, and eastern South America. The deep PCF (Figure 8c) identifies the equatorial Indian Ocean, ITCZ, South Pacific Convergence Zone and northern Andes as regions where deep clouds are more efficient at precipitating.

Figure 8c also contains 153 grid cells with non-physical answers. The reason behind this is uncertain, though one possibility is that some of the stratiform precipitation counted in this category may actually be associated with mid-level clouds. In addition, the short time-span of data and the lack of coincident measurements between the two satellites may also play a factor. Because of the erratic nature of Figures 8b and 8c, the values given should be considered only in terms of large-scale regional magnitude differences.

In order to determine the sensitivity of the results to the choice of boundaries between shallow, mid-level, and deep clouds, we have repeated the PCF calculations after varying the boundaries. The GLAS shallow/mid-level boundary height was varied from 3 km to 5 km and the mid-level/deep boundary height was varied from 7.75 km to 12.75 km. For the TRMM convective echo-top distribution, the shallow/mid-level boundary height wave varied from 3 km to 4.5 km and the mid-level/deep boundary height was varied from 6.25 km to 9 km. Mean PCF values were then calculated for each possible boundary condition (removing those combinations where the TRMM

precipitation boundary height would be higher than the corresponding GLAS cloud boundary height).

The results of the sensitivity test are listed in Table 2. Note that the option of varying both the upper and lower boundaries of the mid-level category led to many more possible combinations than for the shallow and deep categories. While there are some variations in calculated PCFs, the mean values, as well as the spread of these values, still suggest that deep clouds are more likely to be raining than shallow or mid-level clouds regardless of boundary height, as was expected. In addition, the average PCF for each category remains relatively low, below 30% in all cases, regardless of bounds.

Table 2: Spread of Precipitating Cloud Fraction mean values, as dependent on the levels chosen for the boundaries between the three height categories.

Category	**Combinations**	**Mean**	**SD**	**Minimum**	**Maximum**
Shallow	42	3.63%	0.557%	2.51%	4.65%
Mid-level	9954	6.05%	1.56%	2.34%	11.9%
Deep	237	25.9%	2.09%	20.9%	29.5%

CHAPTER V

CONCLUSION

This analysis seeks to determine the likelihood of rain from shallow, mid-level, and deep clouds in the tropics. Cloud data were obtained from the GLAS/ICESat cloud-height product for the Laser 2A period between 26 September and 18 November 2003. Precipitation data came from the corresponding period from the TRMM PR.

Areal coverage calculations were made for both clouds and precipitation and separated into shallow, mid-level, and deep categories. Fractional areal coverage (FAC) in all three cloud height categories show significant cloud and precipitation coverage over the ITCZ and the warm pool of the western Pacific. In addition, large cloud and precipitation FACs are noted over the tropical continents in the mid-level and deep categories. Also apparent upon comparison is that areas of high cloud FAC do not always coincide with areas of high precipitation FAC, and vice versa.

Precipitating cloud fraction (PCF) was then calculated by dividing the precipitation FAC by the cloud FAC. On average, these values are low, averaging around 24% for deep clouds, 7% for mid-level clouds and 4% for shallow clouds, with regional maxima mostly located over the oceans.

A major issue in this analysis is the lack of concurrent scans between the two satellites in order to connect specific cloud and precipitation features more accurately. It is hoped that the newly-launched CloudSat and CALIPSO satellites [*Stephens et al.*, 2002] will provide greater opportunities to continue this line of study.

REFERENCES

Awaka, J., T. Iguchi, H Kumagai, and K. Okamoto (1997), Rain type classification algorithm for TRMM precipitation radar, *Proc. IEEE 1997 Int. Geoscience and Remote Sensing Symp.*, 1633-1635.

Bergman, J. W., and M. L. Salby (1996), Diurnal variations of cloud cover and their relationship to climatological conditions, *Journal of Climate*, *9*, 2802-2820.

Braham, R. R. (1952), The Water and Energy Budgets of the Thunderstorm and Their Relation to Thunderstorm Development, *Journal of Meteorology*, *9*, 227-242.

Cetrone, J., and R. A. Houze (2006), Characteristics of tropical convection over the ocean near Kwajalein, *Mon Weather Rev*, *134*, 834-853.

Dessler, A. E., S. P. Palm, and J. D. Spinhirne (2006), Tropical cloud-top height distributions revealed by the Ice, Cloud, and Land Elevation Satellite (ICESat)/Geoscience Laser Altimeter System (GLAS), *Journal of Geophysical Research-Atmospheres*, *111*, D12, art. no. d12215.

Hardy, K. R. (1963), The Development of Raindrop-Size Distributions and Implications Related to the Physics of Precipitation, *Journal of the Atmospheric Sciences*, *20*, 299-312.

Hildebrand, P. H. (1998), Shear-parallel moist convection over the tropical ocean: A case study from 18 February 1993 TOGA COARE, *Mon Weather Rev*, *126*, 1952-1976.

Houghton, H. G. (1968), On Precipitation Mechanisms and their Artificial Modification, *Journal of Applied Meteorology*, *7*, 851-859.

Houze, R. A. (1981), Structures of Atmospheric Precipitation Systems - a Global Survey, *Radio Science*, *16*, 671-689.

Houze, R. A. (1997), Stratiform precipitation in regions of convection: A meteorological paradox?, *Bulletin of the American Meteorological Society*, *78*, 2179-2196.

Houze, R. A., and C. P. Cheng (1977), Radar Characteristics of Tropical Convection Observed during Gate - Mean Properties and Trends over Summer Season, *Mon Weather Rev*, *105*, 964-980.

Jensen, M. P., and A. D. Del Genio (2006), Factors limiting convective cloud-top height at the ARM Nauru Island climate research facility, *Journal of Climate*, *19*, 2105-2117.

Johnson, R. H., P. E. Ciesielski, and K. A. Hart (1996), Tropical inversions near the 0 degrees C level, *Journal of the Atmospheric Sciences*, *53*, 1838-1855.

Johnson, R. H., T. M. Richenbach, S. A. Rutledge, P. E. Ciesielski, and W. H. Schubert (1999), Trimodal characteristics of tropical convection, *Journal of Climate*, *12*, 2397-2418.

Kummerow, C., W. Barnes, T. Kozu, J. Shiue, and J. Simpson (1998), The Tropical Rainfall Measuring Mission (TRMM) sensor package, *Journal of Atmospheric and Oceanic Technology*, *15*, 809-817.

LeMone, M. A., and R. J. Meitin (1984), 3 Examples of Fair-Weather Mesoscale Boundary-Layer Convection in the Tropics, *Mon Weather Rev*, *112*, 1985-1997.

Lucas, C., E. J. Zipser, and M. A. Lemone (1994), Vertical Velocity in Oceanic Convection Off Tropical Australia, *Journal of the Atmospheric Sciences*, *51*, 3183-3193.

Madden, R. A., and P. R. Julian (1994), Observations of the 40-50-Day Tropical Oscillation - a Review, *Mon Weather Rev*, *122*, 814-837.

Mahesh, A., M. A. Gray, S. P. Palm, W. D. Hart, and J. D. Spinhirne (2004), Passive and active detection of clouds: Comparisons between MODIS and GLAS observations, *Geophys Res Lett*, *31*, 4, art. no. L04108.

Malkus, J. S., and H. Riehl (1964), Cloud Structure and Distributions over the Tropical Pacific Ocean, *Tellus*, *16*, 275-287.

Marshall, J. S., and W. M. Palmer (1948), The Distribution of Raindrops with Size, *Journal of Meteorology*, *5*, 165-166.

Parsons, D. B., K. Yoneyama, and J. L. Redelsperger (2000), The evolution of the tropical western Pacific atmosphere-ocean system following the arrival of a dry intrusion, *Quarterly Journal of the Royal Meteorological Society*, *126*, 517-548.

Petty, G. W. (1995), Frequencies and Characteristics of Global Oceanic Precipitation from Shipboard Present-Weather Reports, *Bulletin of the American Meteorological Society*, *76*, 1593-1616.

Redelsperger, J. L., D. B. Parsons, and F. Guichard (2002), Recovery processes and factors limiting cloud-top height following the arrival of a dry intrusion observed during TOGA COARE, *Journal of the Atmospheric Sciences*, *59*, 2438-2457.

Riehl, H., and J. Simpson (1979), The heat balance of the equatorial trough zone, revisited, *Contrib. Atmos. Phys.*, *52*, 287-304.

Schumacher, C., and R. A. Houze (2003a), Stratiform rain in the tropics as seen by the TRMM precipitation radar, *Journal of Climate*, *16*, 1739-1756.

Schumacher, C., and R. A. Houze (2003b), The TRMM precipitation radar's view of shallow, isolated rain, *Journal of Applied Meteorology*, *42*, 1519-1524.

Short, D. A., and K. Nakamura (2000), TRMM radar observations of shallow precipitation over the tropical oceans, *Journal of Climate*, *13*, 4107-4124.

Shusse, Y., and K. Tsuboki (2006), Dimension characteristics and precipitation efficiency of cumulonimbus clouds in the region far south from the mei-yu front over the eastern Asian continent, *Mon Weather Rev*, *134*, 1942-1953.

Simpson, J. (1992), Global circulation and tropical cloud activity, *The Global Role of Tropical Rainfall*, J. S. Theon et al., Eds., A. Deepak Publishing, Hampton, 77-92.

Spinhirne, J. D., S. P. Palm, W. D. Hart, D. L. Hlavka, and E. J. Welton (2005), Cloud and aerosol measurements from GLAS: Overview and initial results, *Geophys Res Lett*, *32*, 22, art. no. L22S03.

Steiner, M., R. A. Houze, and S. E. Yuter (1995), Climatological Characterization of 3-Dimensional Storm Structure from Operational Radar and Rain-Gauge Data, *Journal of Applied Meteorology*, *34*, 1978-2007.

Stephens, G. L., D. G. Vane, R. J. Boain, G. G. Mace, K. Sassen, and co-authors (2002), The cloudsat mission and the a-train - A new dimension of space-based observations of clouds and precipitation, *Bulletin of the American Meteorological Society*, *83*, 1771-1790.

Takahashi, N., and T. Iguchi (2004), Estimation and correction of beam mismatch of the Precipitation Radar after an orbit boost of the Tropical Rainfall Measuring Mission satellite, *IEEE Transactions on Geoscience and Remote Sensing*, *42*, 2362-2369.

Takemi, T., O. Hirayama, and C. H. Liu (2004), Factors responsible for the vertical development of tropical oceanic cumulus convection, *Geophys Res Lett*, *31*, 11, art. no. L11109.

Wang, L. K., and A. E. Dessler (2006), Instantaneous cloud overlap statistics in the tropical area revealed by ICESat/GLAS data, *Geophys Res Lett*, *33*, 15, art. no. L15804.

Wang, P. H., M. P. McCormick, P. Minnis, G. S. Kent, G. K. Yue, and K. M. Skeens (1995), A Method for Estimating Vertical-Distribution of the Sage-Ii Opaque Cloud Frequency, *Geophys Res Lett*, *22*, 243-246.

Waugh, D. W., and L. M. Polvani (2000), Climatology of intrusions into the tropical upper troposphere, *Geophys Res Lett*, *27*, 3857-3860.

Yanai, M., S. Esbensen, and J. H. Chu (1973), Determination of Bulk Properties of Tropical Cloud Clusters from Large-Scale Heat and Moisture Budgets, *Journal of the Atmospheric Sciences*, *30*, 611-627.

Yoneyama, K., and D. B. Parsons (1999), A proposed mechanism for the intrusion of dry air into the Tropical Western Pacific region, *Journal of the Atmospheric Sciences*, *56*, 1524-1546.

Zuidema, P. (1998), The 600-800-mb minimum in tropical cloudiness observed during TOGA COARE, *Journal of the Atmospheric Sciences*, *55*, 2220-2228.

Zwally, H. J., R. Schutz, S. Palm, W. Hart, S. Hlavka, J. Spinhirne, and E. Welton (2003), GLAS/ICESat L2 Global Cloud Heights for Multilayer Clouds V026, 26 September to 18 November 2003. Boulder, CO: National Snow and Ice Data Center. Digital Media.

APPENDIX

This appendix shows the 53 cross-sections used for the coincident scan analysis. The top figure beginning on the following page shows the horizontal scan, similar to Figure 4a. As with this figure, the thick dotted line is the path of the GLAS satellite (processing south to north), and the wide horizontal path is the TRMM satellite (processing west to east). Contoured is the storm height, or the height of the precipitation as viewed by the TRMM satellite.

The bottom figure shows the vertical cross-section along the GLAS path. Black areas represent clouds, and grey areas mark where the GLAS satellite returned no signal after extinguishing. The TRMM storm-height is contoured above this in color. The colors differ based on raintype (see Table 1 for definitions of each raintype), using the following color scale:

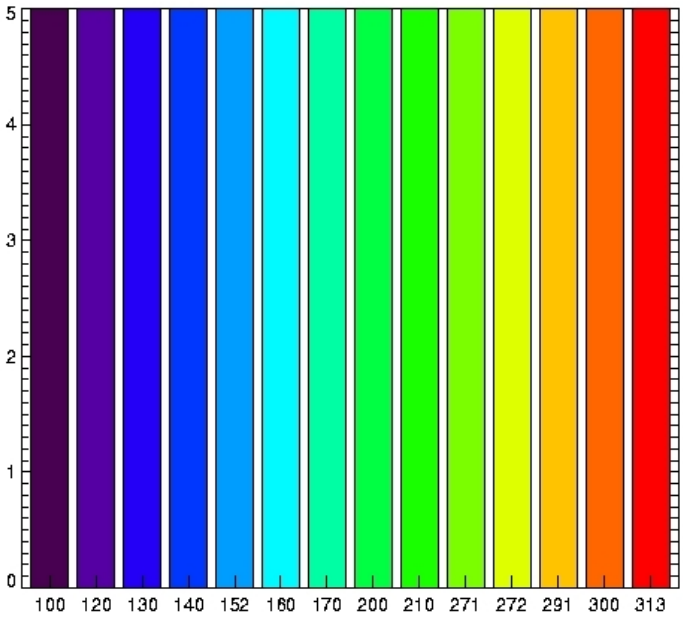

Coincident Scan 1:
GLAS orbital file GLA09_026_1102_029_0001_0_01_0001.DAT
TRMM orbital file 2A23.030928.33452.6.HDF

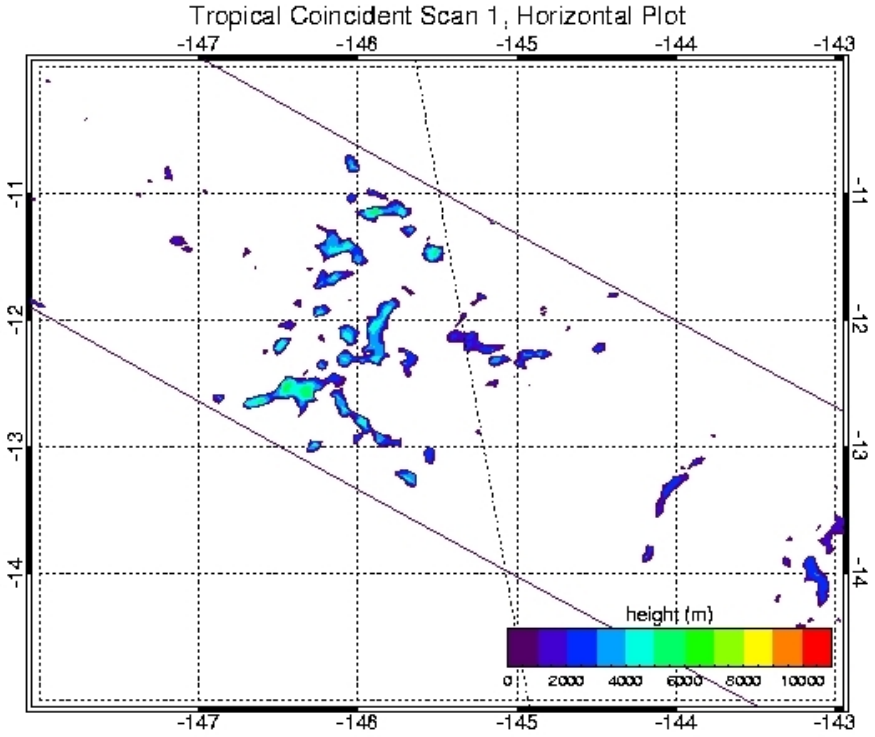

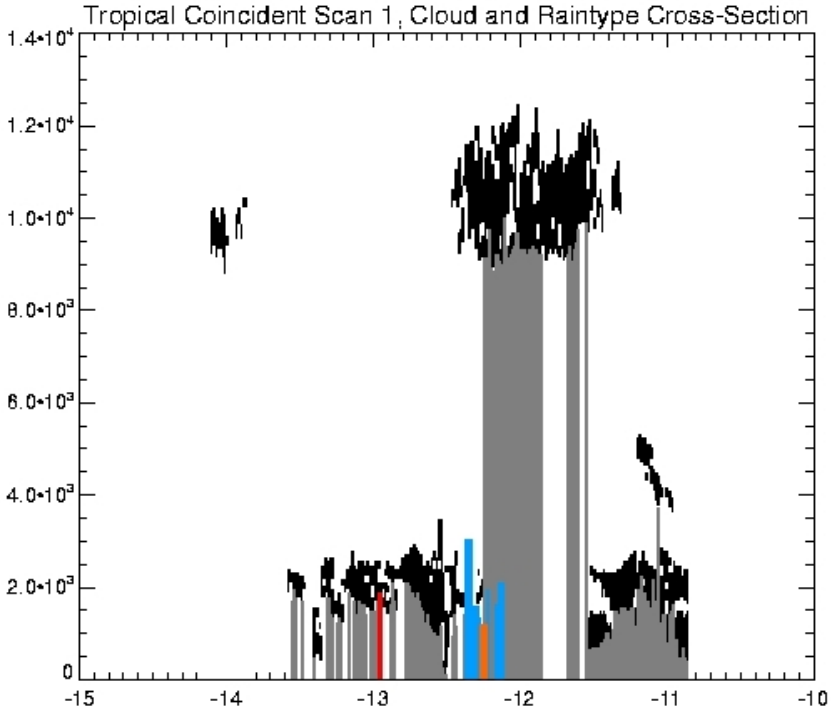

Coincident Scan 2:
GLAS orbital file GLA09_026_1102_029_0001_0_01_0001.DAT
TRMM orbital file 2A23.030928.33453.6.HDF

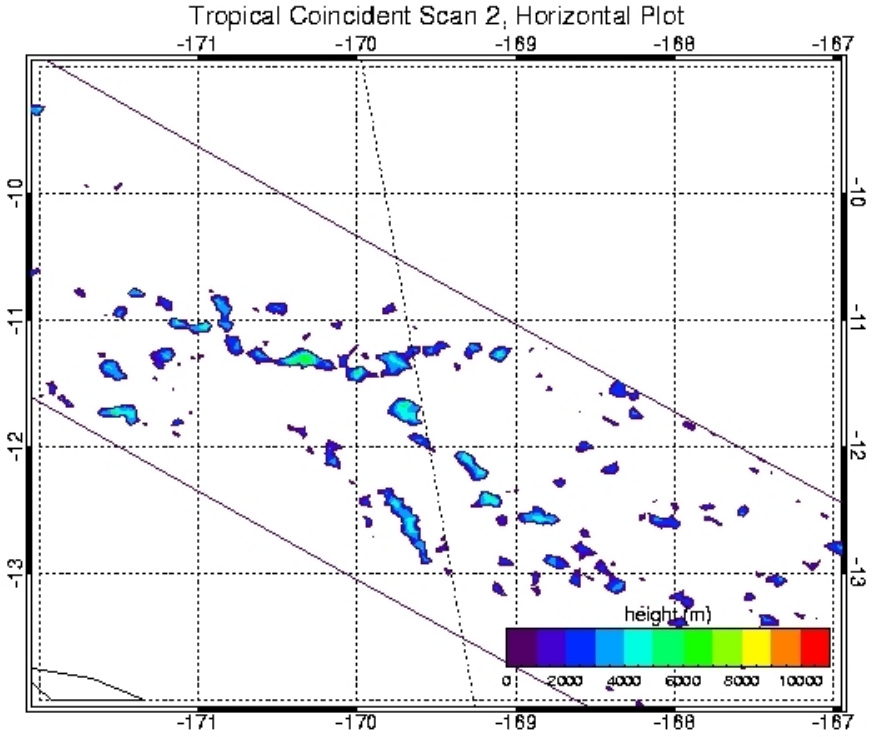

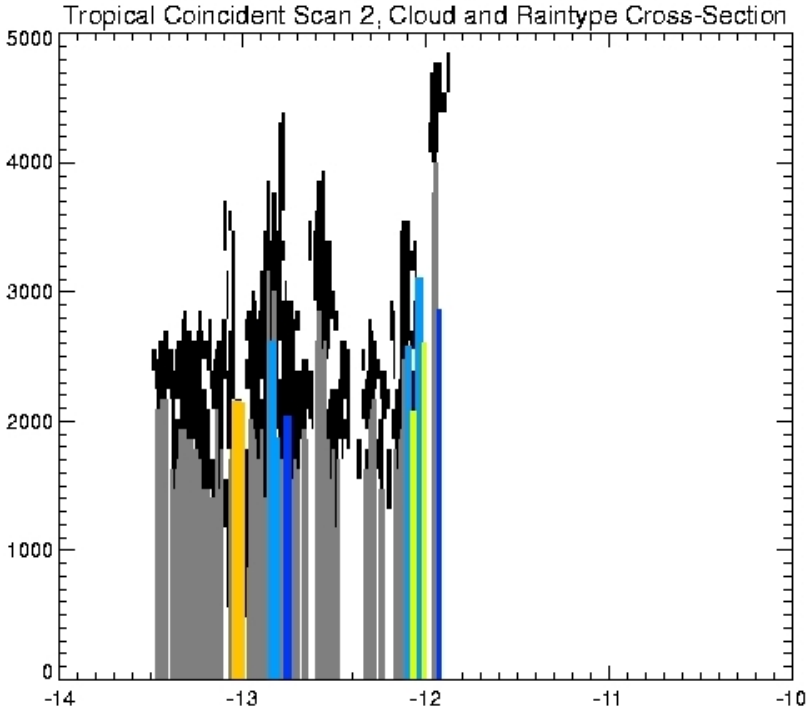

Coincident Scan 3:
GLAS orbital file GLA09_026_0001_0_01_0001.DAT
TRMM orbital file 2A23.030928.33454.6.HDF

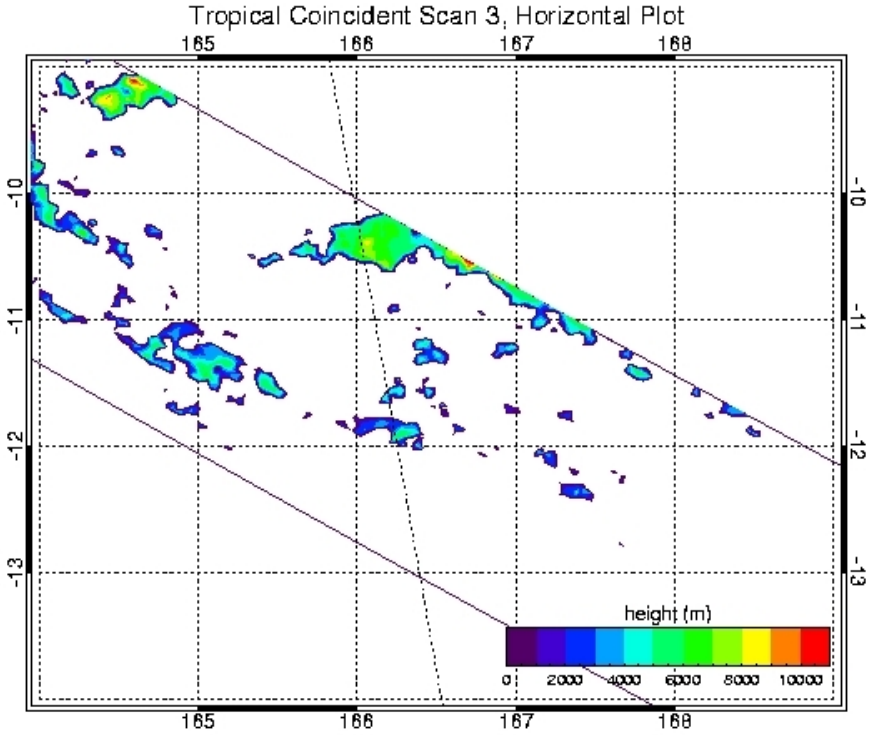

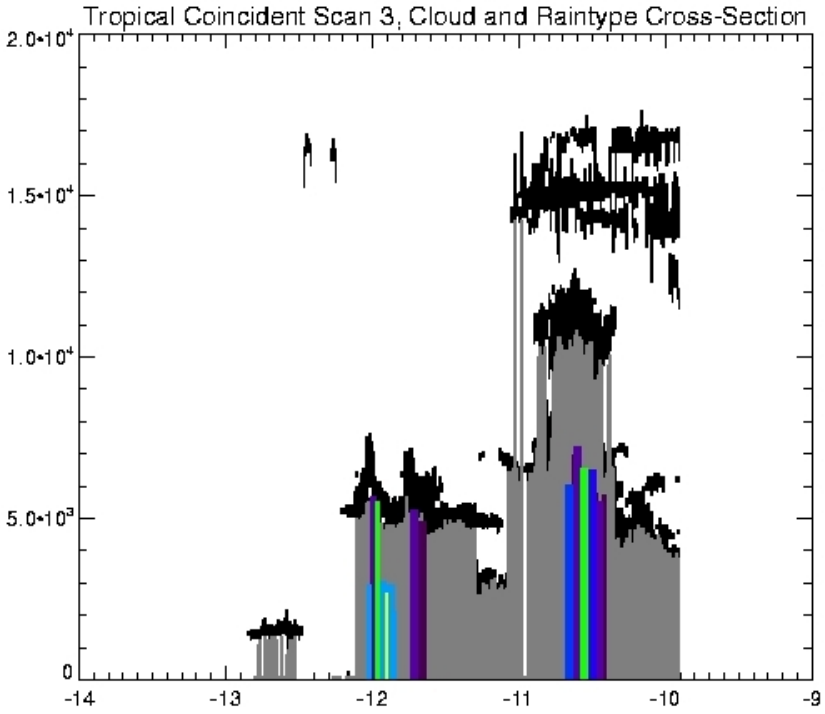

Coincident Scan 4:
GLAS orbital file GLA09_026_1102_029_0029_0_01_0001.DAT
TRMM orbital file 2A23.030929.33478.6.HDF

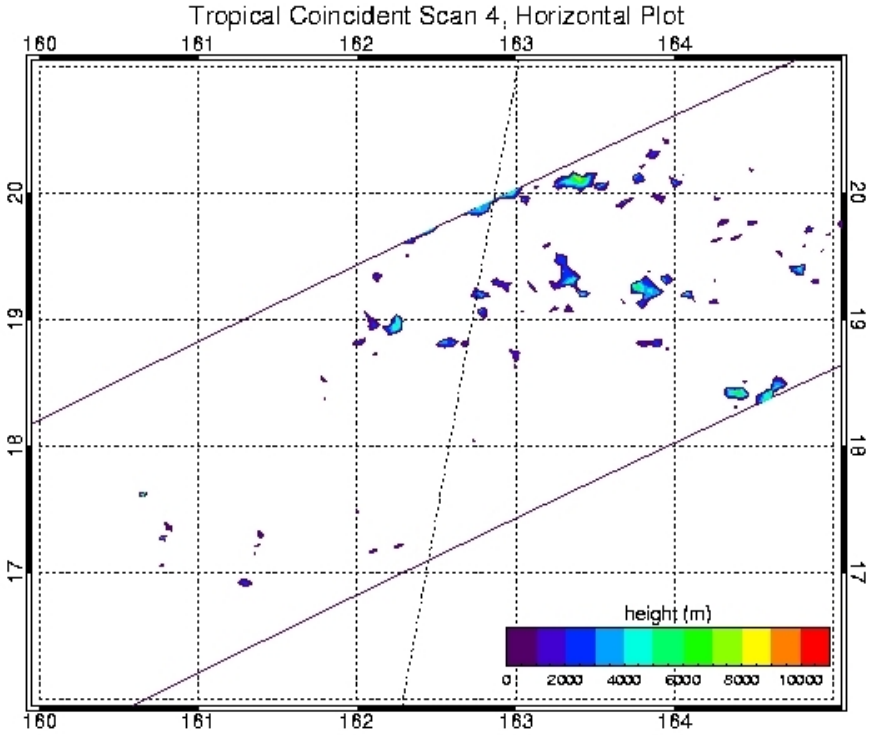

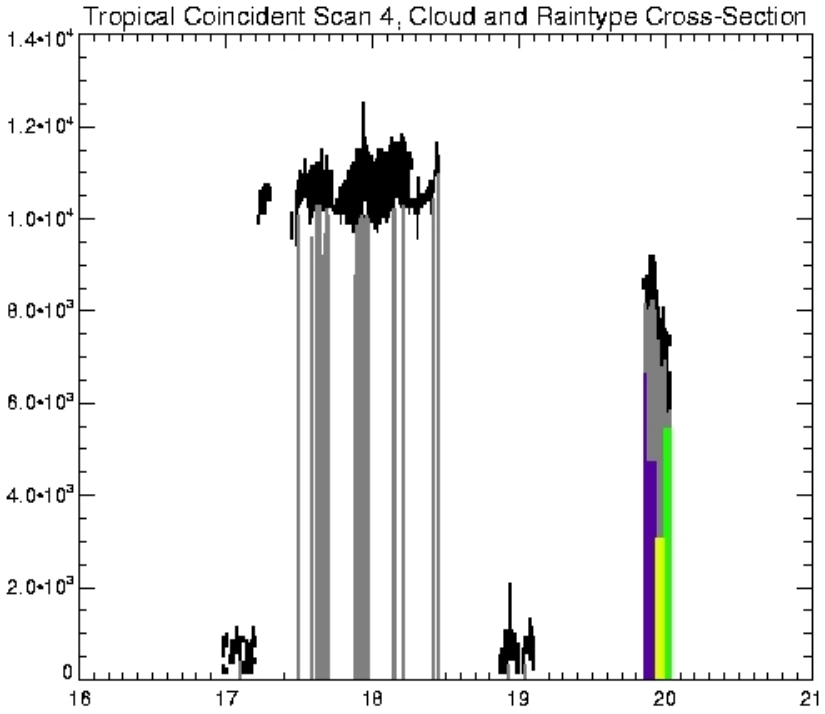

Coincident Scan 5:
GLAS orbital file GLA09_026_2103_001_1303_0_01_0001.DAT
TRMM orbital file 2A23.031018.33775.6.HDF

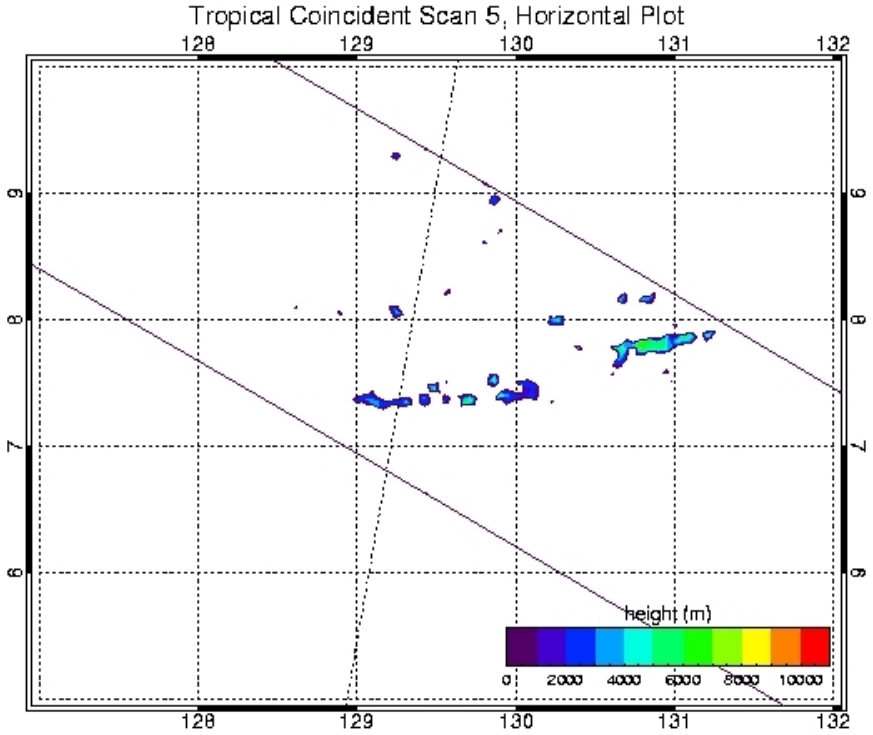

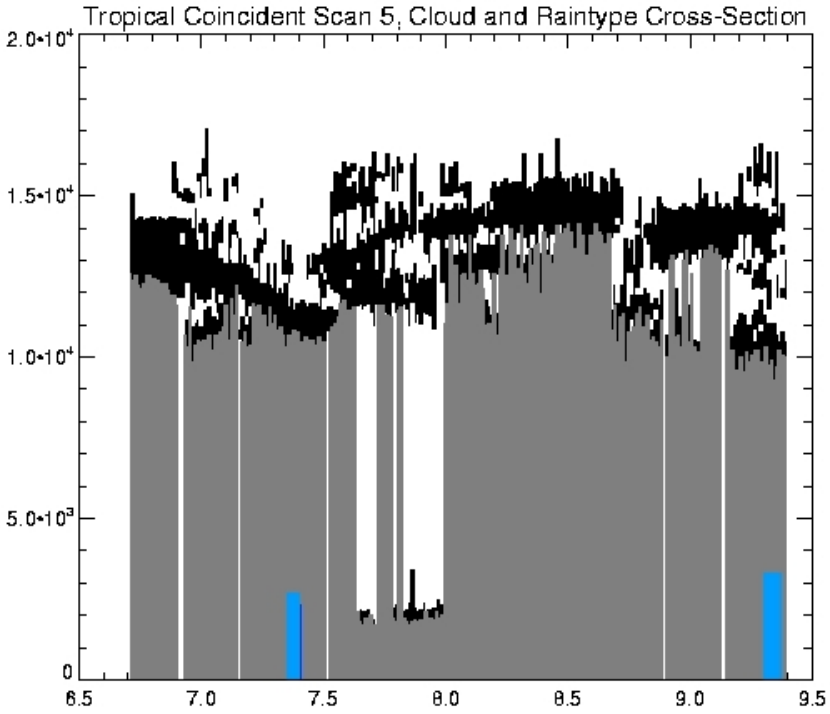

Coincident Scan 6:
GLAS orbital file GLA09_026_2103_001_1303_0_01_0001.DAT
TRMM orbital file 2A23.031019.33776.6.HDF

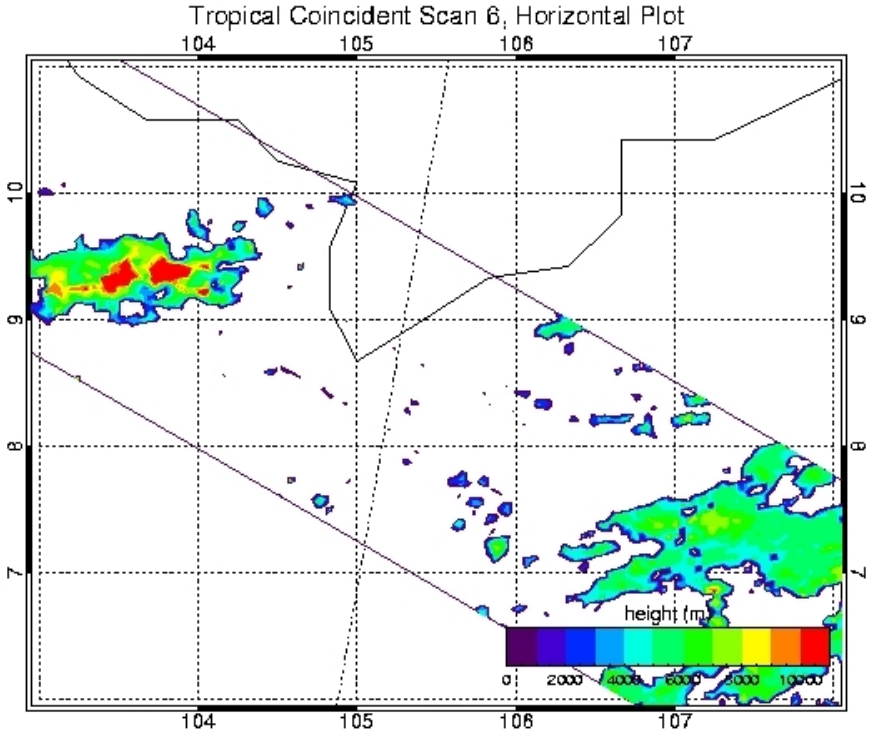

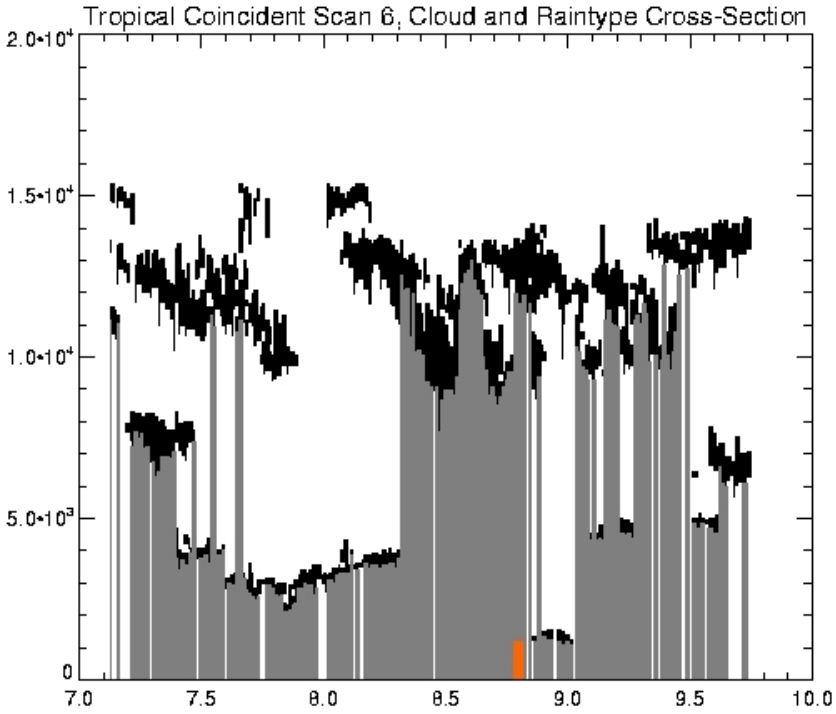

Coincident Scan 7:
GLAS orbital file GLA09_026_2103_001_1303_0_01_0001.DAT
TRMM orbital file 2A23.031019.33779.6.HDF

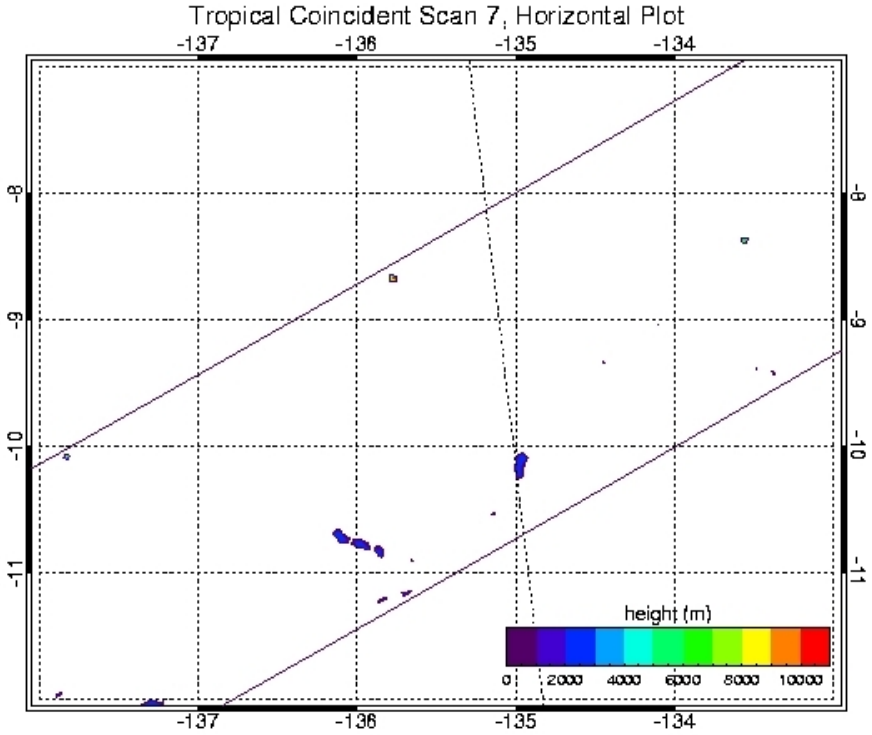

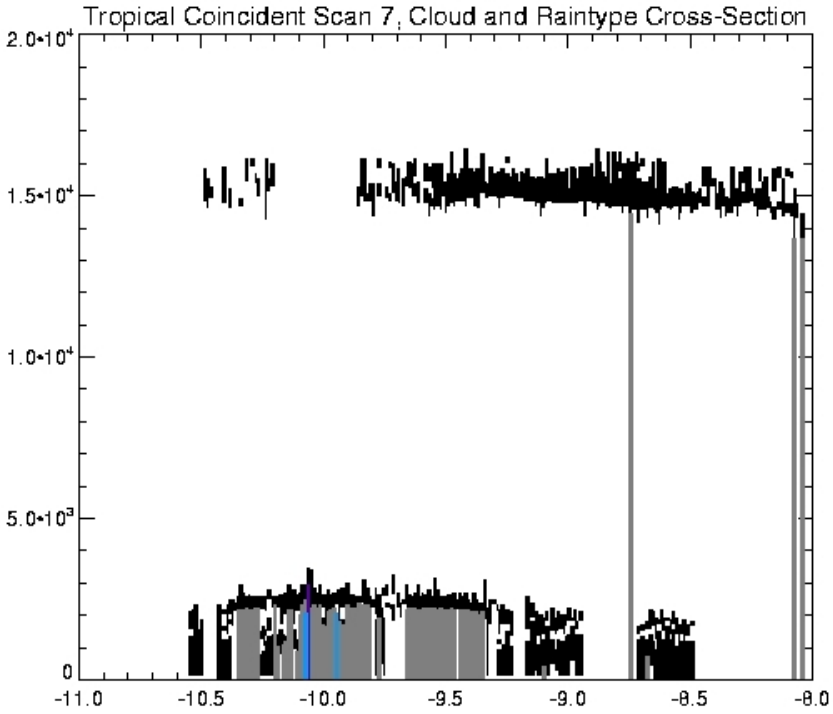

Coincident Scan 8:
GLAS orbital file GLA09_026_2103_001_1317_0_01_0001.DAT
TRMM orbital file 2A23.031019.33781.6.HDF

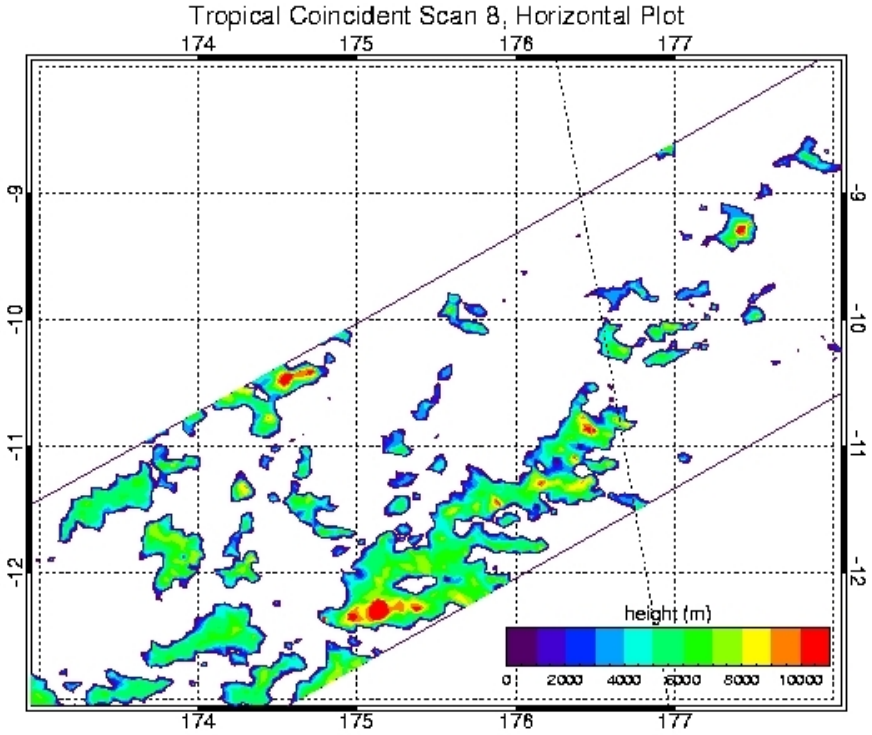

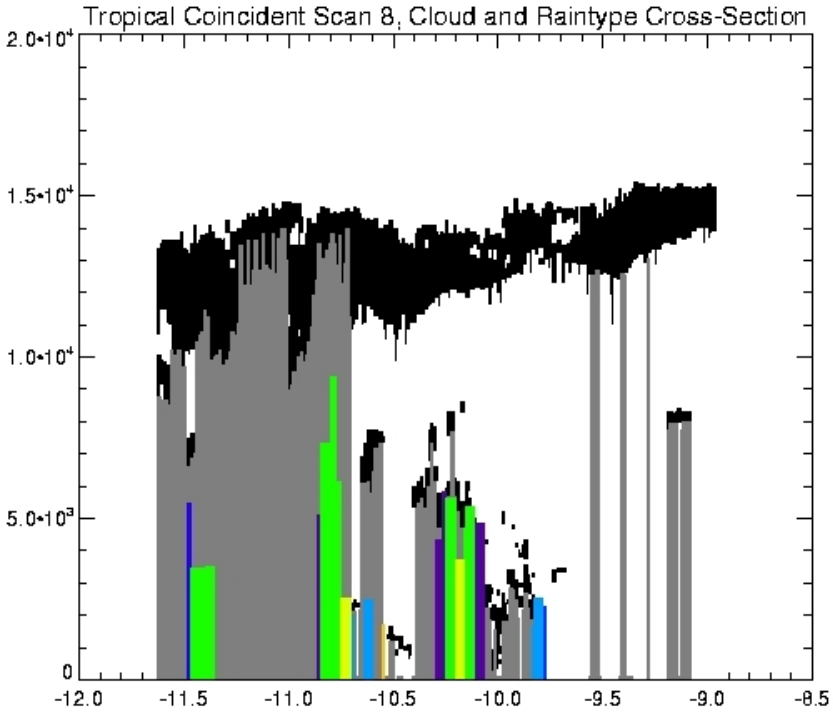

Coincident Scan 9:
GLAS orbital file GLA09_026_2103_001_1331_0_01_0001.DAT
TRMM orbital file 2A23.031020.33800.6.HDF

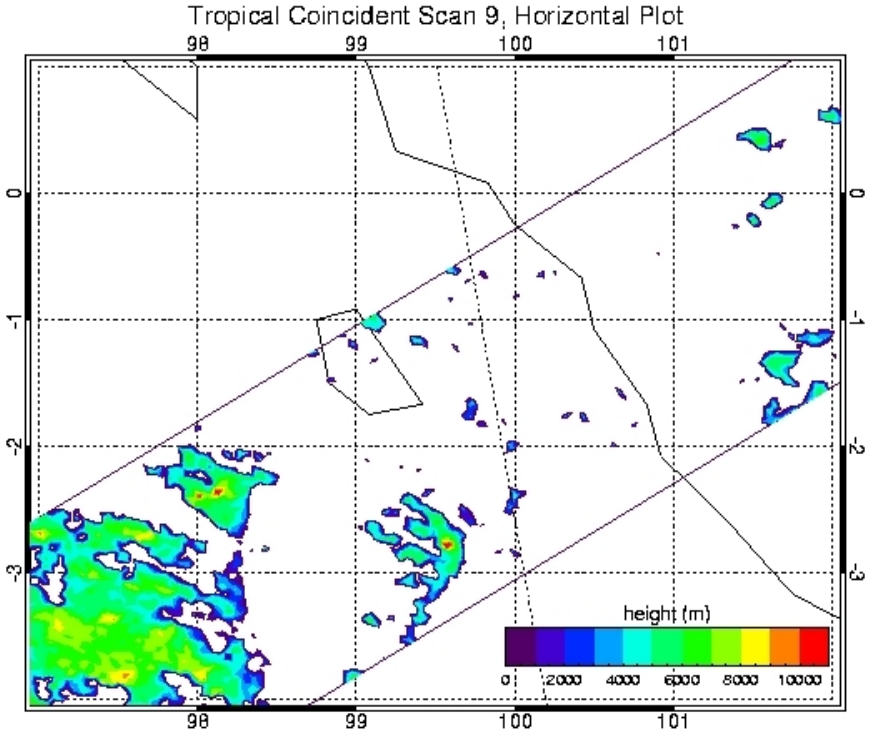

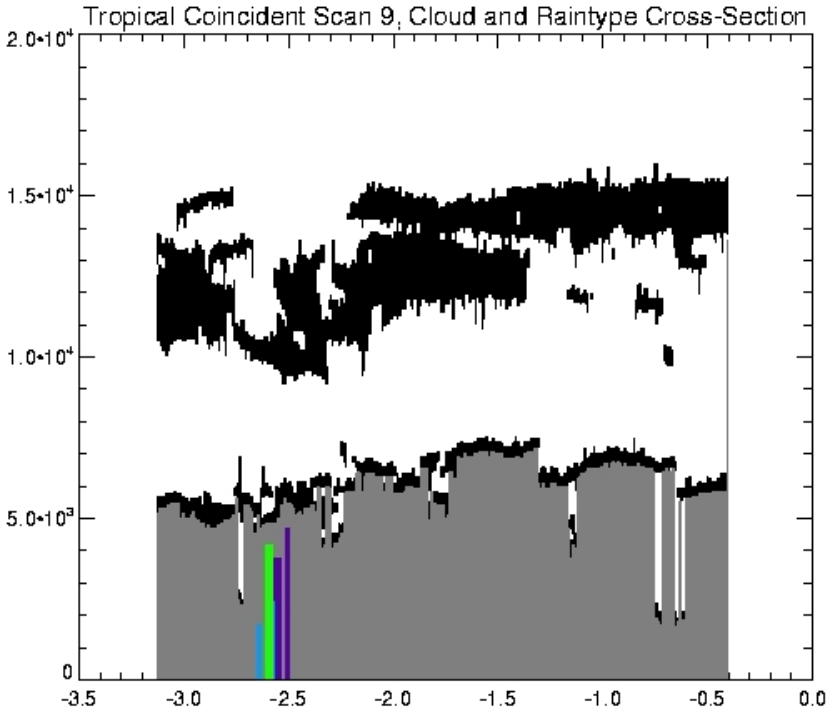

Coincident Scan 10:
GLAS orbital file GLA09_026_2103_001_1331_0_01_0001.DAT
TRMM orbital file 2A23.031020.33801.6.HDF

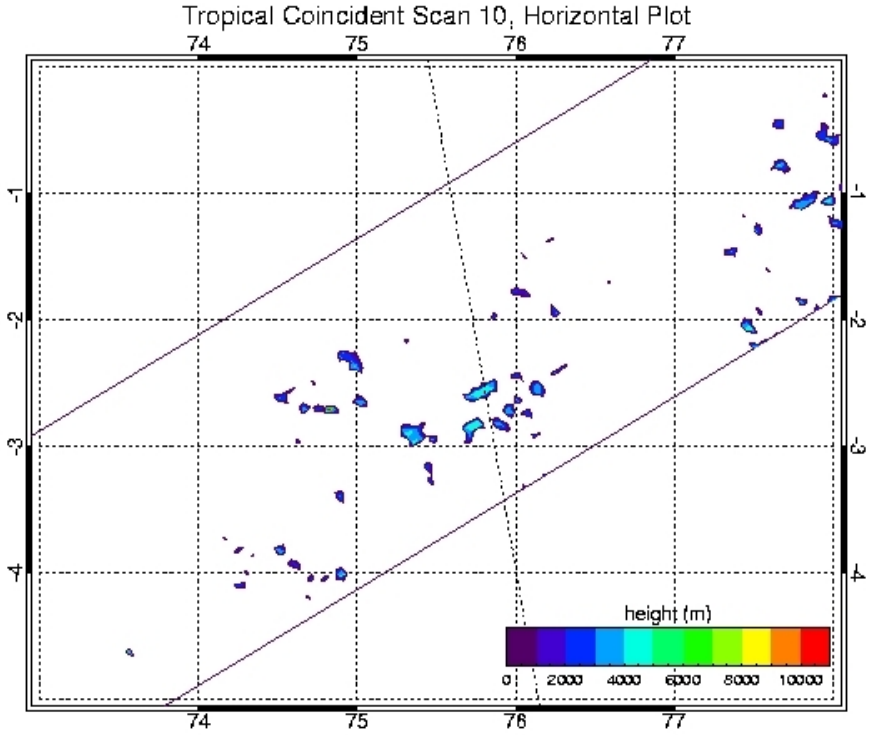

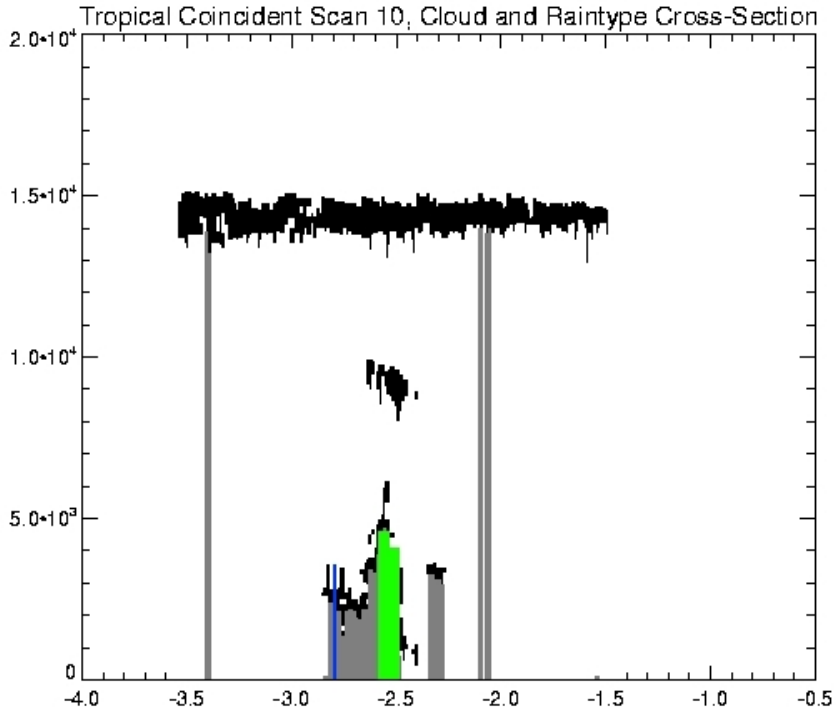

Coincident Scan 11:
GLAS orbital file GLA09_026_2103_001_1331_0_01_0001.DAT
TRMM orbital file 2A23.031020.33802.6.HDF

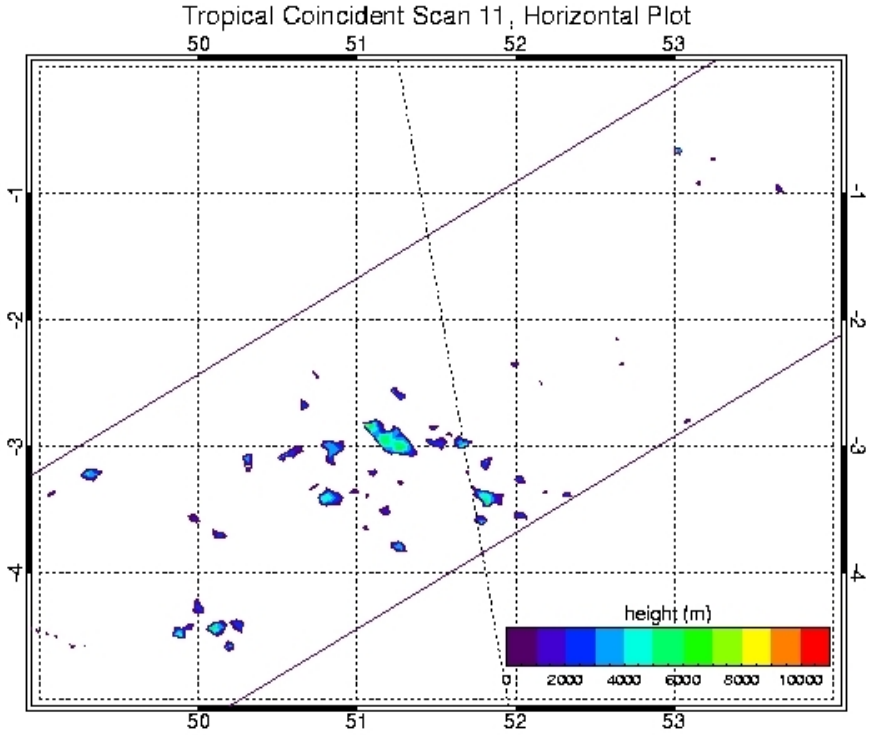

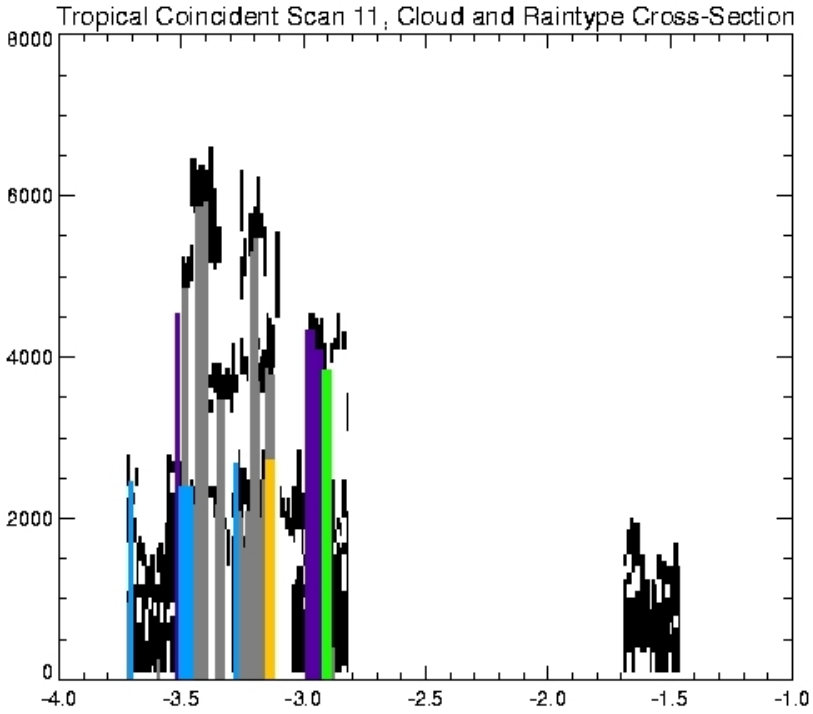

Coincident Scan 12:
GLAS orbital file GLA09_026_2103_001_1331_0_01_0001.DAT
TRMM orbital file 2A23.031020.33803.6.HDF

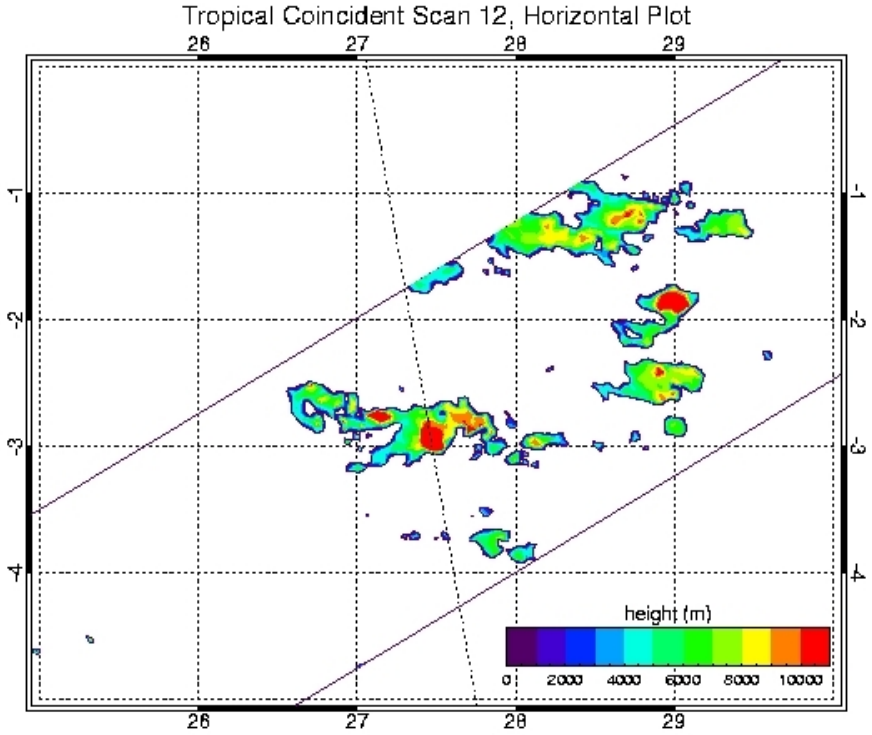

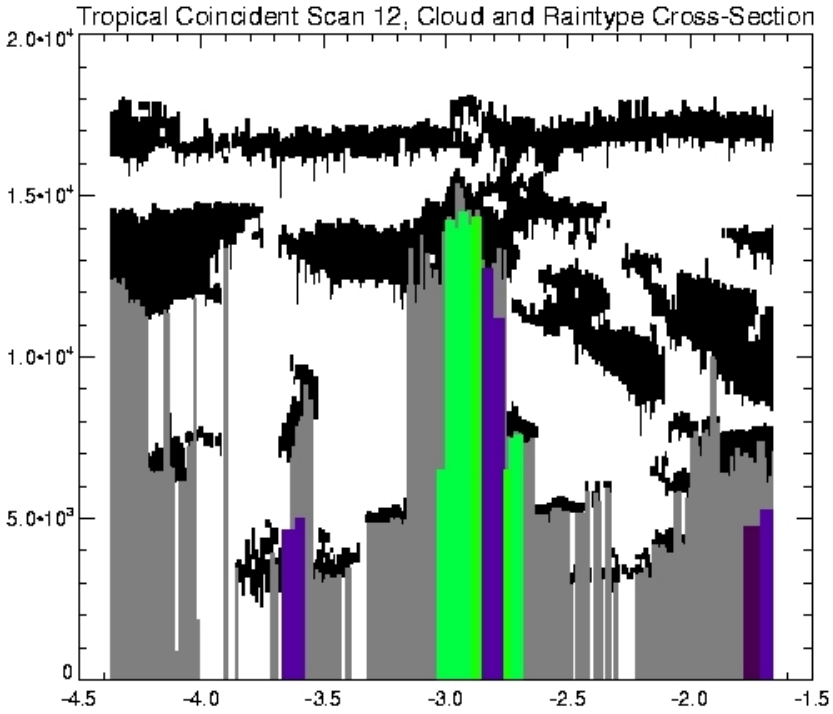

Coincident Scan 13:
GLAS orbital file GLA09_026_2103_001_1331_0_01_0001.DAT
TRMM orbital file 2A23.031020.33804.6.HDF

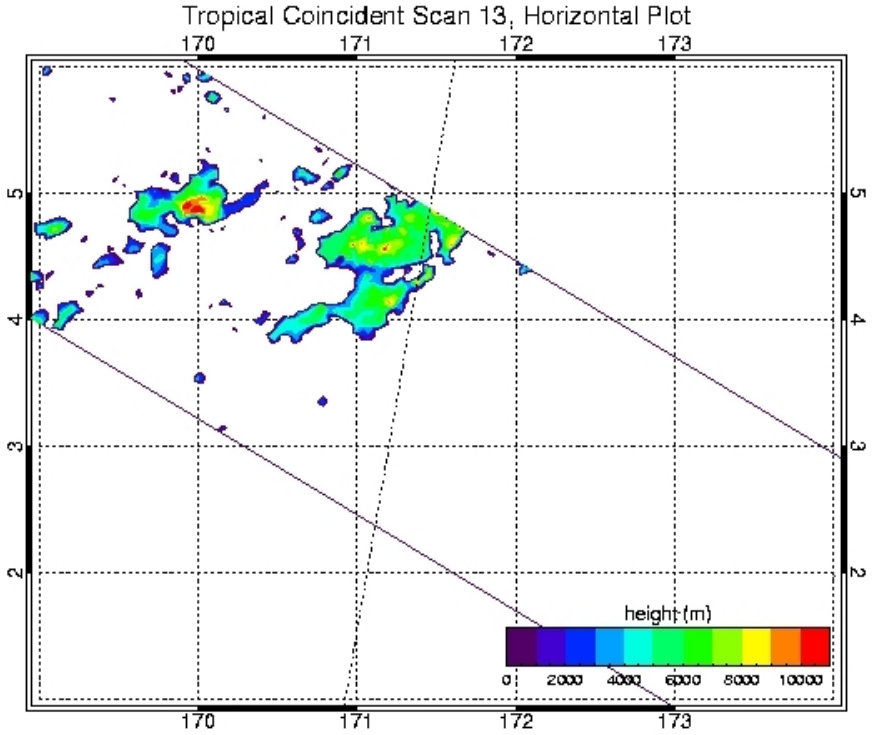

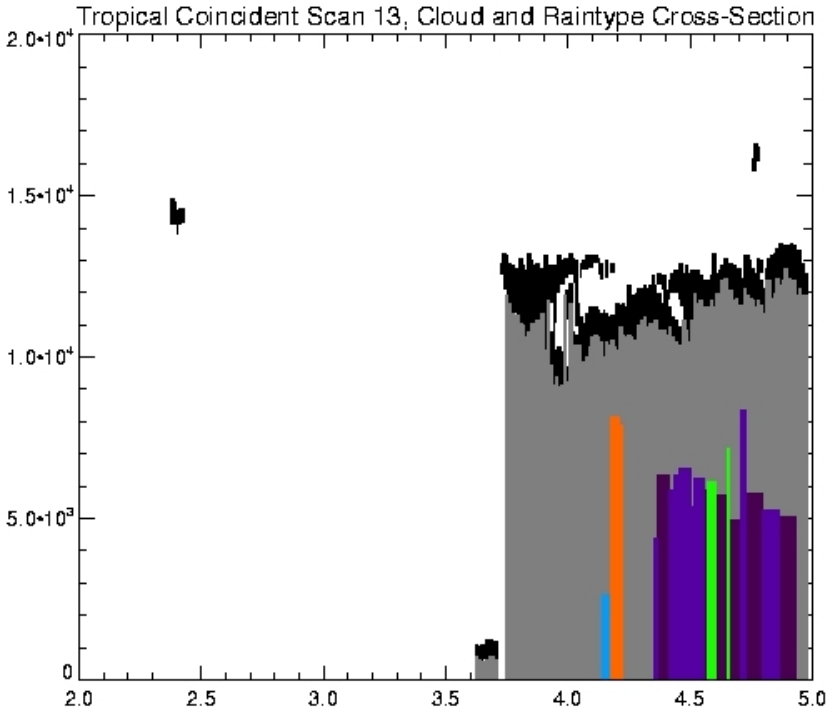

Coincident Scan 14:
GLAS orbital file GLA09_026_2103_002_0001_0_01_0001.DAT
TRMM orbital file 2A23.031022.33823.6.HDF

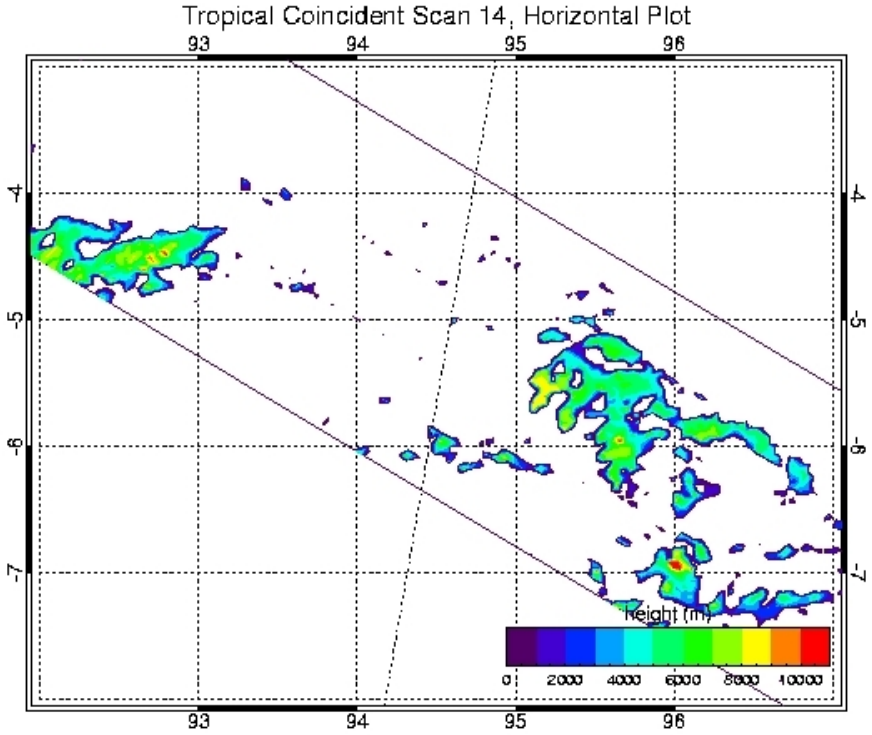

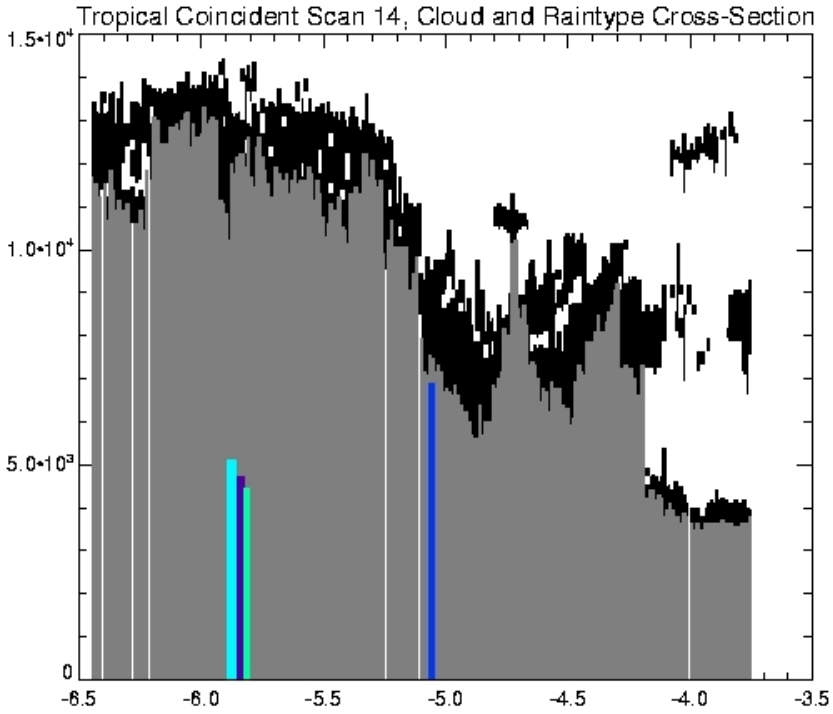

Coincident Scan 15:
GLAS orbital file GLA09_026_2103_002_0001_0_01_0001.DAT
TRMM orbital file 2A23.031022.33824.6.HDF

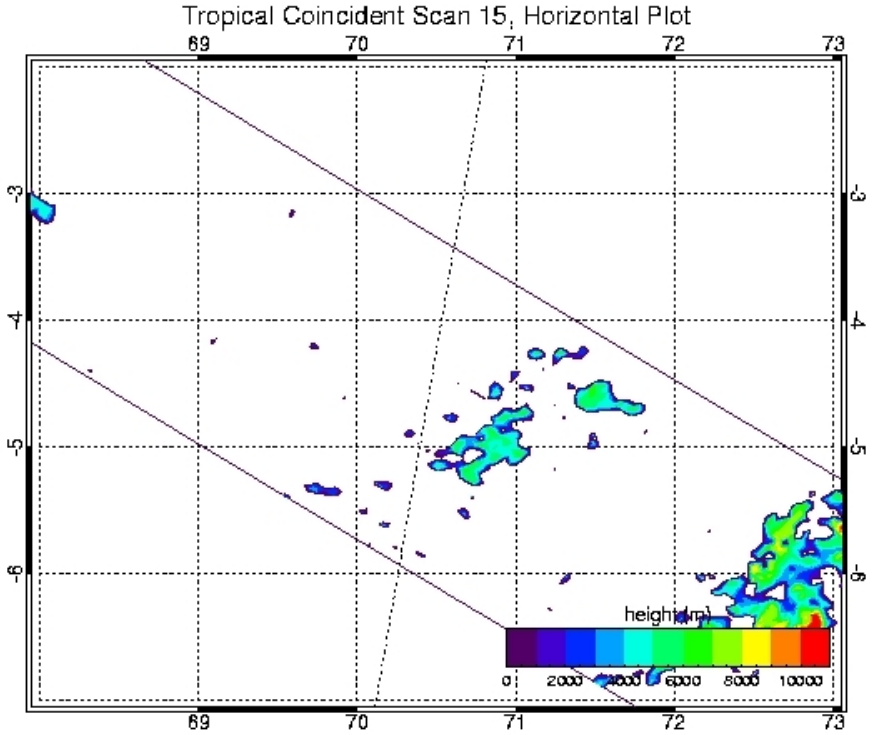

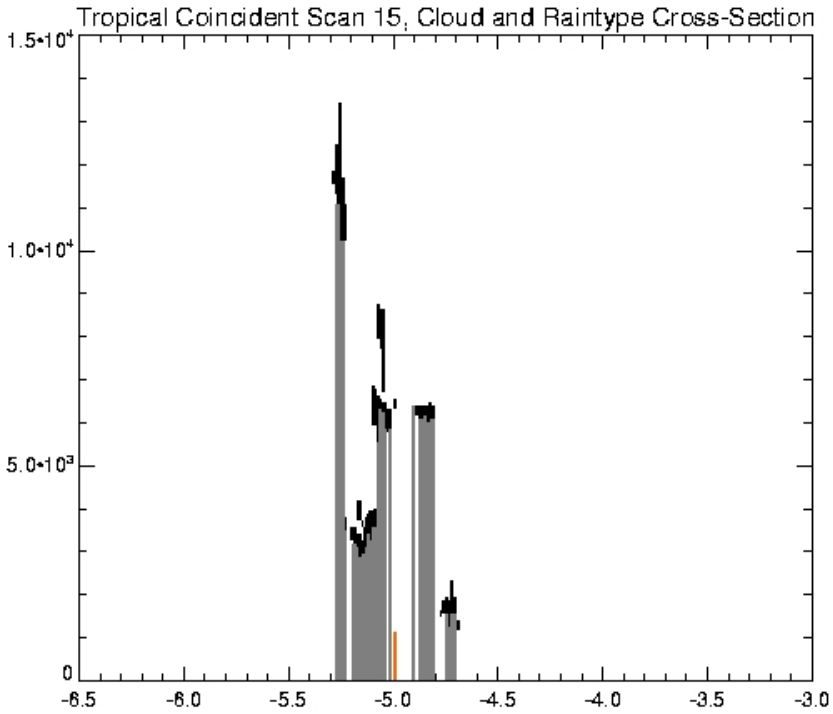

Coincident Scan 16:
GLAS orbital file GLA09_026_2103_002_0001_0_01_0001.DAT
TRMM orbital file 2A23.031022.33826.6.HDF

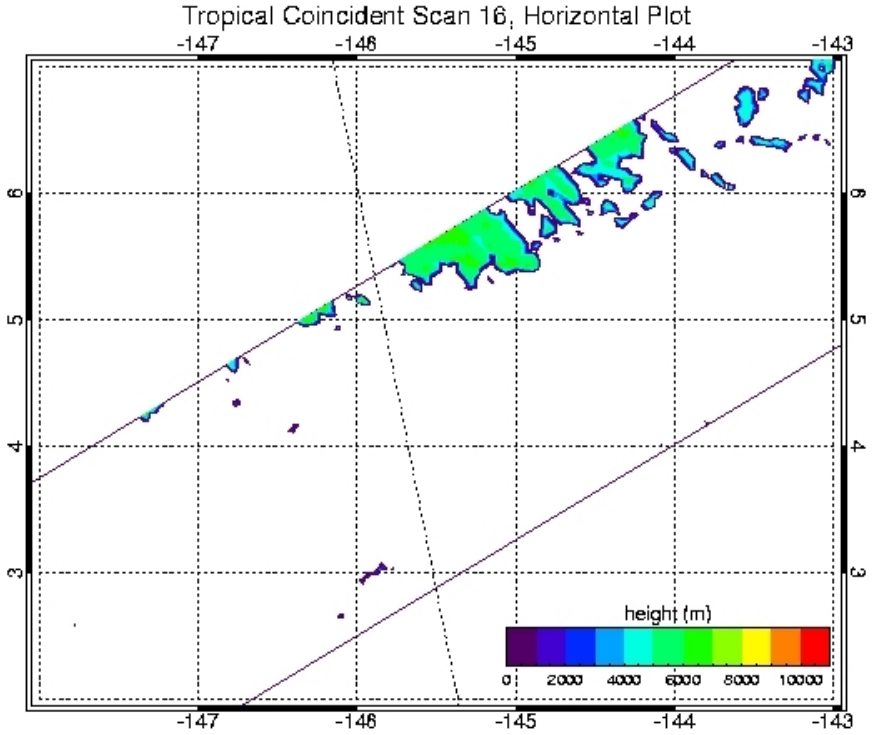

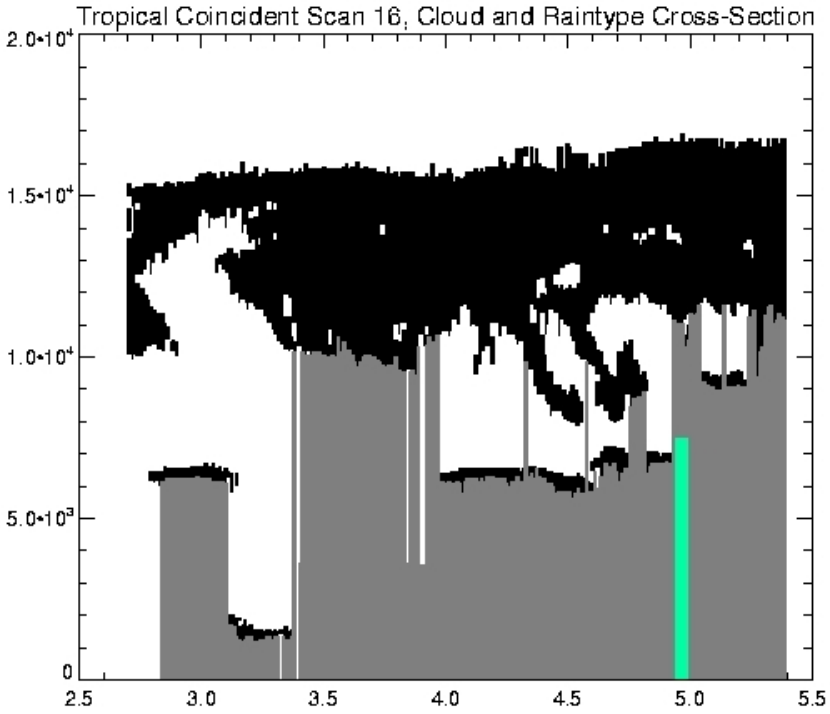

Coincident Scan 17:
GLAS orbital file GLA09_026_2103_002_0001_0_01_0001.DAT
TRMM orbital file 2A23.031022.33826.6.HDF

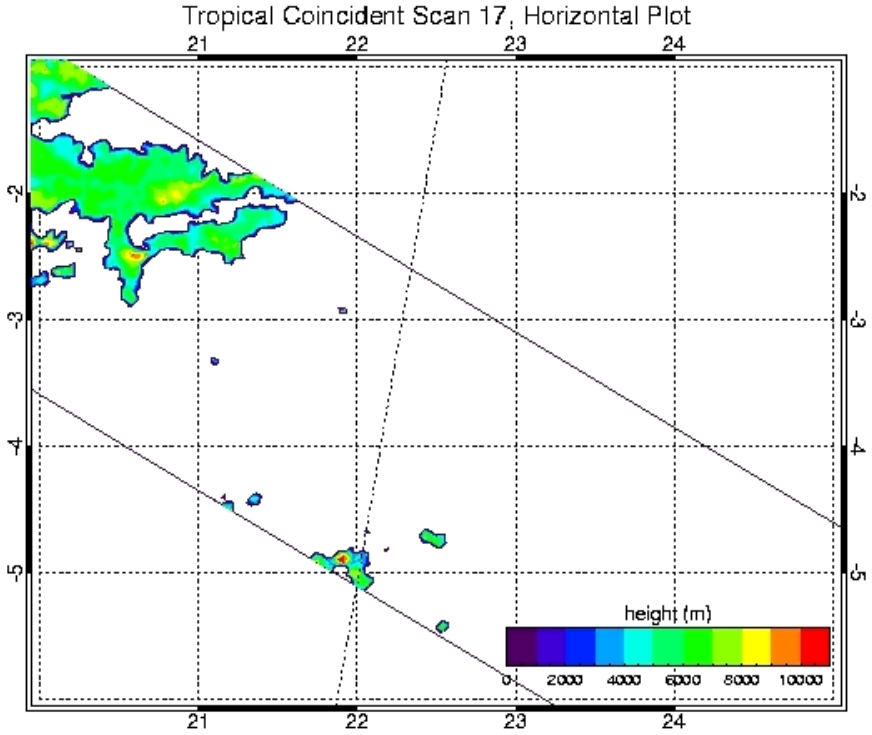

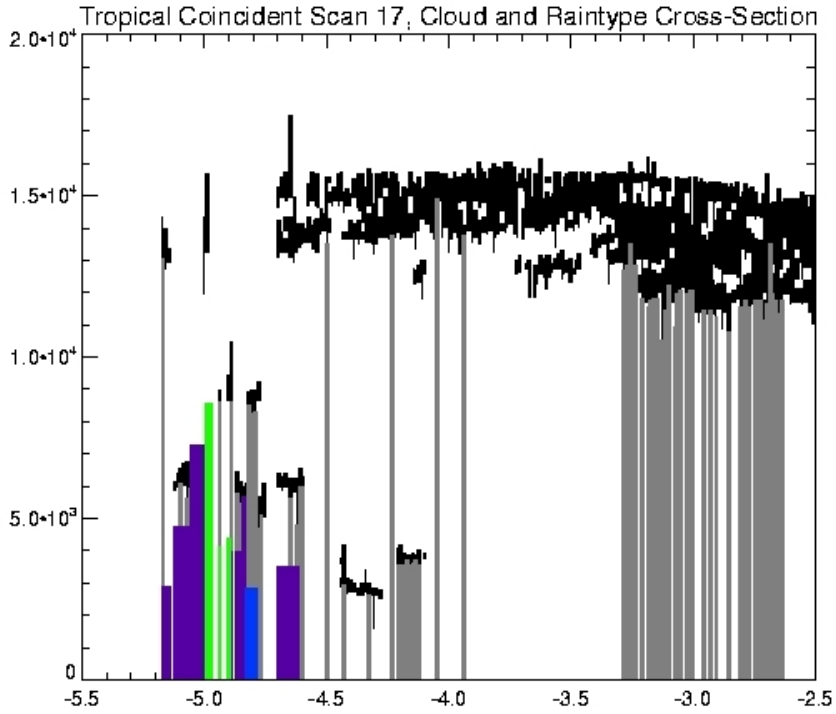

Coincident Scan 18:
GLAS orbital file GLA09_026_2103_002_0001_0_01_0001.DAT
TRMM orbital file 2A23.031022.33827.6.HDF

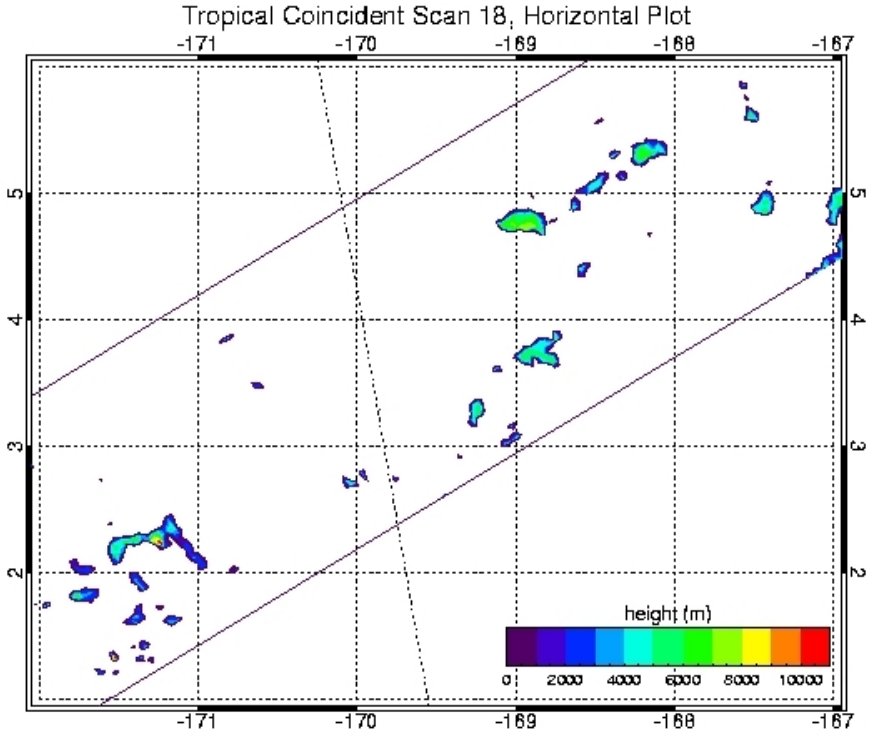

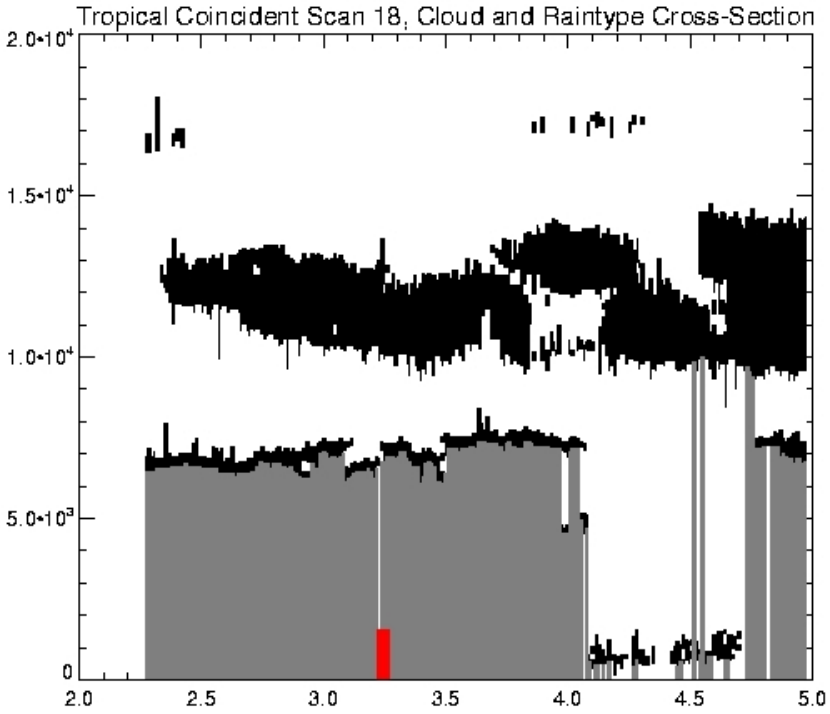

Coincident Scan 19:
GLAS orbital file GLA09_026_2103_002_0015_0_01_0001.DAT
TRMM orbital file 2A23.031023.33845.6.HDF

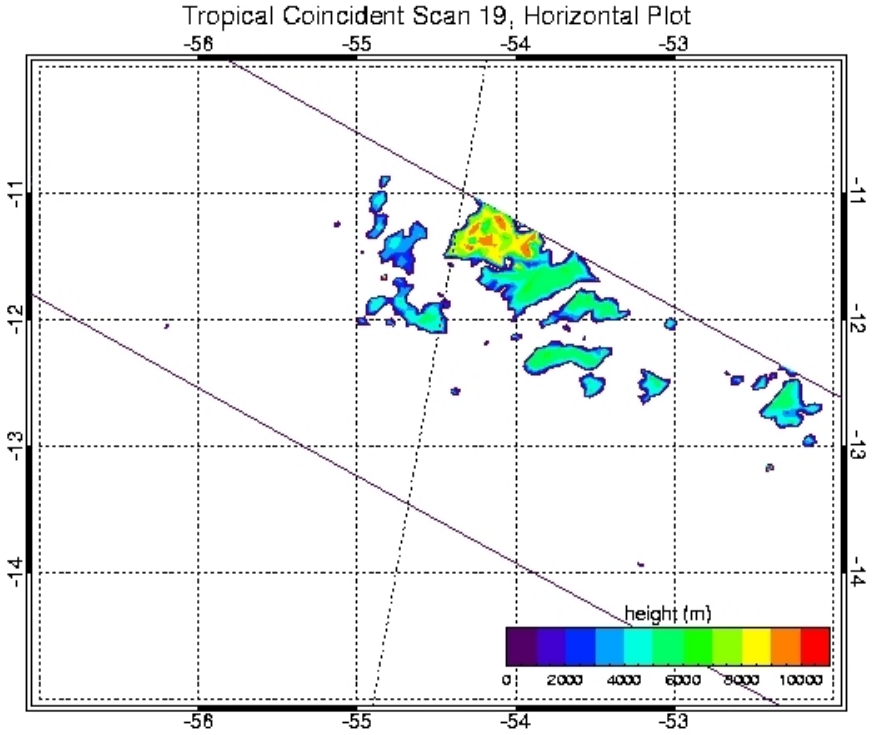

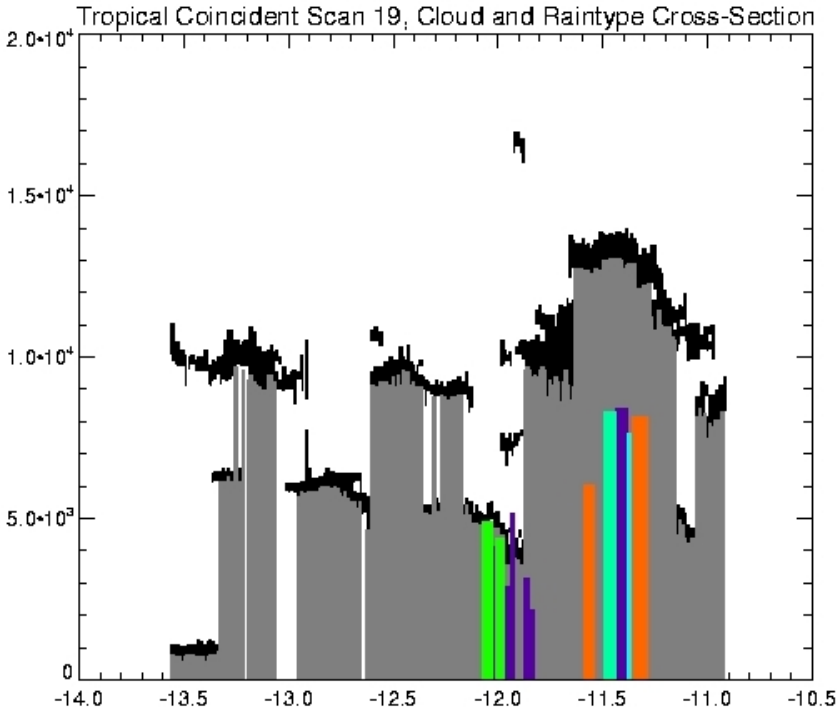

Coincident Scan 20:
GLAS orbital file GLA09_026_2103_002_0015_0_01_0001.DAT
TRMM orbital file 2A23.031023.33846.6.HDF

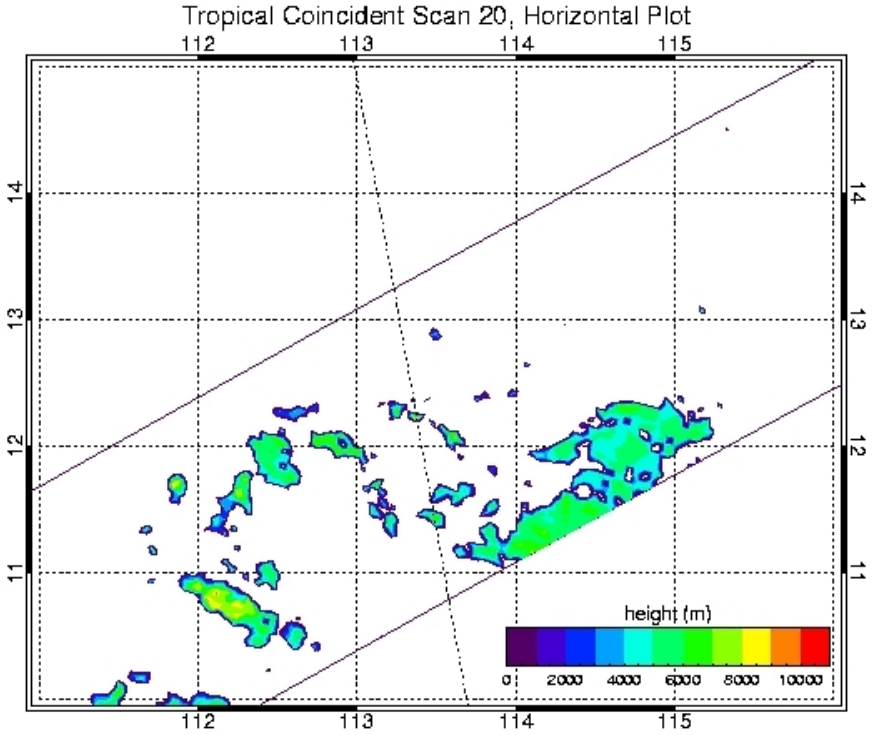

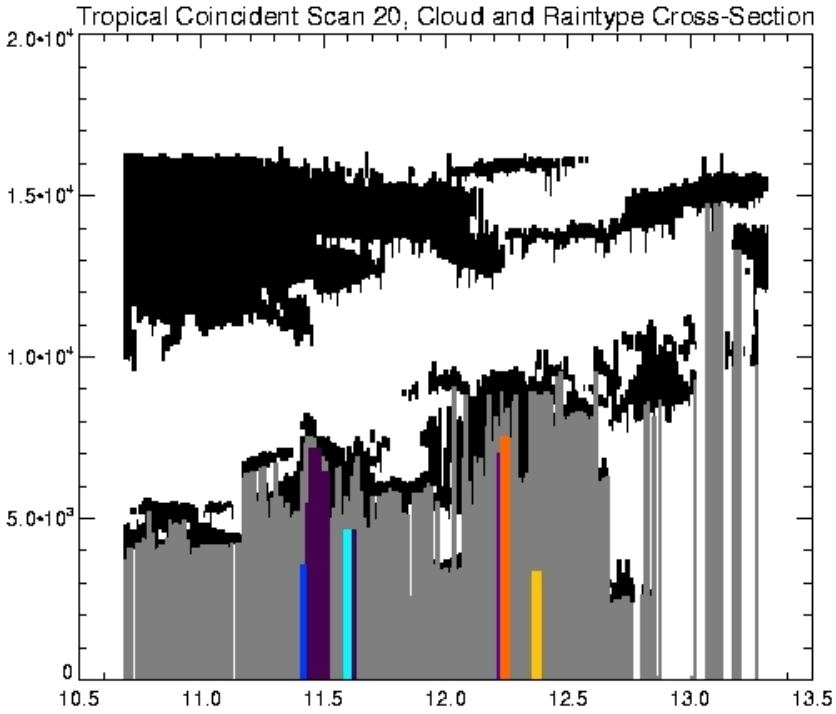

Coincident Scan 21:
GLAS orbital file GLA09_026_2103_002_0015_0_01_0001.DAT
TRMM orbital file 2A23.031023.33848.6.HDF

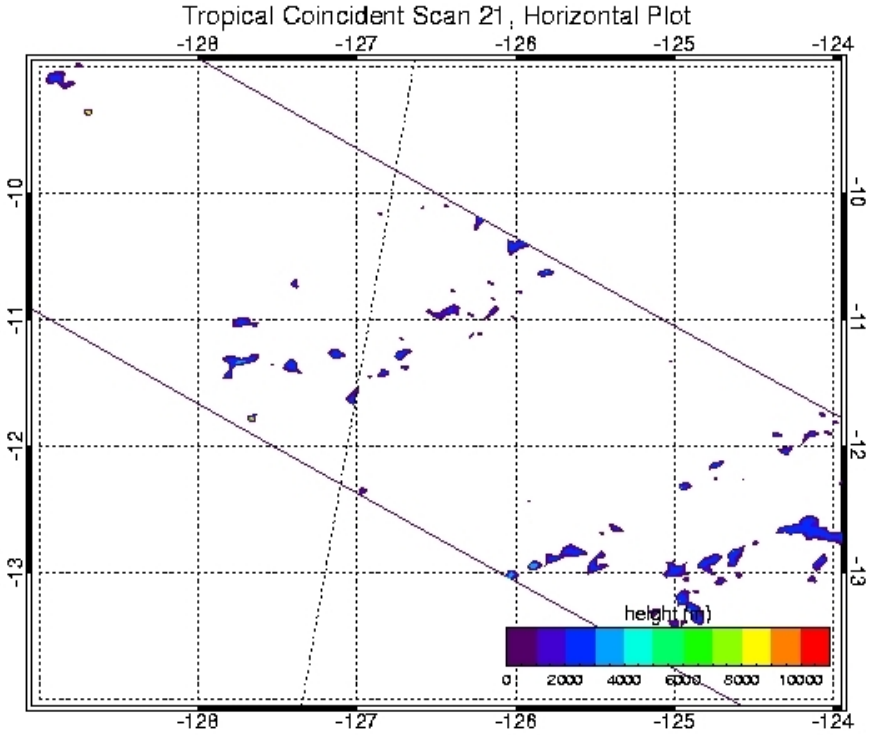

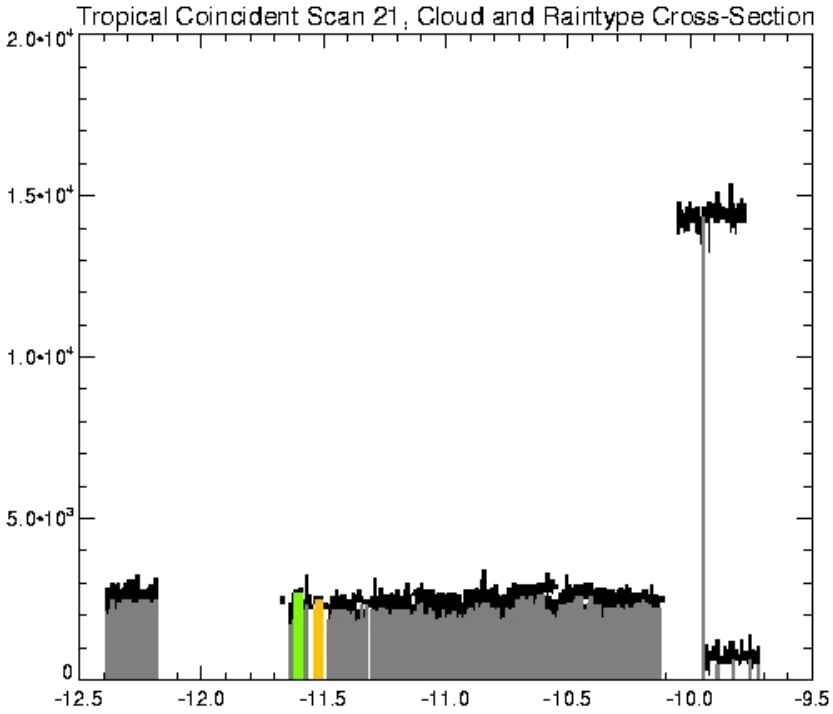

Coincident Scan 22:
GLAS orbital file GLA09_026_2103_002_0029_0_01_0001.DAT
TRMM orbital file 2A23.031023.33849.6.HDF

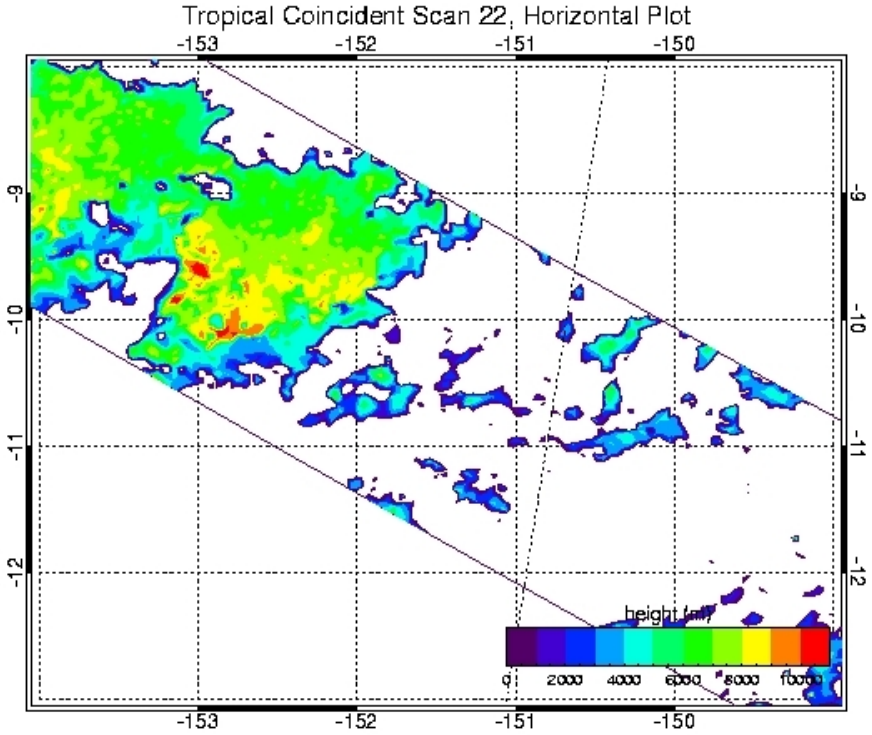

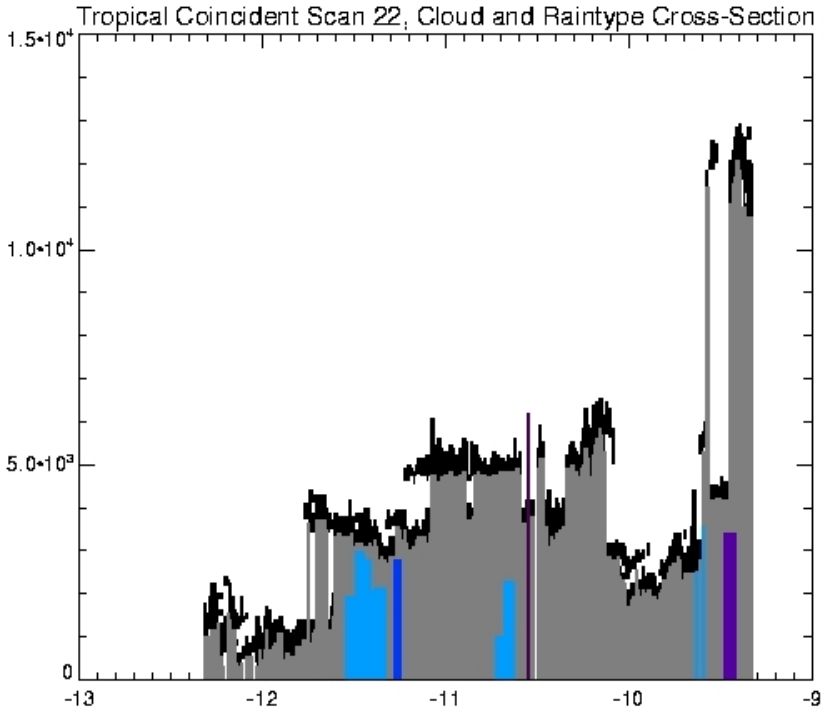

Coincident Scan 23:
GLAS orbital file GLA09_026_2103_002_0029_0_01_0001.DAT
TRMM orbital file 2A23.031023.33850.6.HDF

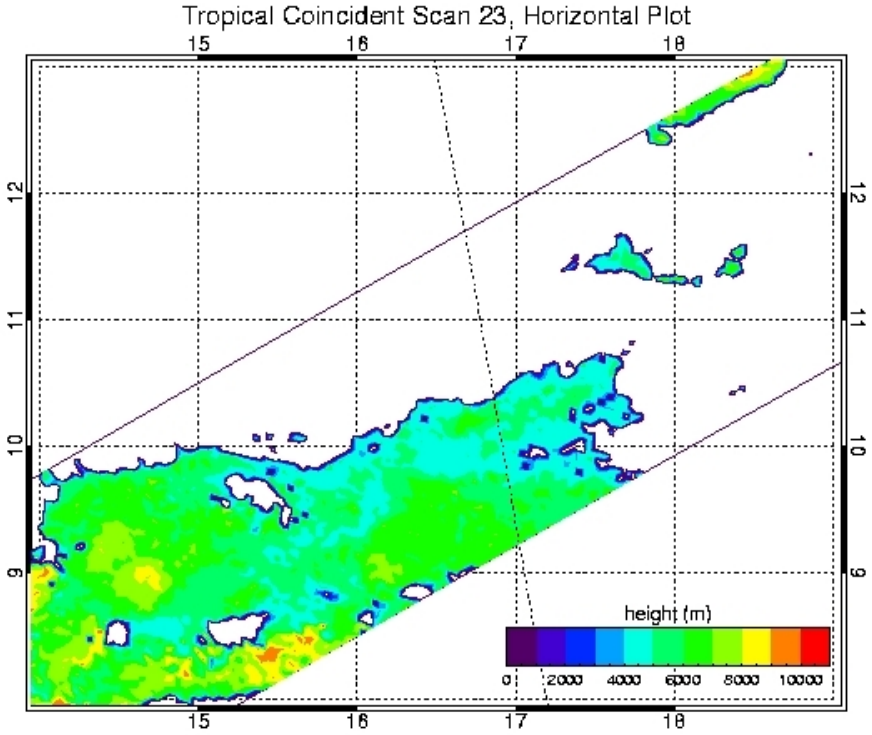

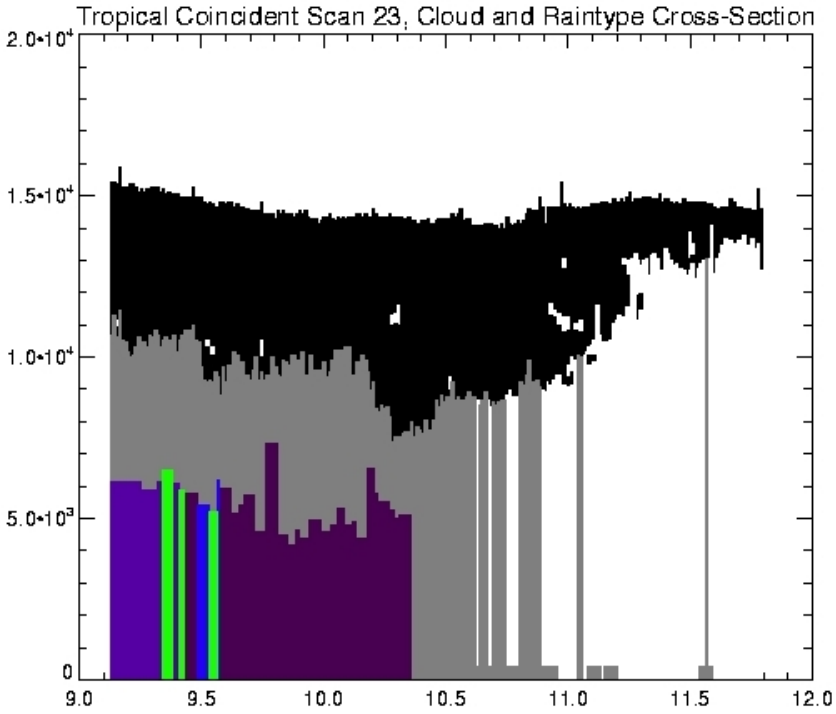

Coincident Scan 24:
GLAS orbital file GLA09_026_2103_002_0029_0_01_0001.DAT
TRMM orbital file 2A23.031023.33850.6.HDF

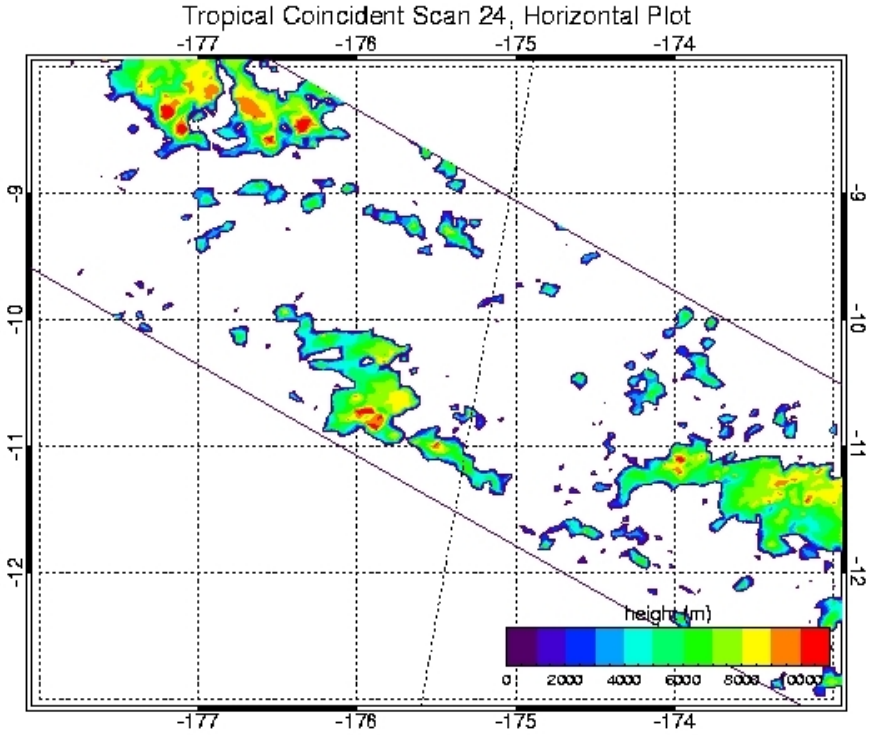

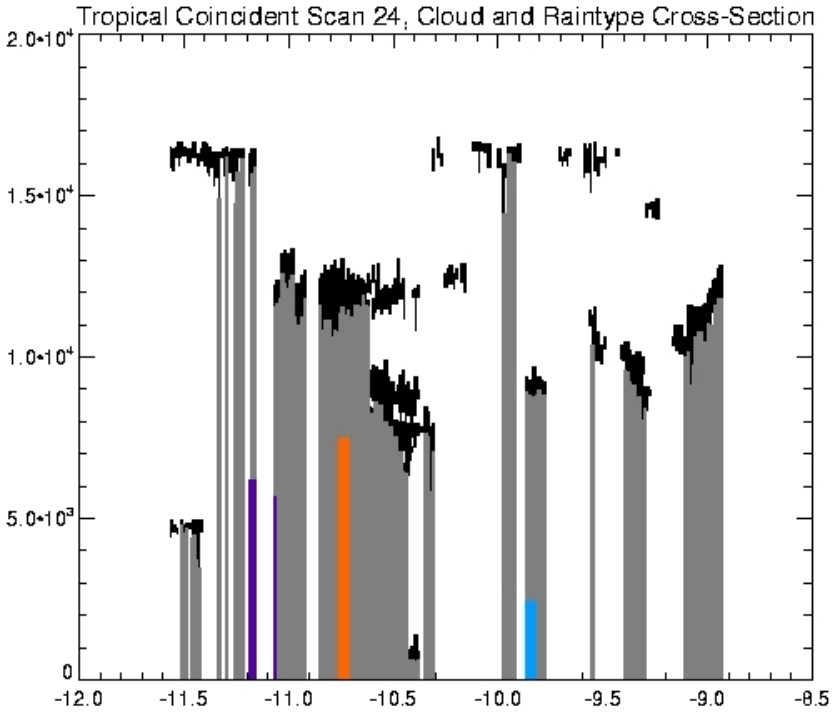

Coincident Scan 25:
GLAS orbital file GLA09_026_2103_002_0029_0_01_0001.DAT
TRMM orbital file 2A23.031023.33851.6.HDF

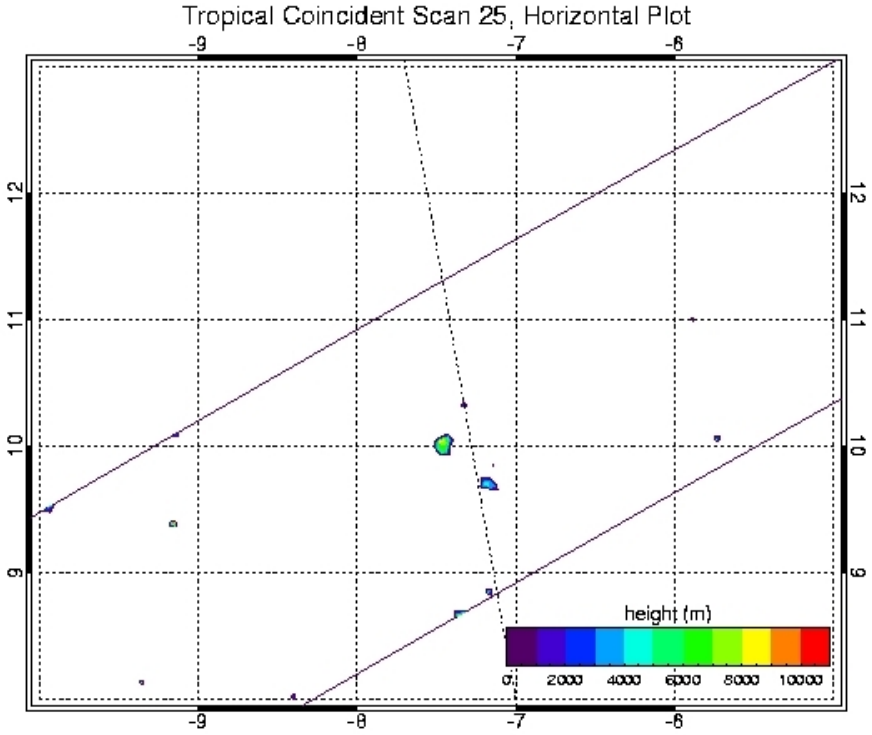

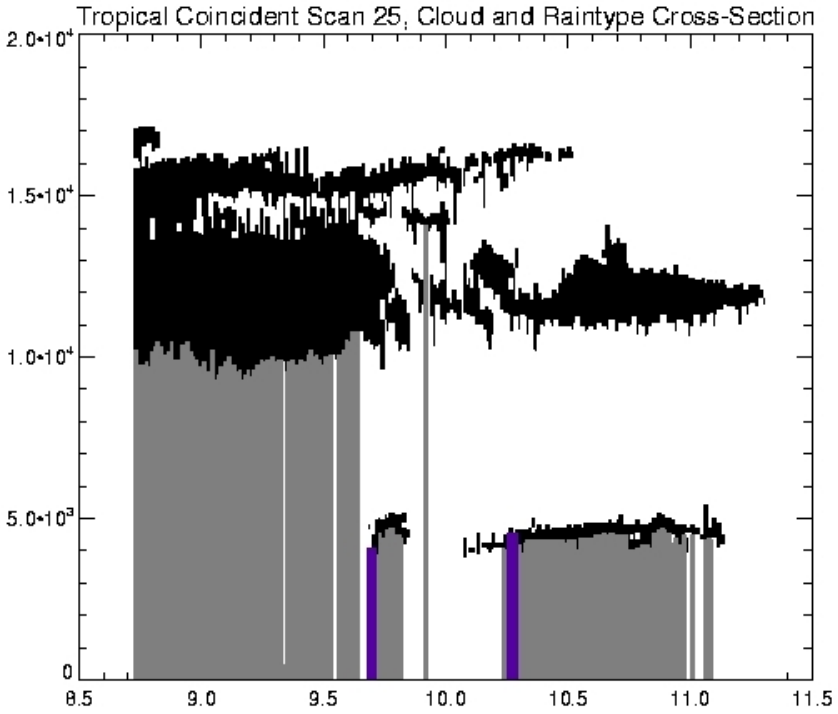

Coincident Scan 26:
GLAS orbital file GLA09_026_2103_002_0043_0_01_0001.DAT
TRMM orbital file 2A23.031024.33868.6.HDF

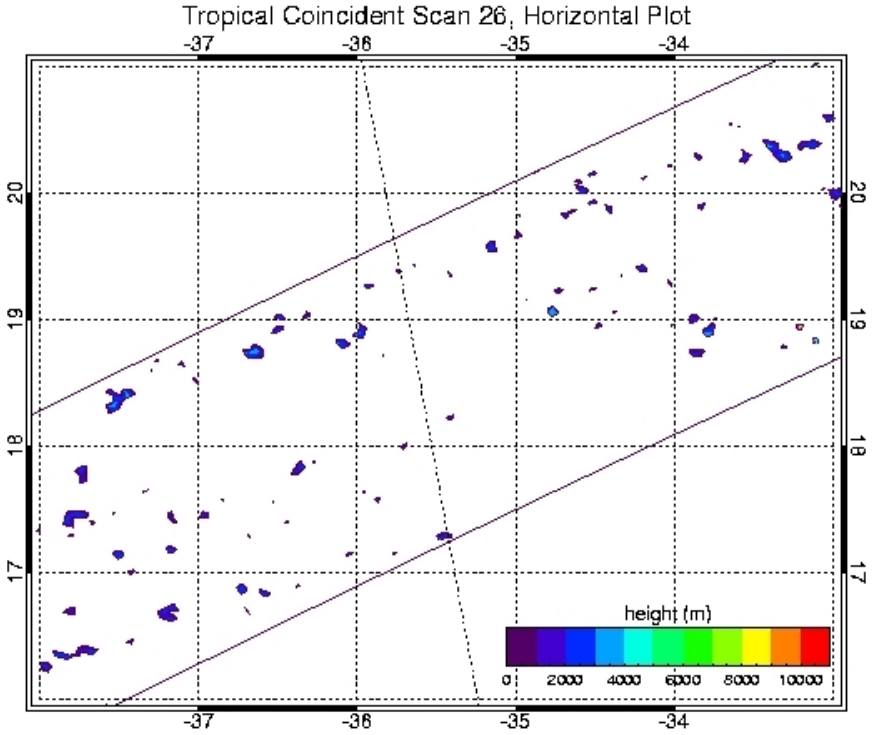

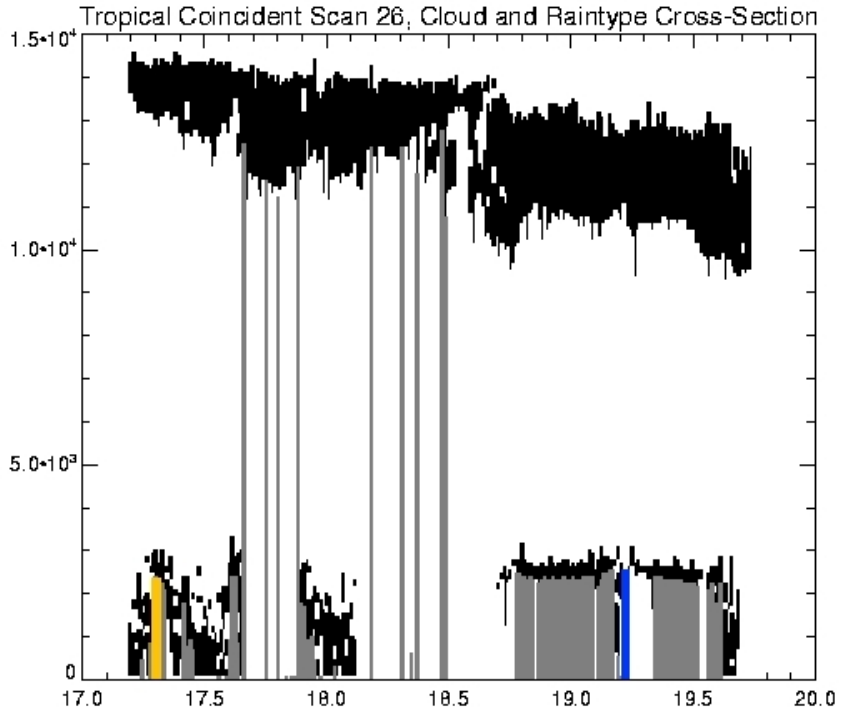

Coincident Scan 27:
GLAS orbital file GLA09_026_2103_002_0043_0_01_0001.DAT
TRMM orbital file 2A23.031025.33874.6.HDF

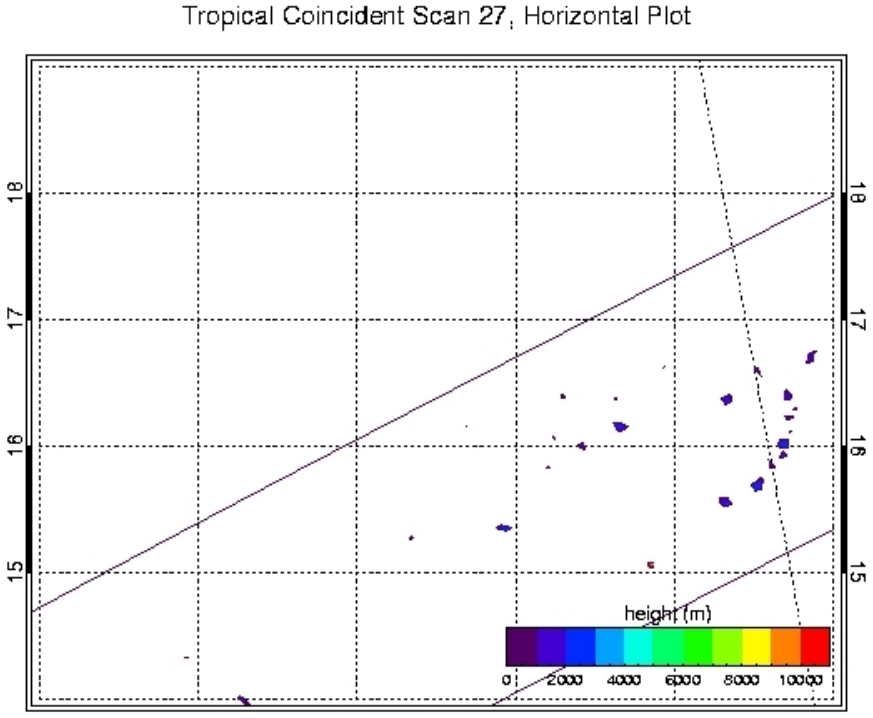

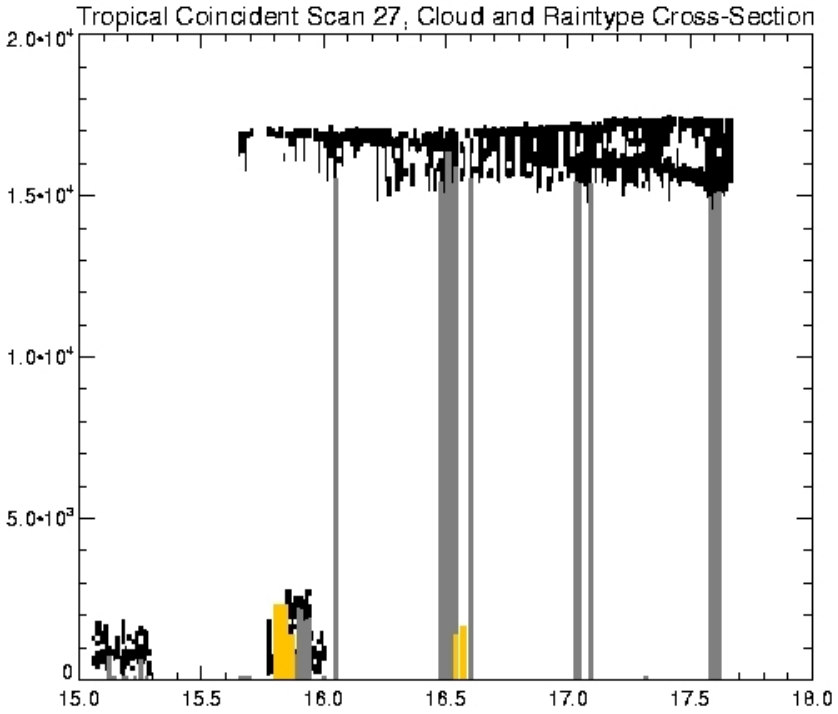

Coincident Scan 28:
GLAS orbital file GLA09_026_2103_002_0309_0_01_0001.DAT
TRMM orbital file 2A23.031111.34148.6.HDF

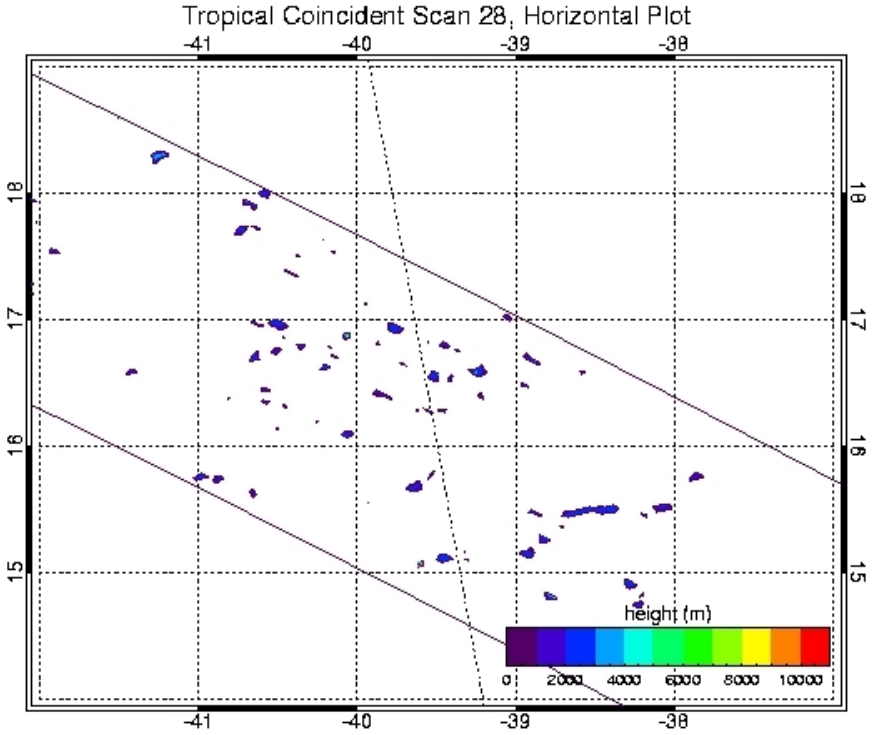

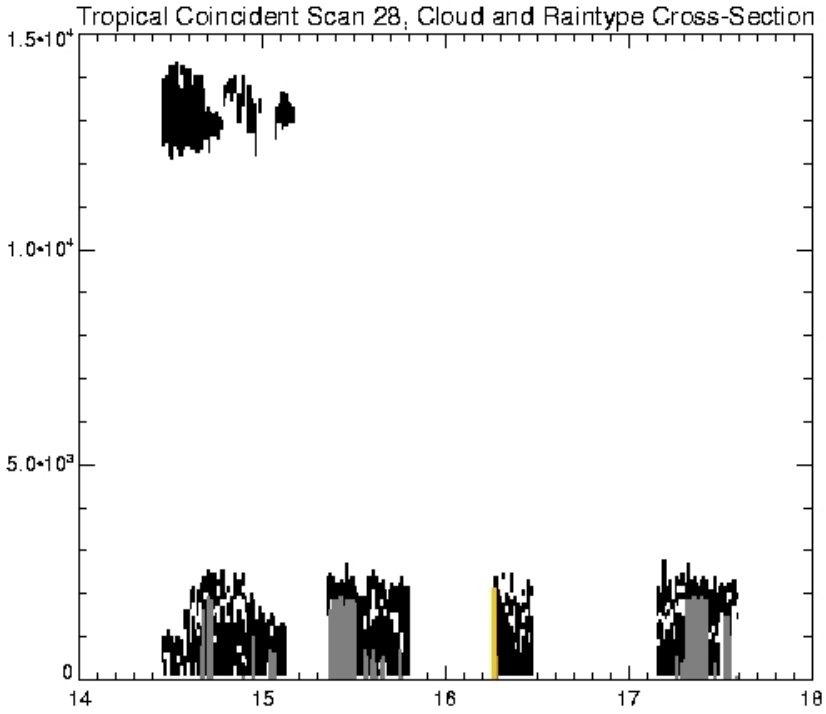

Coincident Scan 29:
GLAS orbital file GLA09_026_2103_002_0309_0_01_0001.DAT
TRMM orbital file 2A23.031111.34149.6.HDF

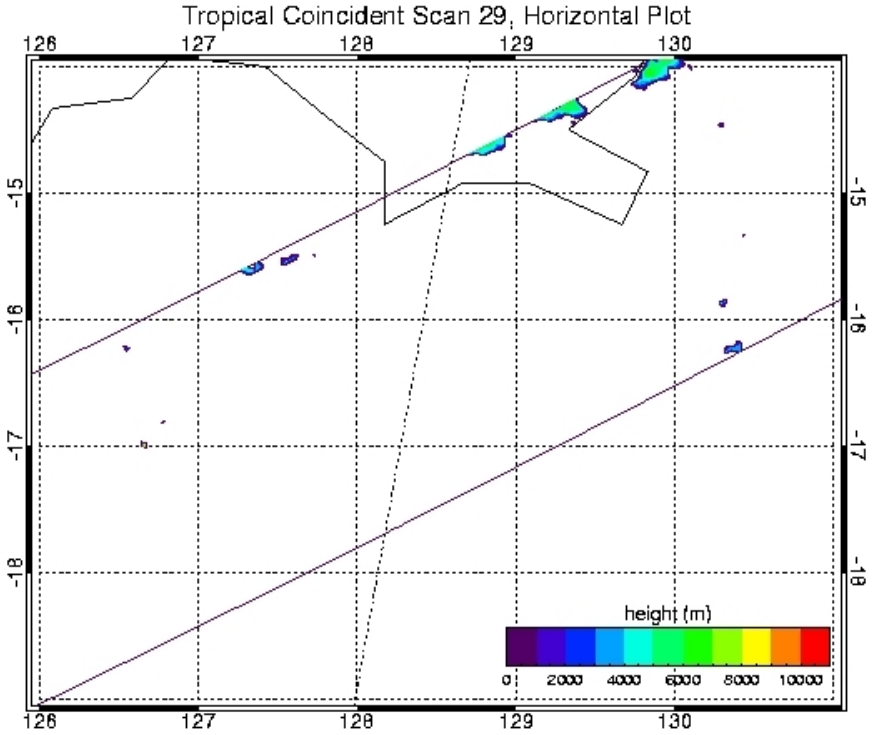

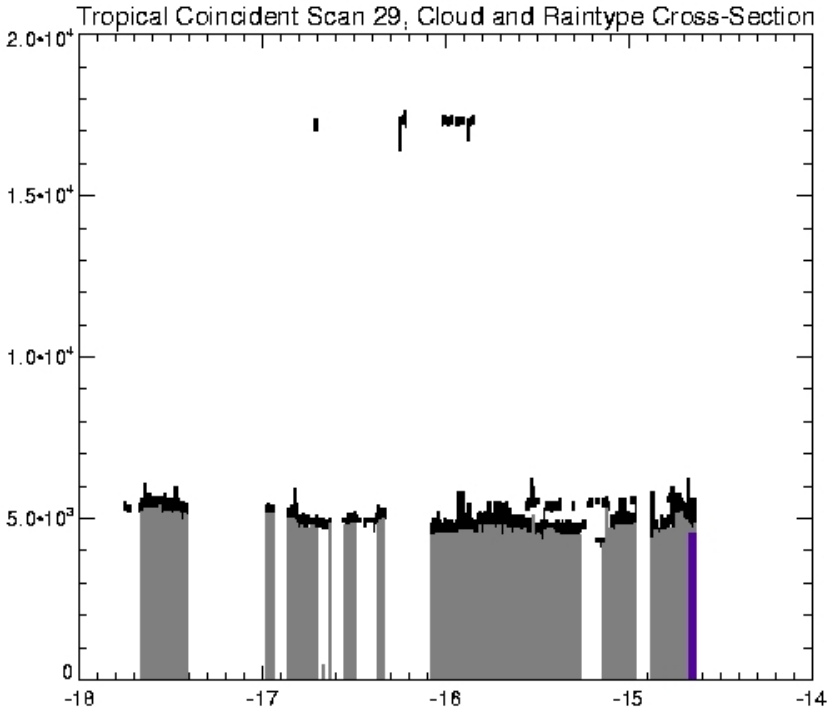

Coincident Scan 30:
GLAS orbital file GLA09_026_2103_002_0309_0_01_0001.DAT
TRMM orbital file 2A23.031111.34149.6.HDF

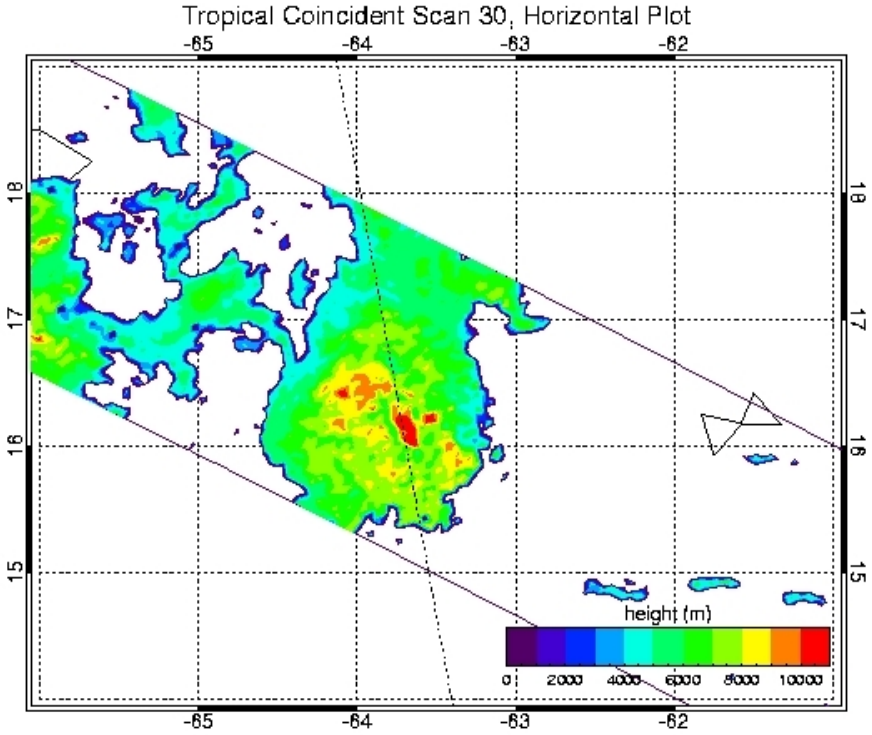

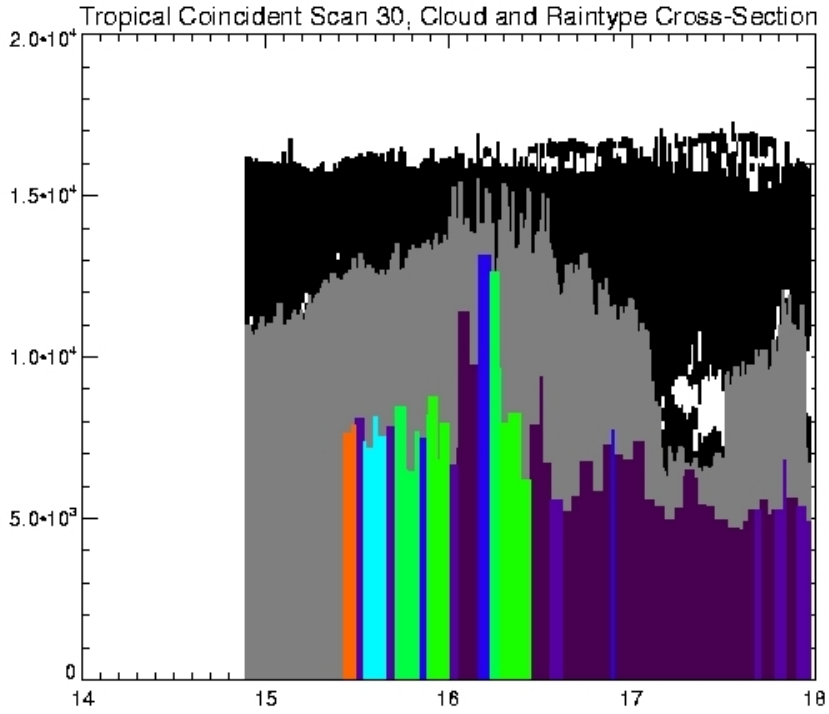

Coincident Scan 31:
GLAS orbital file GLA09_026_2103_002_0309_0_01_0001.DAT
TRMM orbital file 2A23.031112.34150.6.HDF

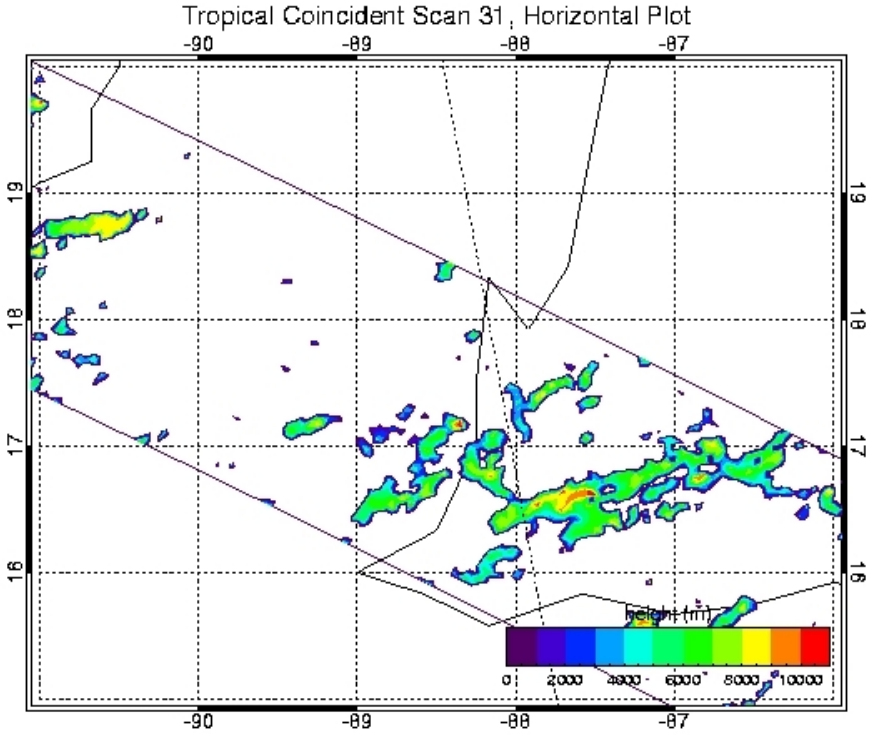

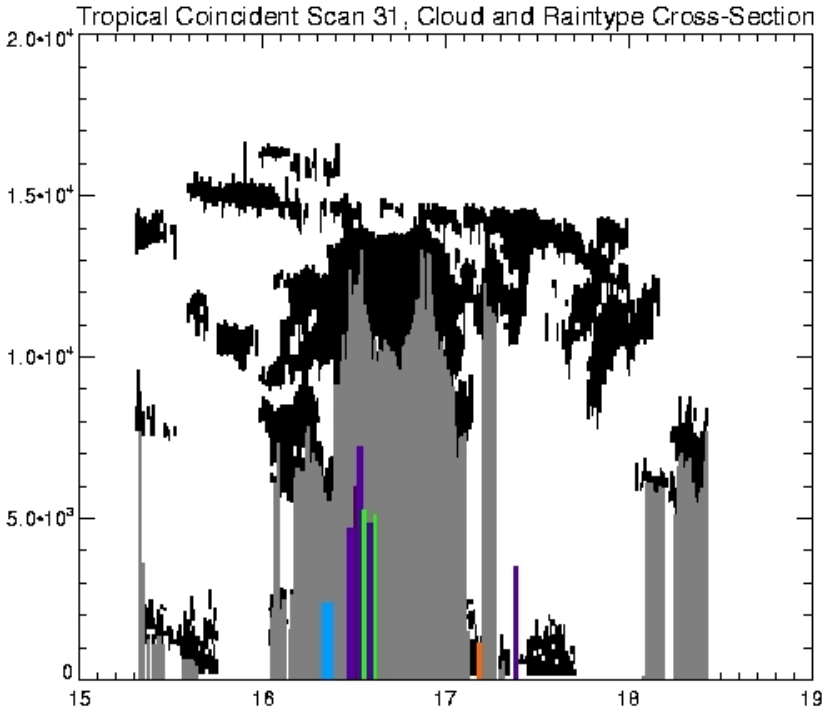

Coincident Scan 32:
GLAS orbital file GLA09_026_2103_002_0309_0_01_0001.DAT
TRMM orbital file 2A23.031112.34152.6.HDF

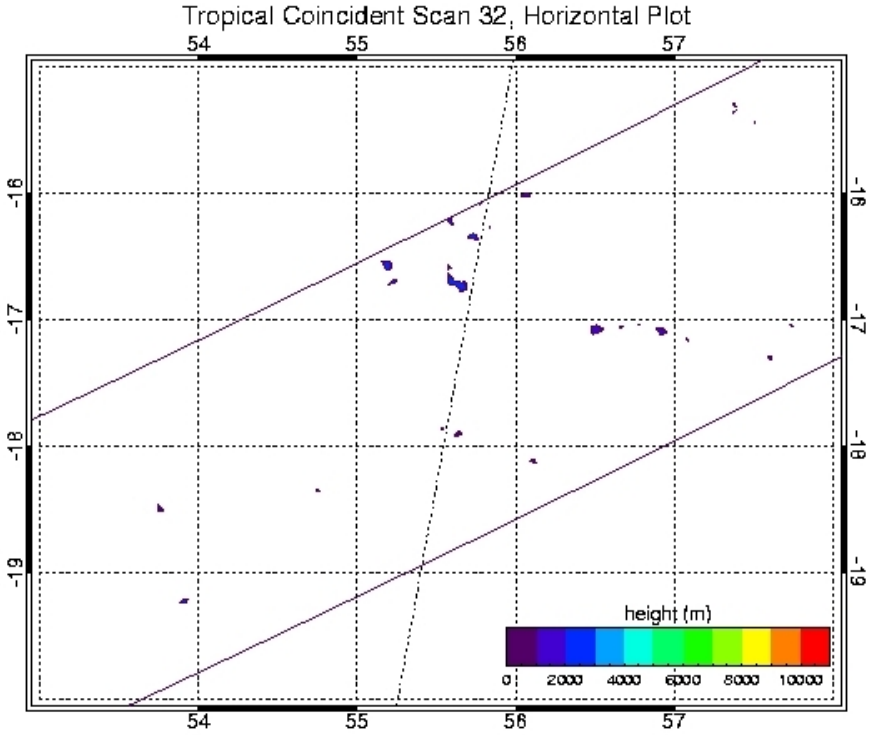

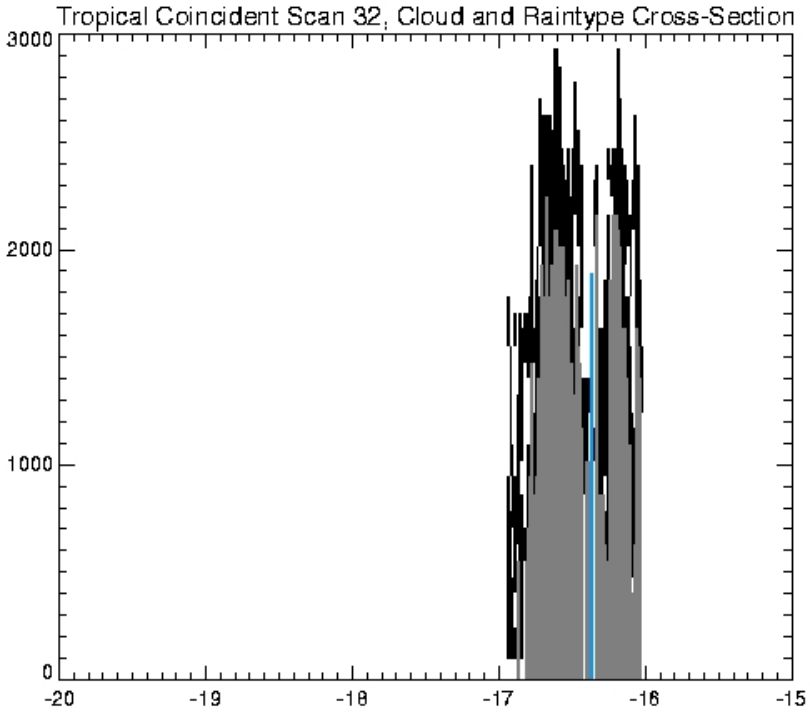

Coincident Scan 33:
GLAS orbital file GLA09_026_2103_002_0309_0_01_0001.DAT
TRMM orbital file 2A23.031112.34153.6.HDF

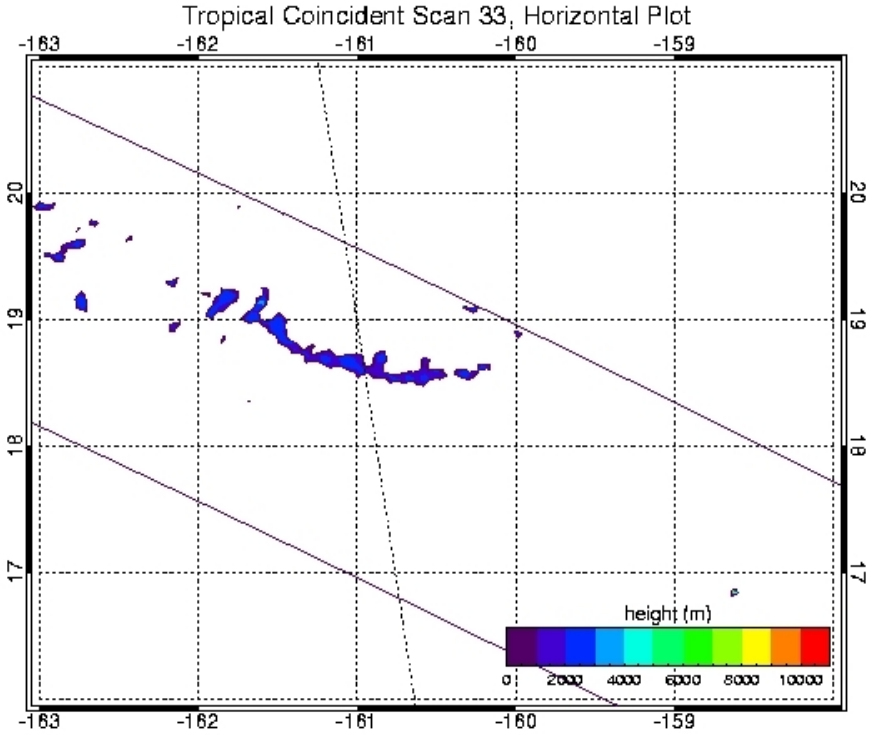

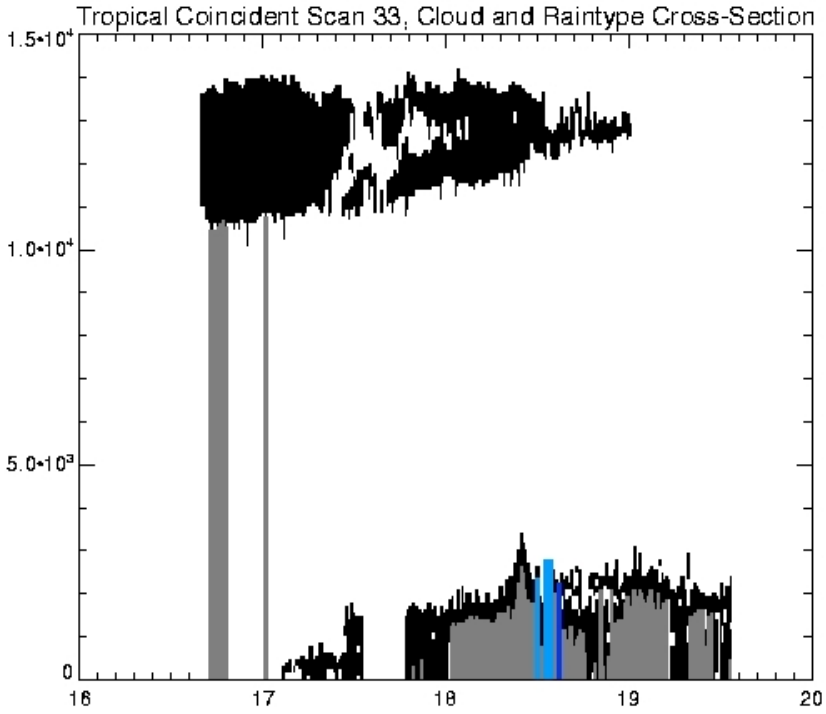

Coincident Scan 34:
GLAS orbital file GLA09_026_2103_002_0323_0_01_0001.DAT
TRMM orbital file 2A23.031113.34171.6.HDF

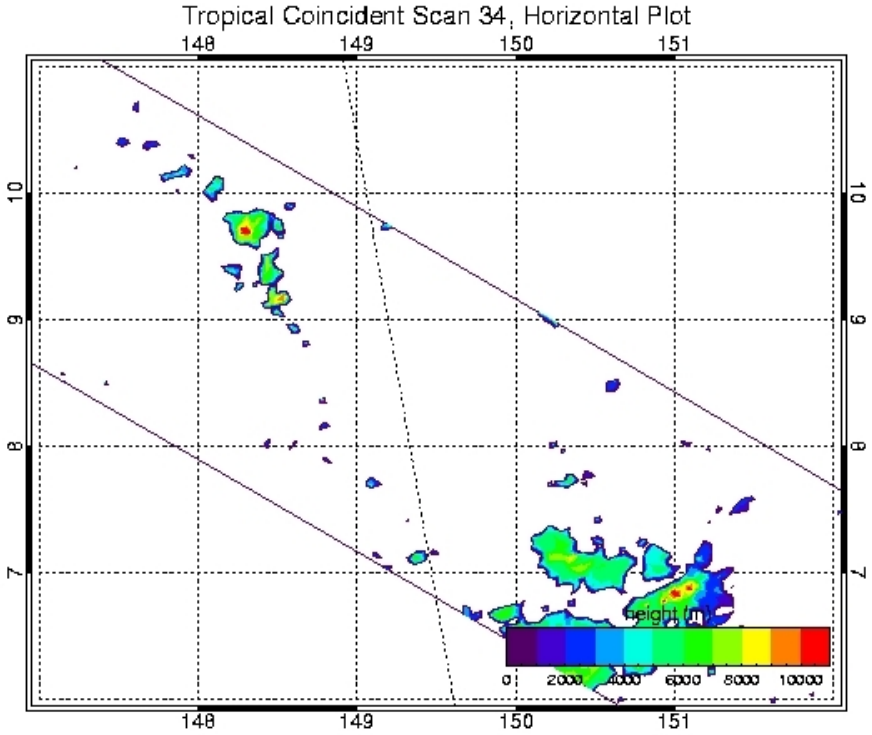

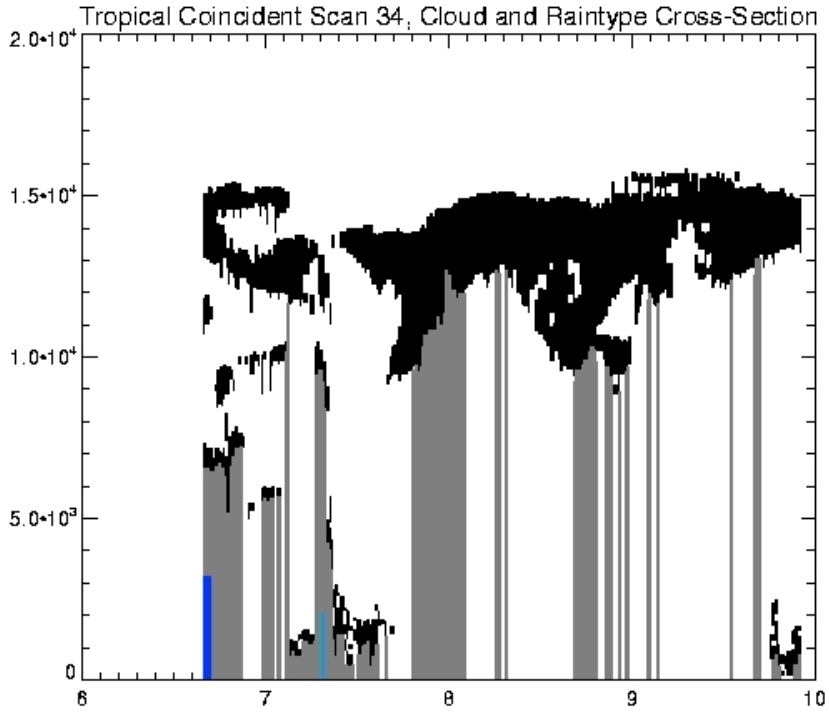

Coincident Scan 35:
GLAS orbital file GLA09_026_2103_002_0337_0_01_0001.DAT
TRMM orbital file 2A23.031113.34172.6.HDF

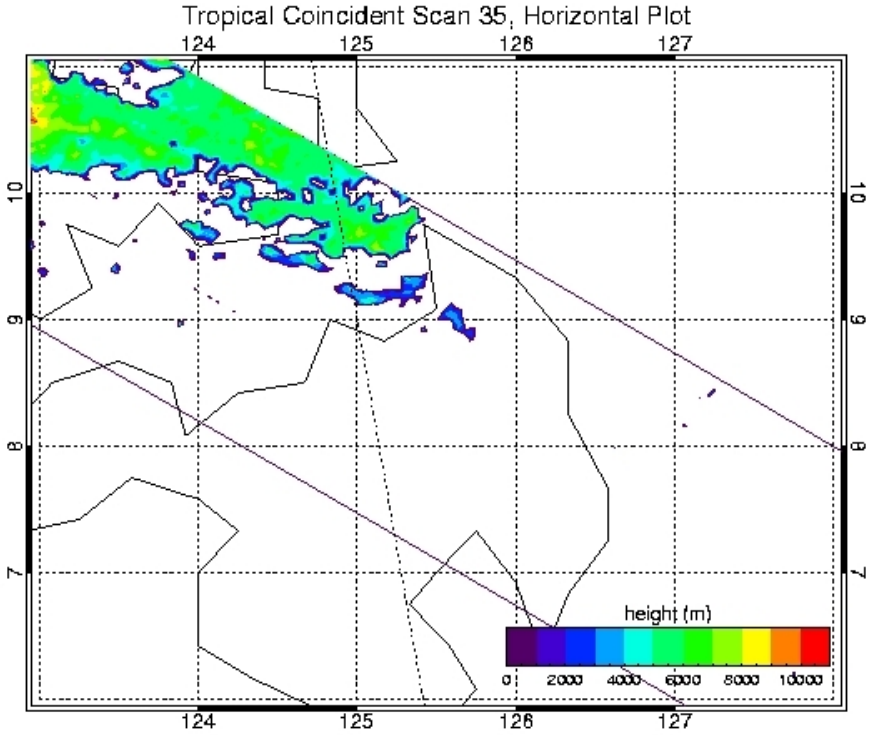

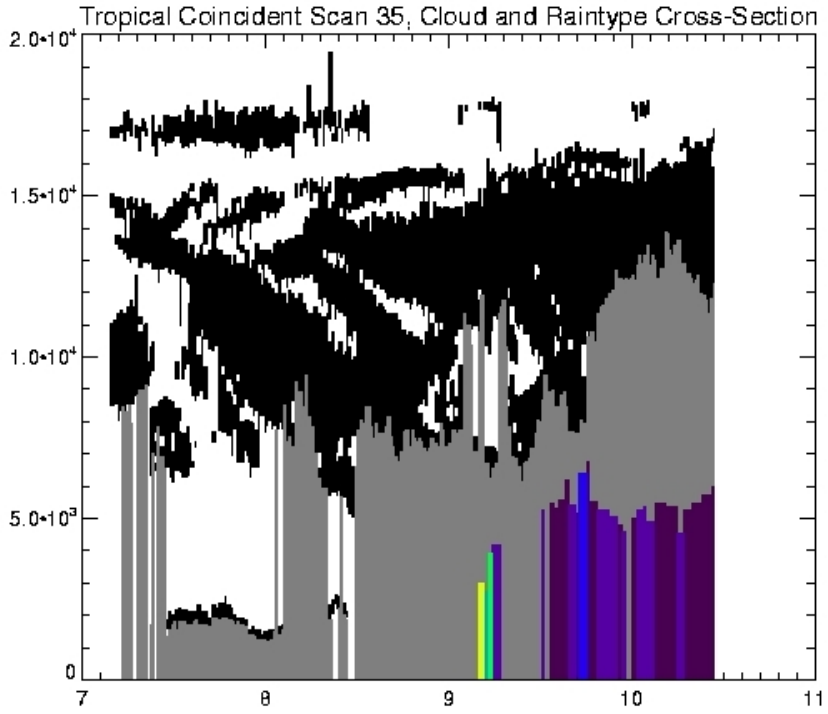

Coincident Scan 36:
GLAS orbital file GLA09_026_2103_002_0337_0_01_0001.DAT
TRMM orbital file 2A23.031113.34173.6.HDF

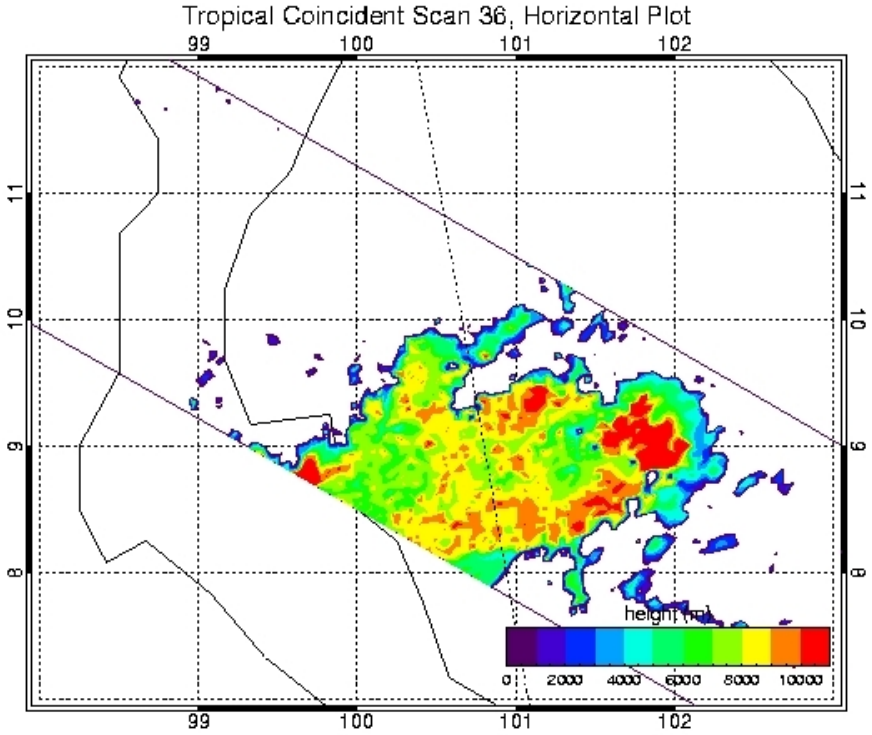

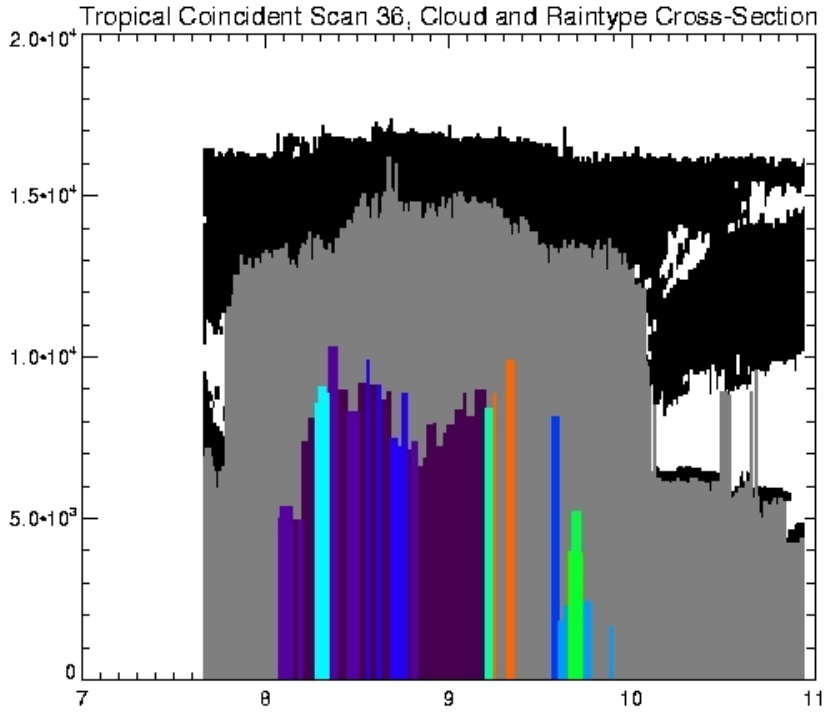

Coincident Scan 37:
GLAS orbital file GLA09_026_2103_002_0337_0_01_0001.DAT
TRMM orbital file 2A23.031113.34175.6.HDF

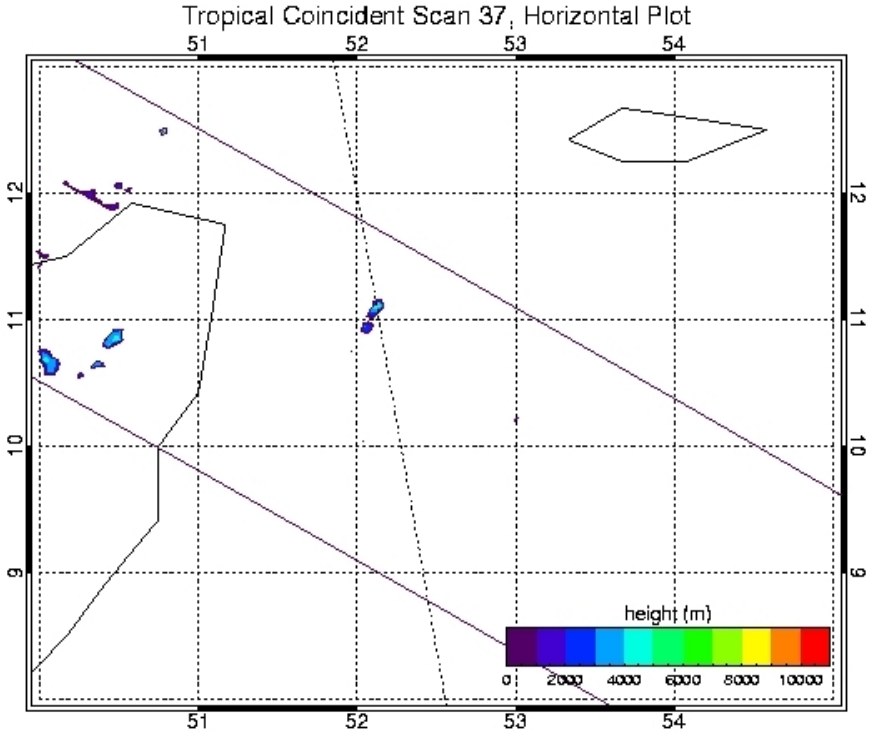

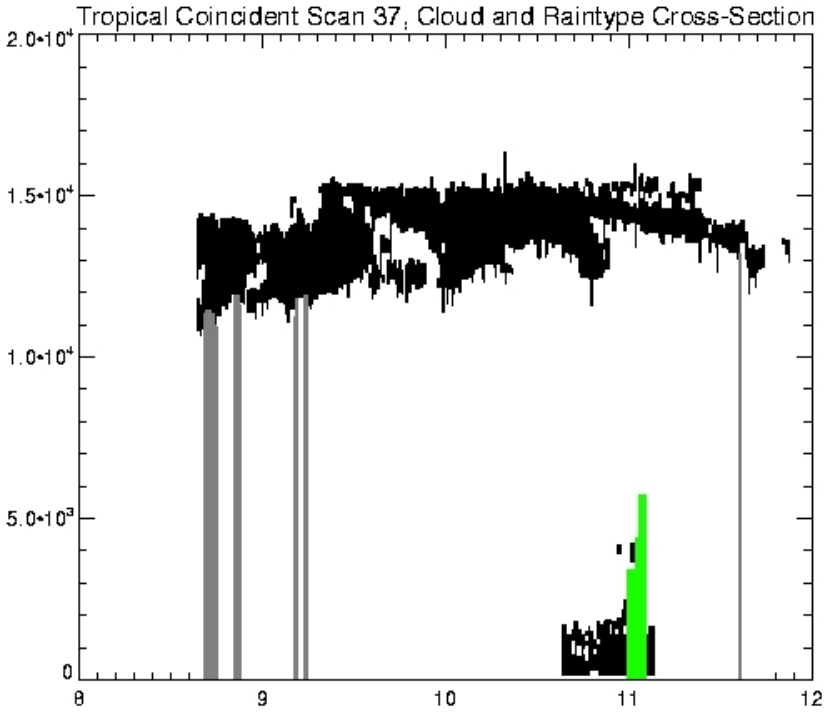

Coincident Scan 38:
GLAS orbital file GLA09_026_2103_002_0337_0_01_0001.DAT
TRMM orbital file 2A23.031113.34177.6.HDF

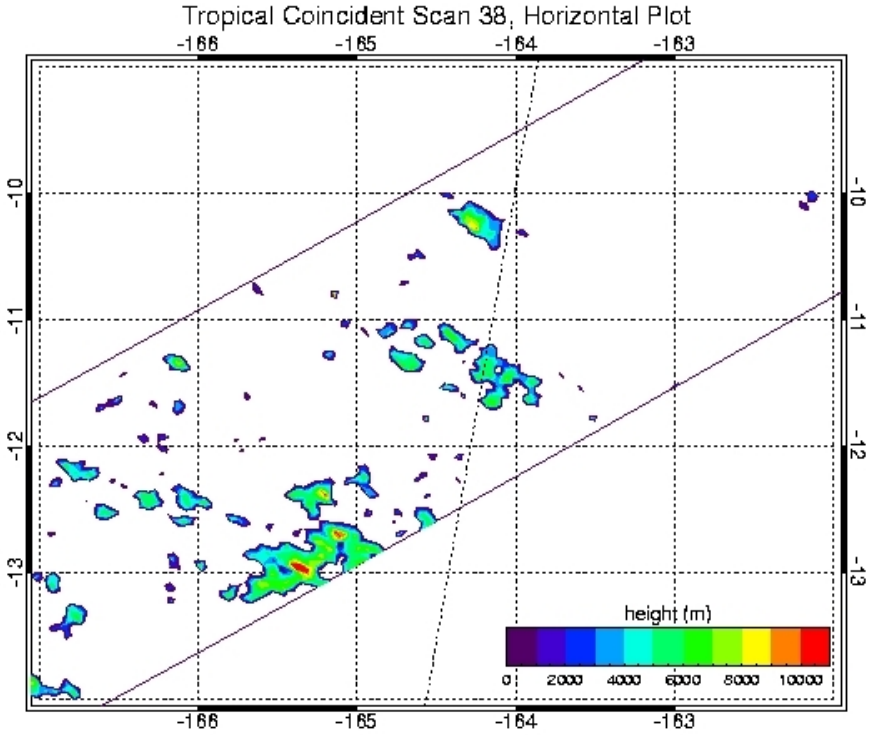

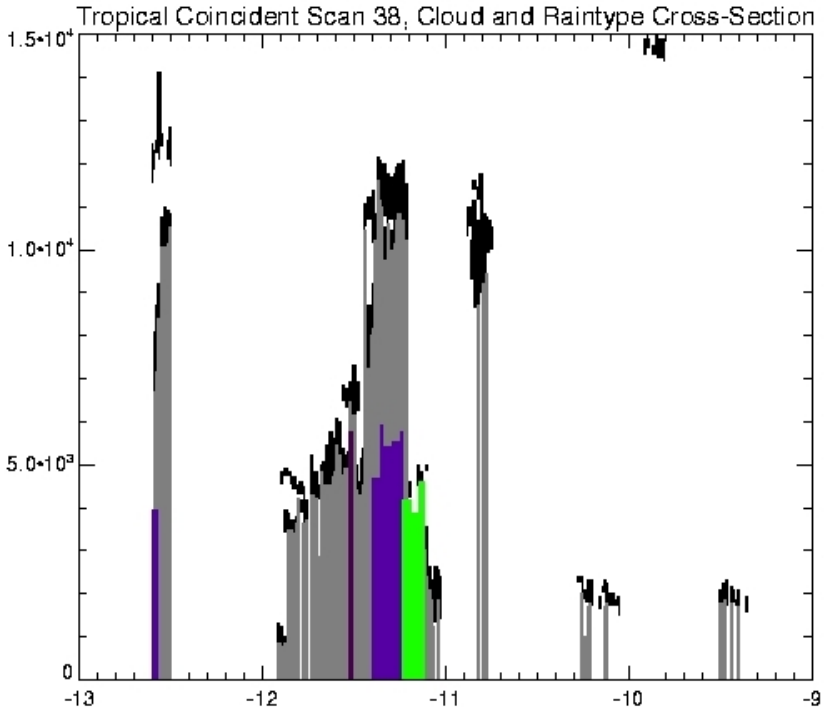

Coincident Scan 39:
GLAS orbital file GLA09_026_2103_002_0351_0_01_0001.DAT
TRMM orbital file 2A23.031114.34195.6.HDF

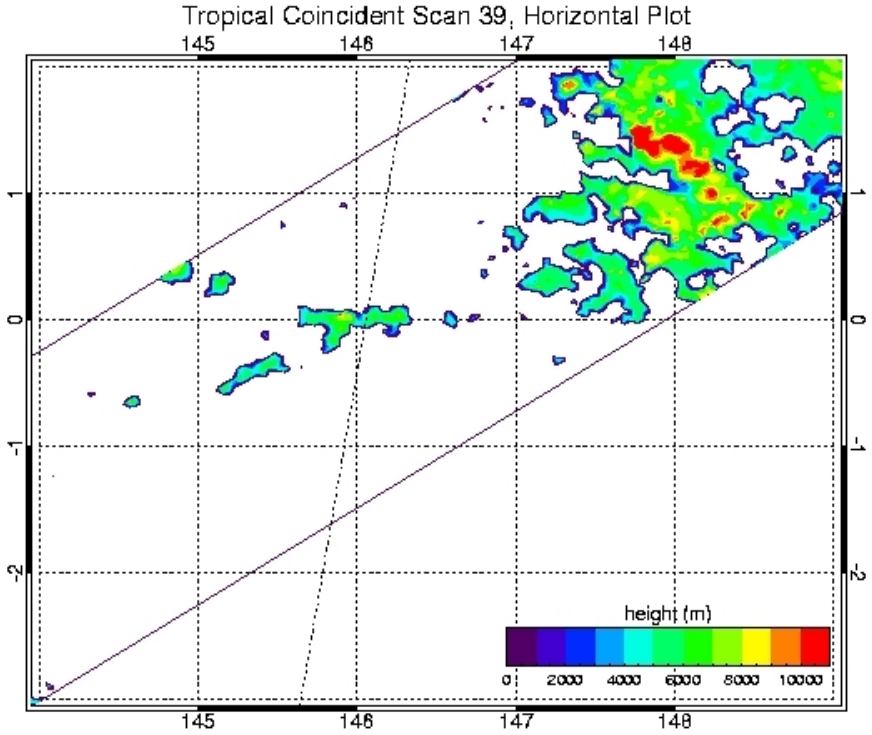

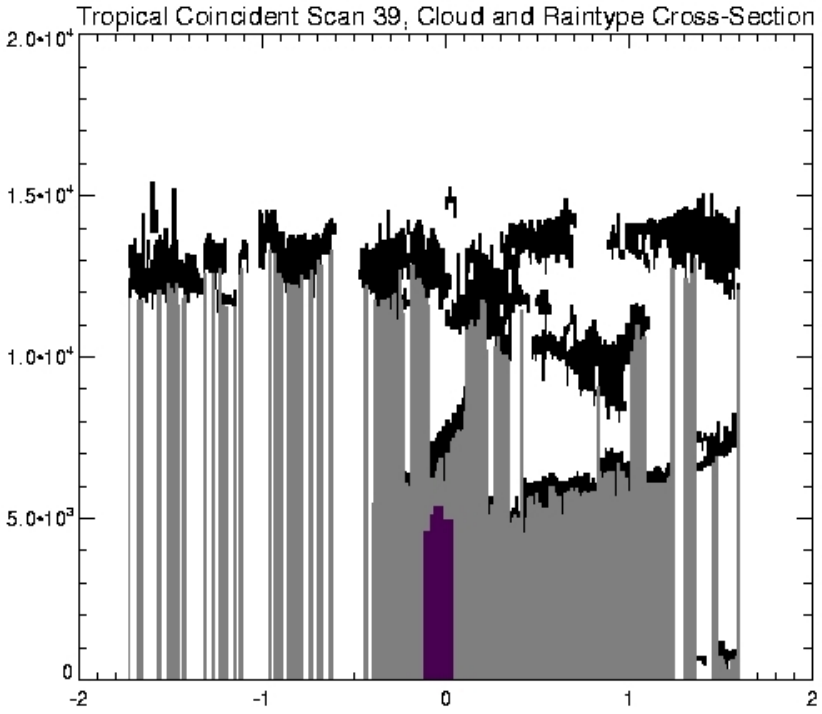

Coincident Scan 40:
GLAS orbital file GLA09_026_2103_002_0351_0_01_0001.DAT
TRMM orbital file 2A23.031115.34196.6.HDF

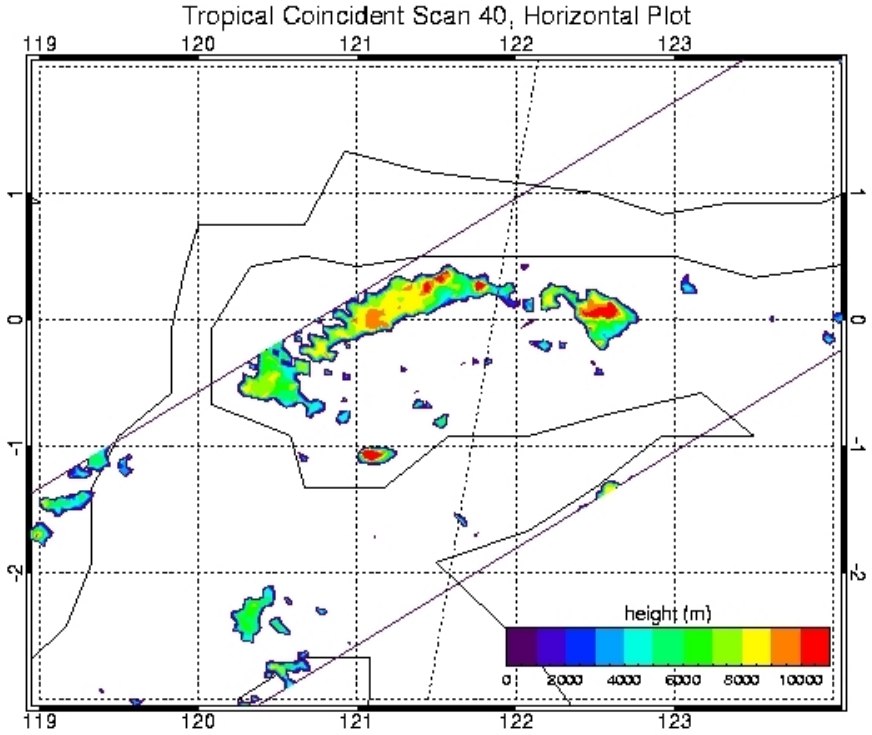

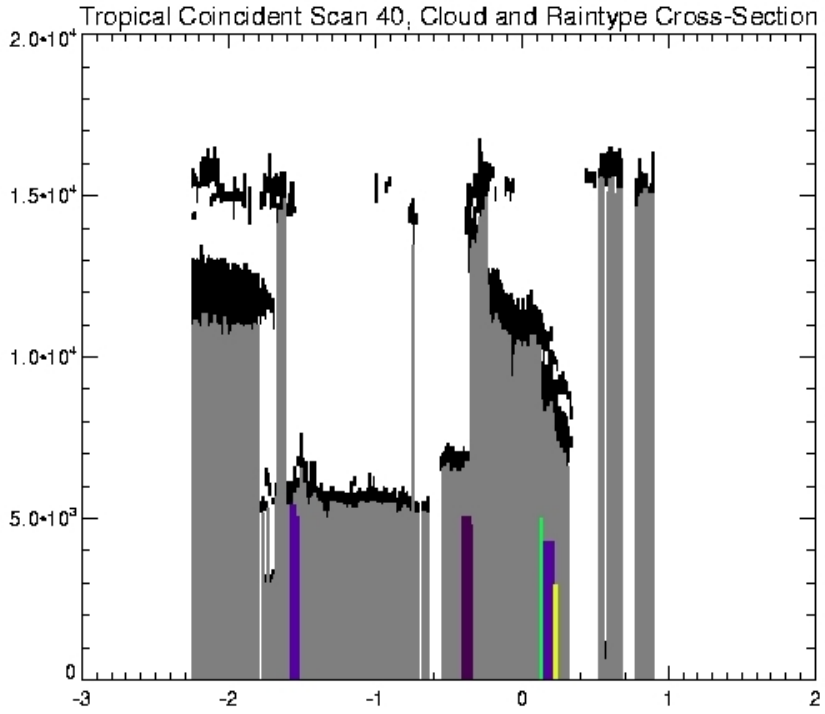

Coincident Scan 41:
GLAS orbital file GLA09_026_2103_002_0351_0_01_0001.DAT
TRMM orbital file 2A23.031115.34196.6.HDF

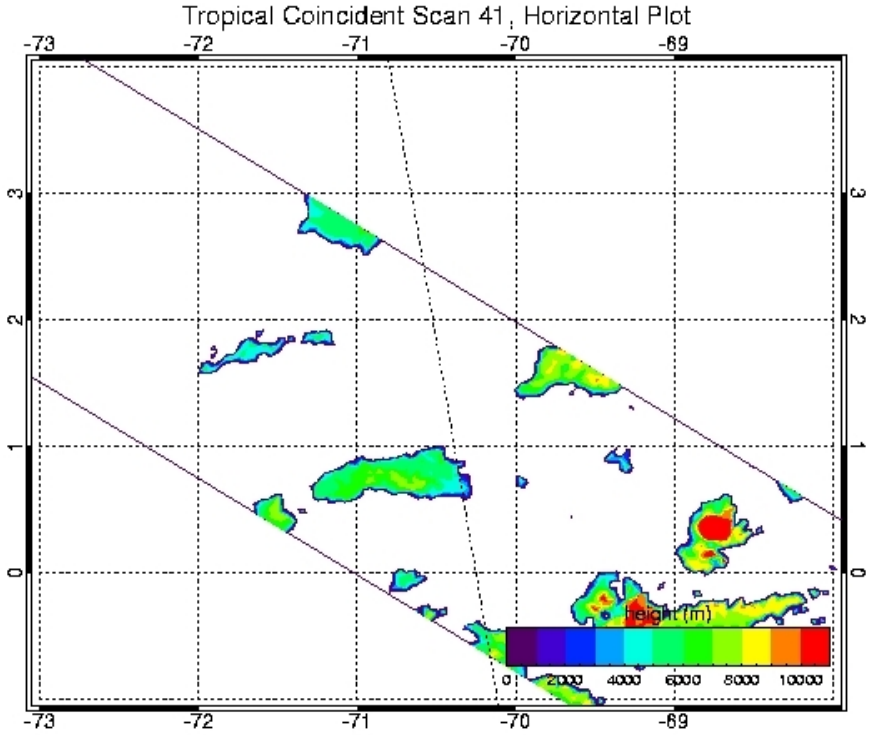

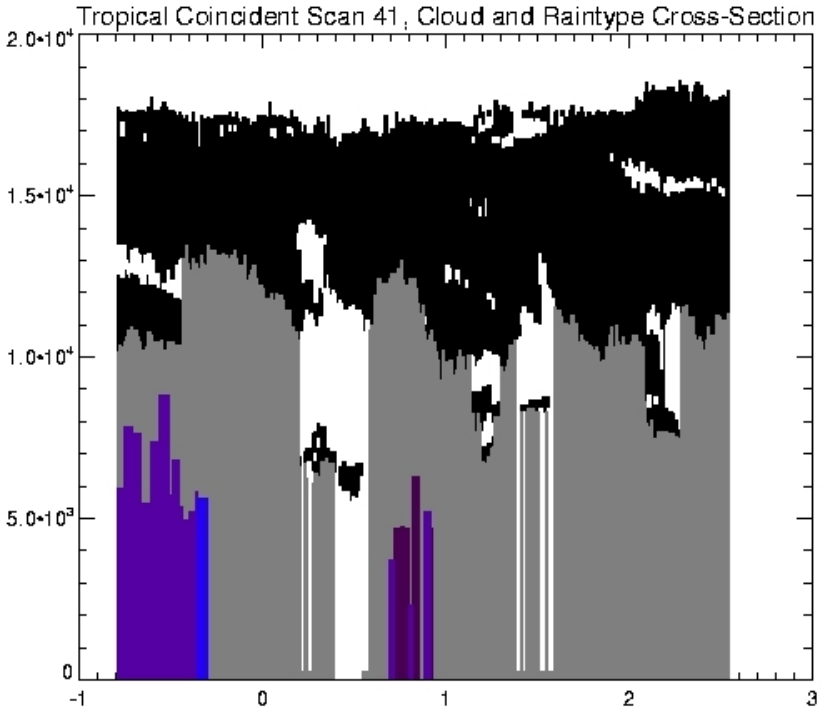

Coincident Scan 42:
GLAS orbital file GLA09_026_2103_002_0351_0_01_0001.DAT
TRMM orbital file 2A23.031115.34197.6.HDF

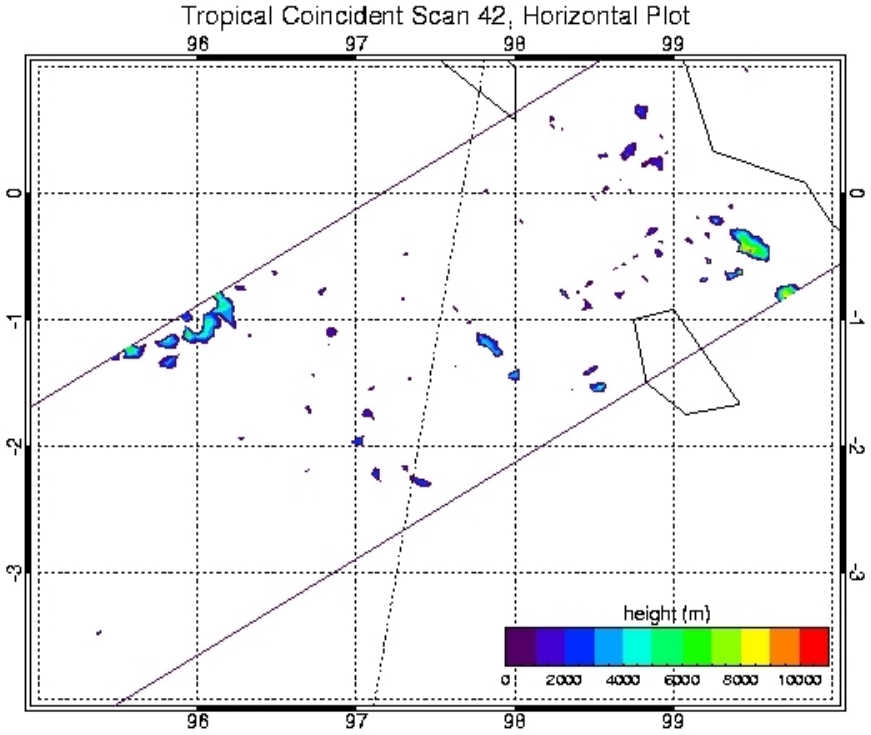

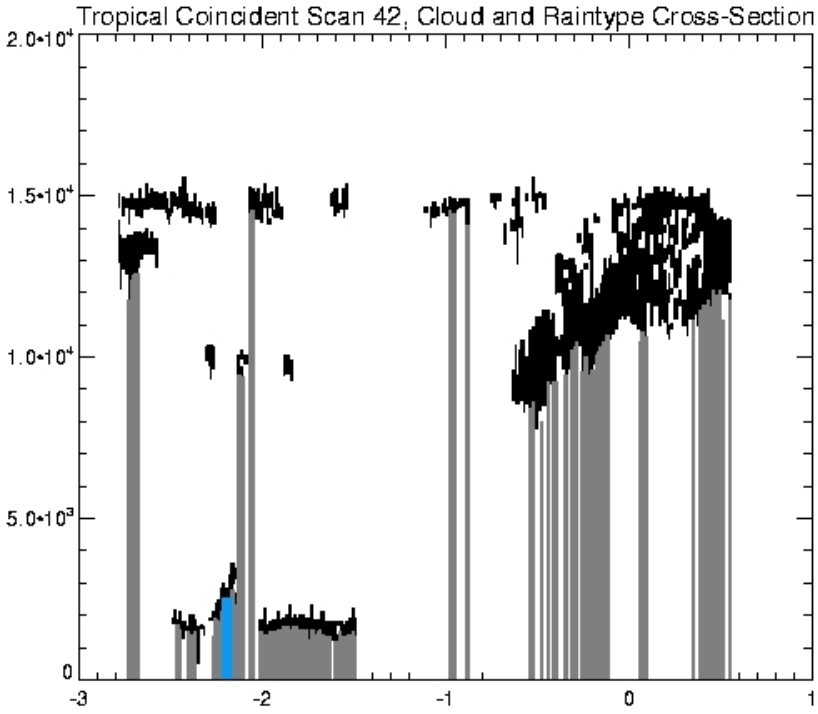

Coincident Scan 43:
GLAS orbital file GLA09_026_2103_002_0351_0_01_0001.DAT
TRMM orbital file 2A23.031115.34198.6.HDF

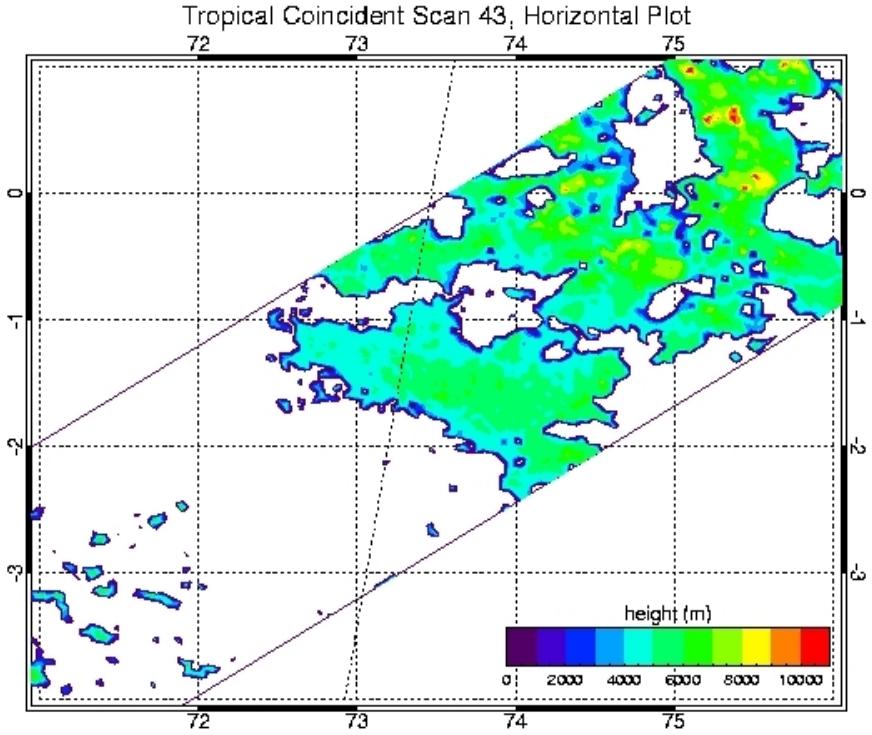

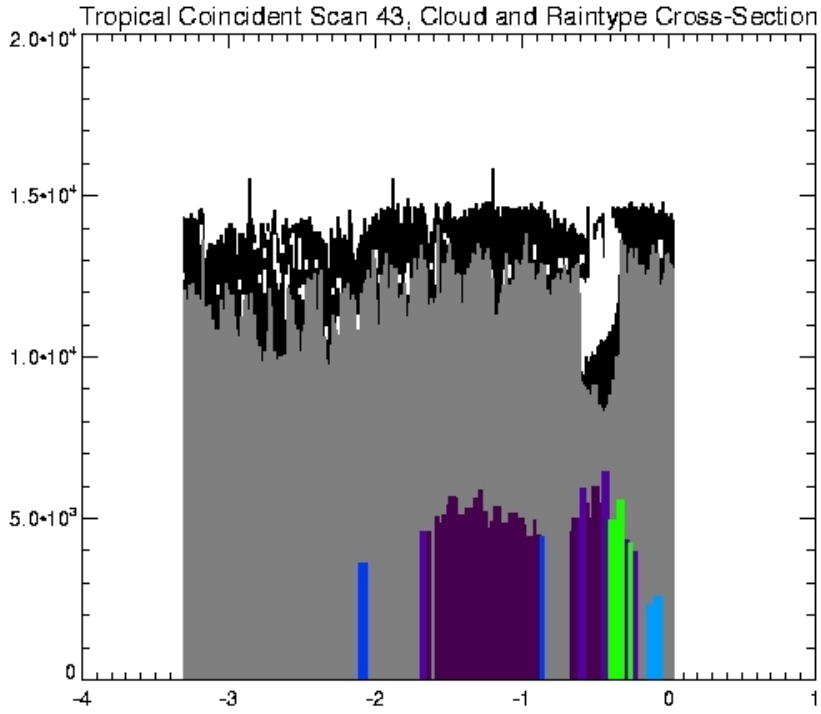

Coincident Scan 44:
GLAS orbital file GLA09_026_2103_002_0351_0_01_0001.DAT
TRMM orbital file 2A23.031115.34200.6.HDF

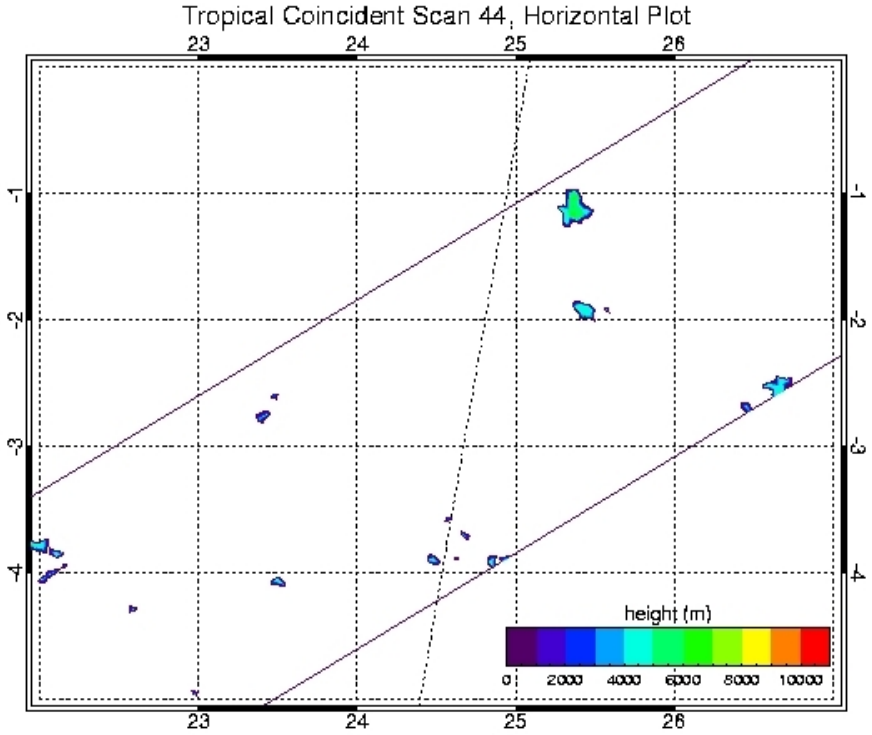

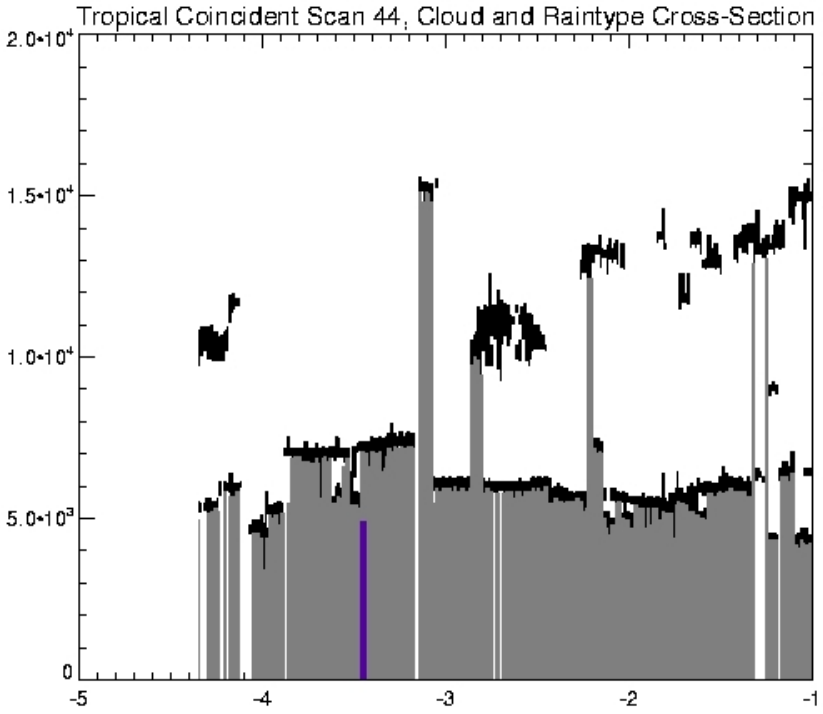

Coincident Scan 45:
GLAS orbital file GLA09_026_2103_002_0379_0_01_0001.DAT
TRMM orbital file 2A23.031116.34219.6.HDF

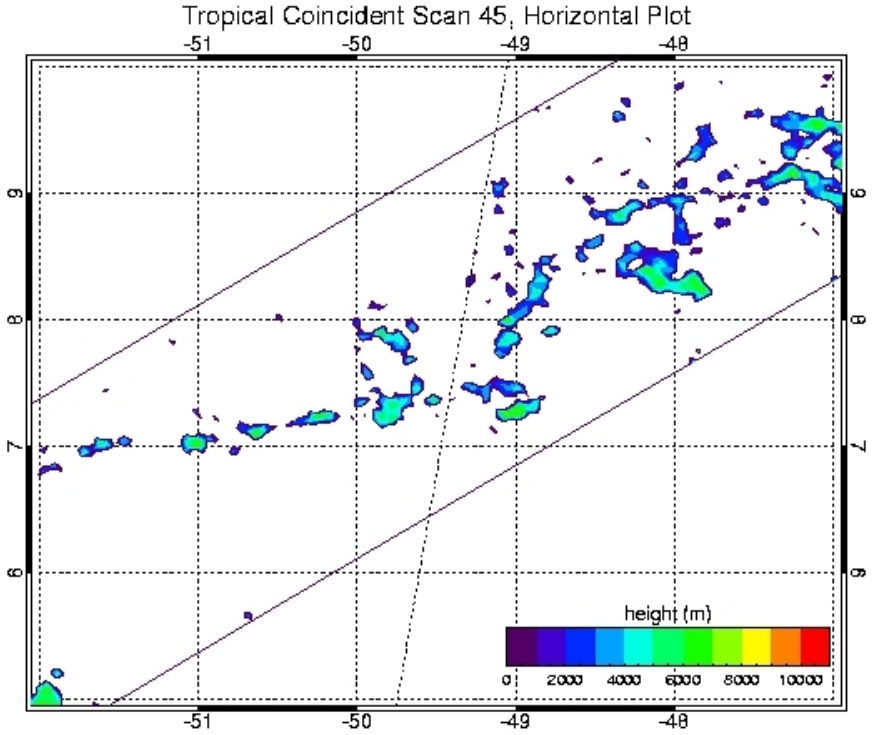

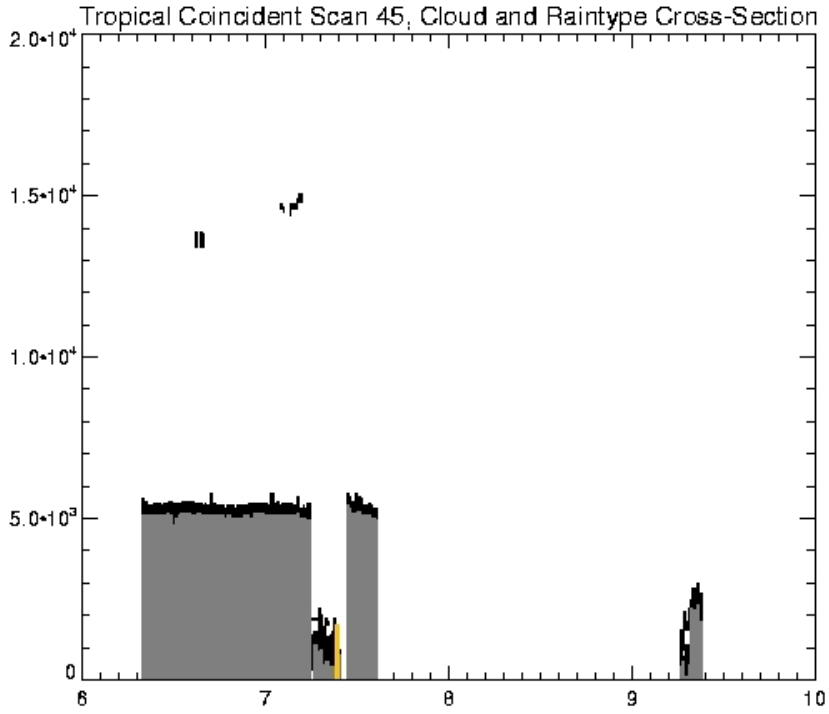

Coincident Scan 46:
GLAS orbital file GLA09_026_2103_002_0379_0_01_0001.DAT
TRMM orbital file 2A23.031116.34219.6.HDF

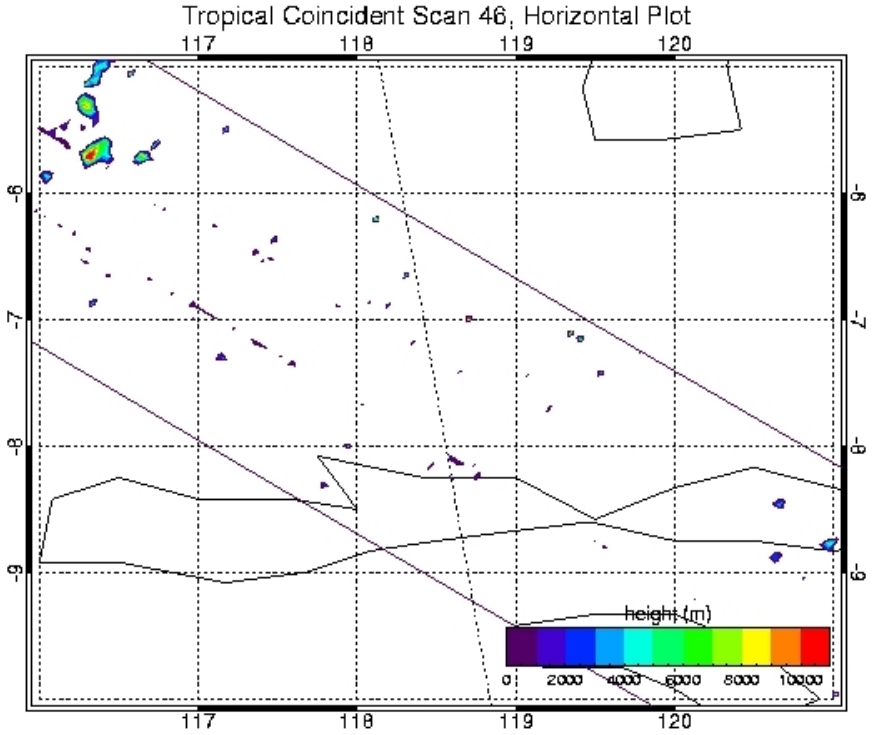

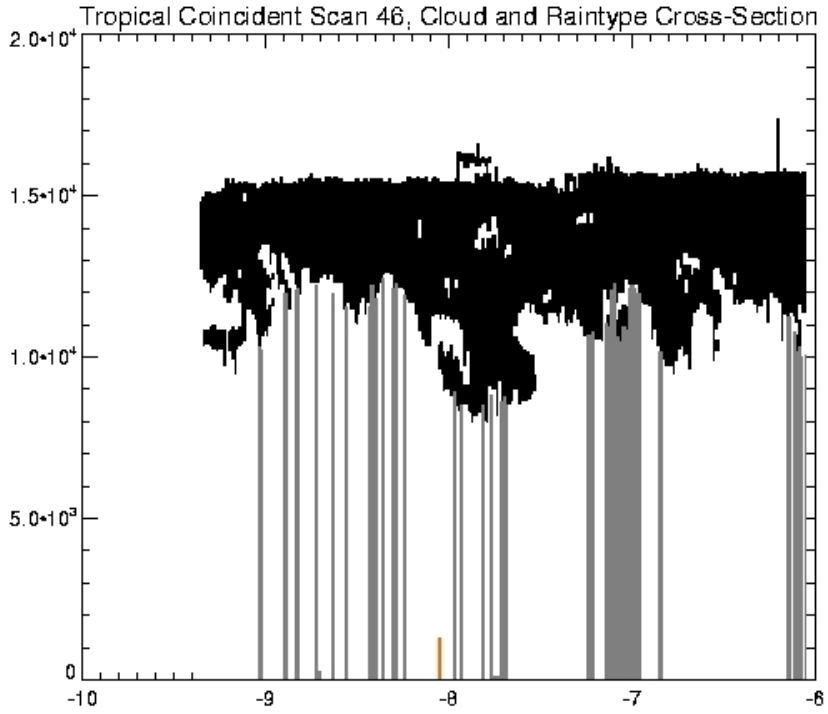

Coincident Scan 47:
GLAS orbital file GLA09_026_2103_002_0379_0_01_0001.DAT
TRMM orbital file 2A23.031116.34219.6.HDF

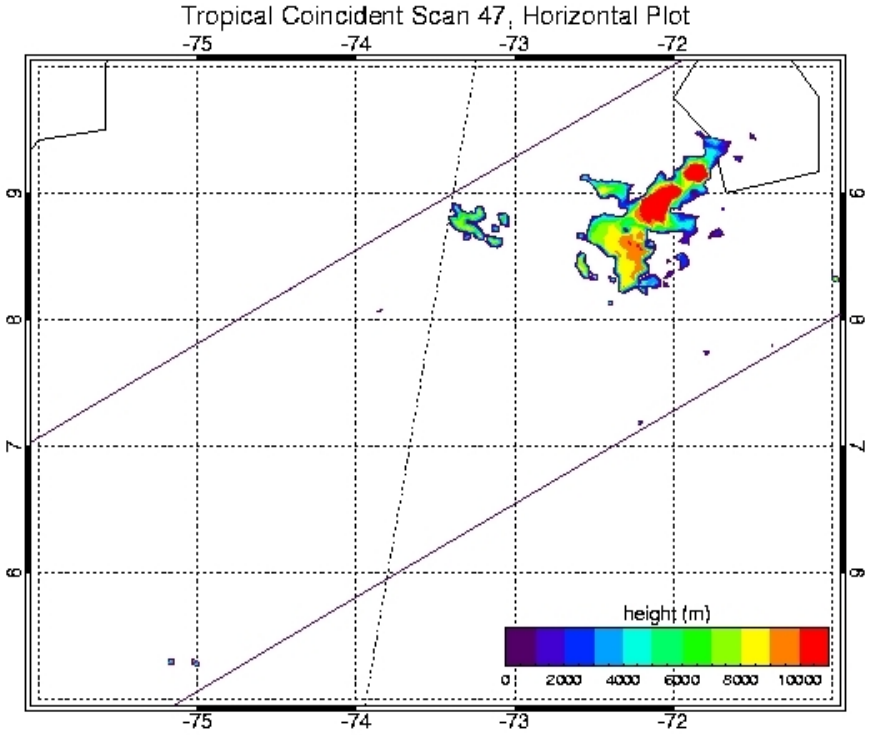

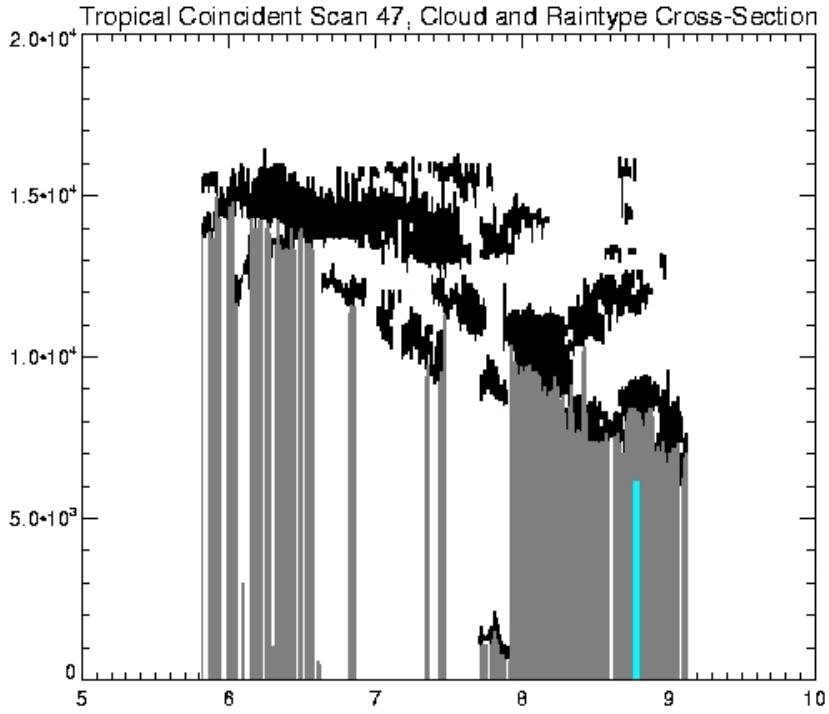

Coincident Scan 48:
GLAS orbital file GLA09_026_2103_002_0379_0_01_0001.DAT
TRMM orbital file 2A23.031116.34221.6.HDF

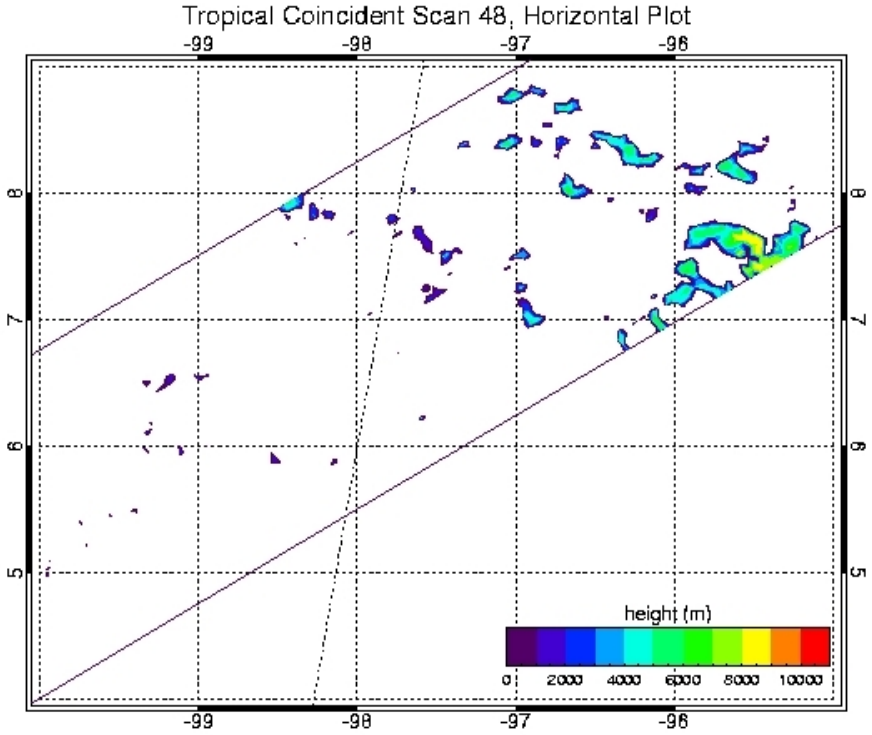

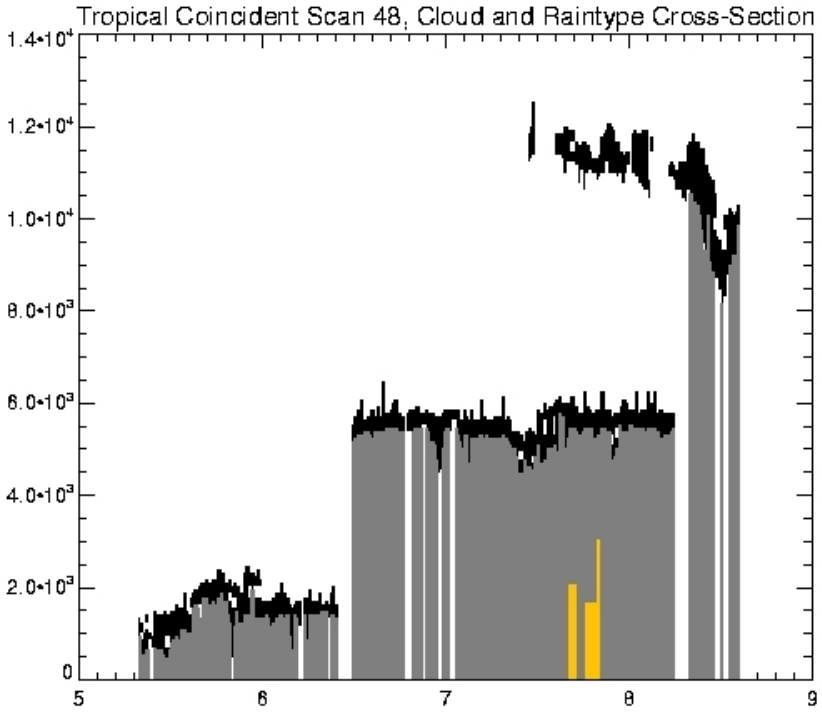

Coincident Scan 49:
GLAS orbital file GLA09_026_2103_002_0379_0_01_0001.DAT
TRMM orbital file 2A23.031116.34223.6.HDF

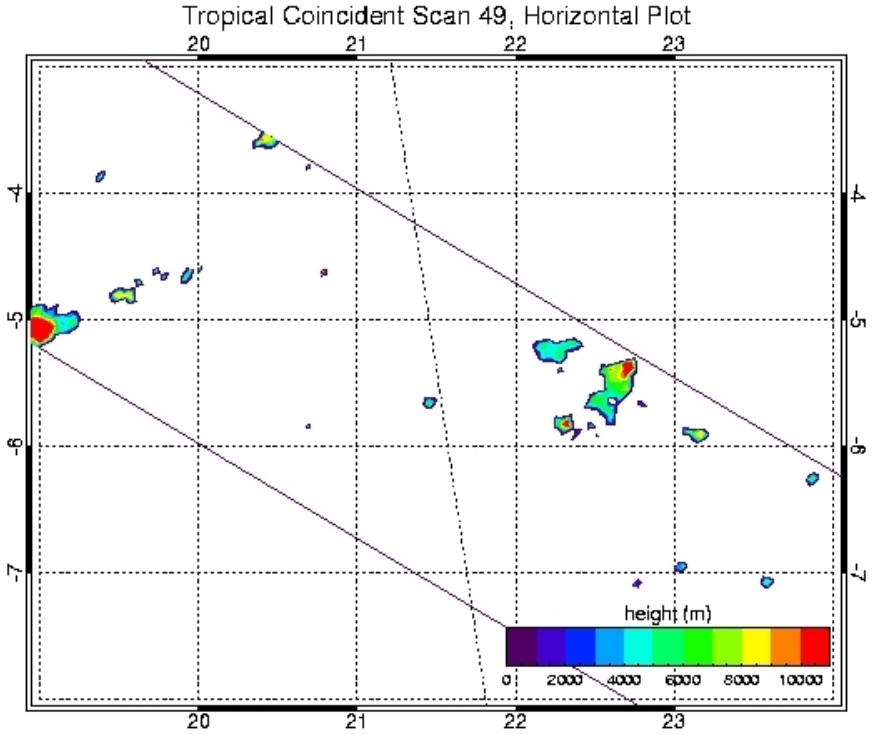

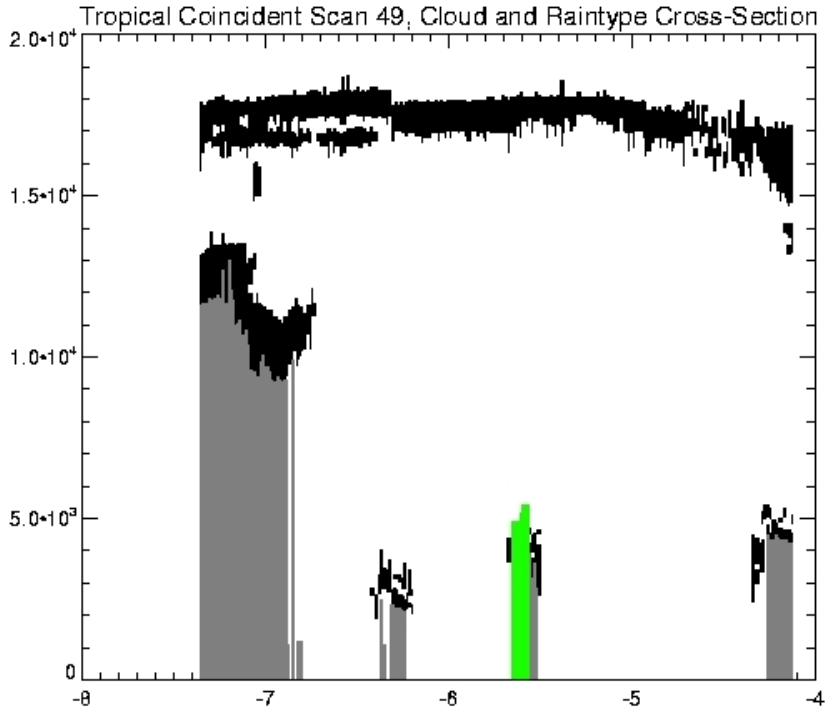

Coincident Scan 50:
GLAS orbital file GLA09_026_2103_002_0379_0_01_0001.DAT
TRMM orbital file 2A23.031116.34225.6.HDF

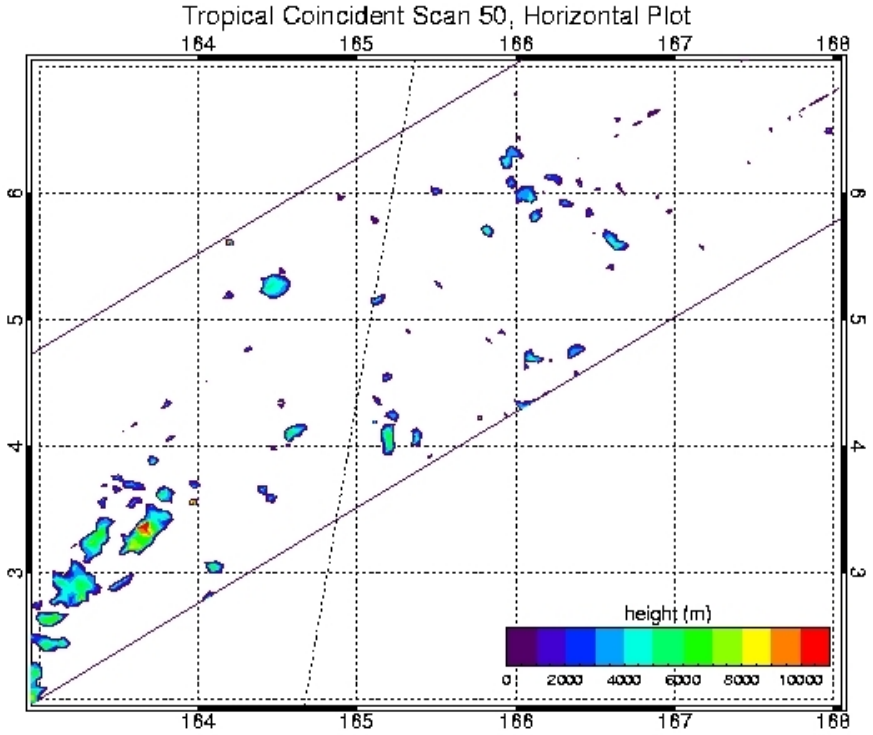

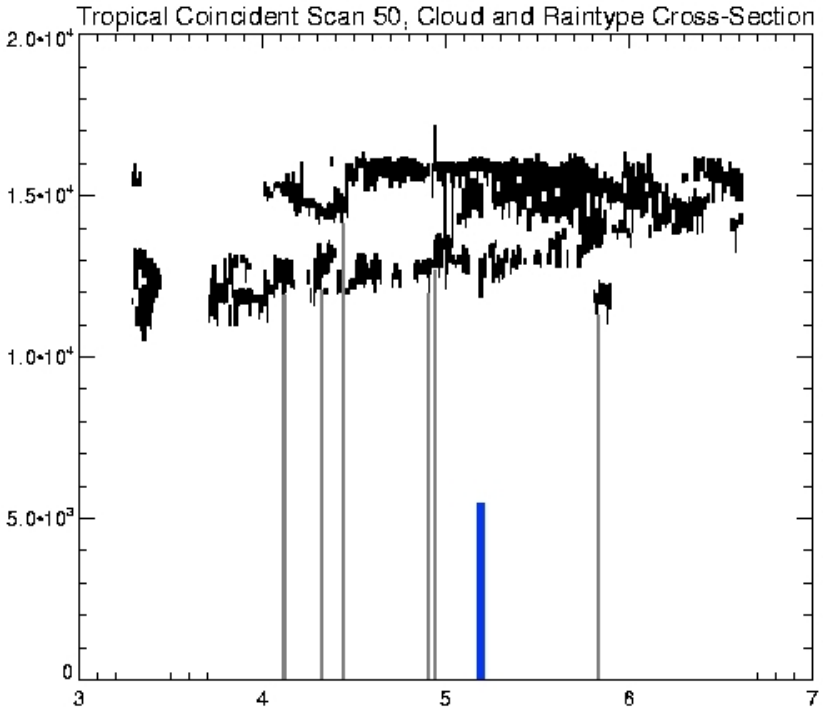

Coincident Scan 51:
GLAS orbital file GLA09_026_2103_002_0407_0_01_0001.DAT
TRMM orbital file 2A23.031118.34245.6.HDF

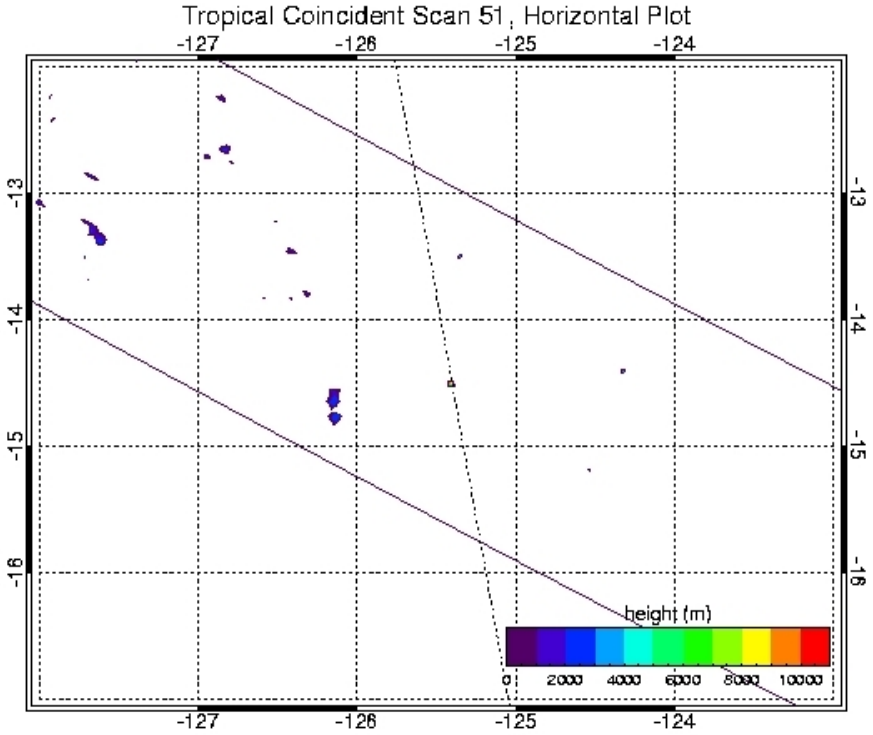

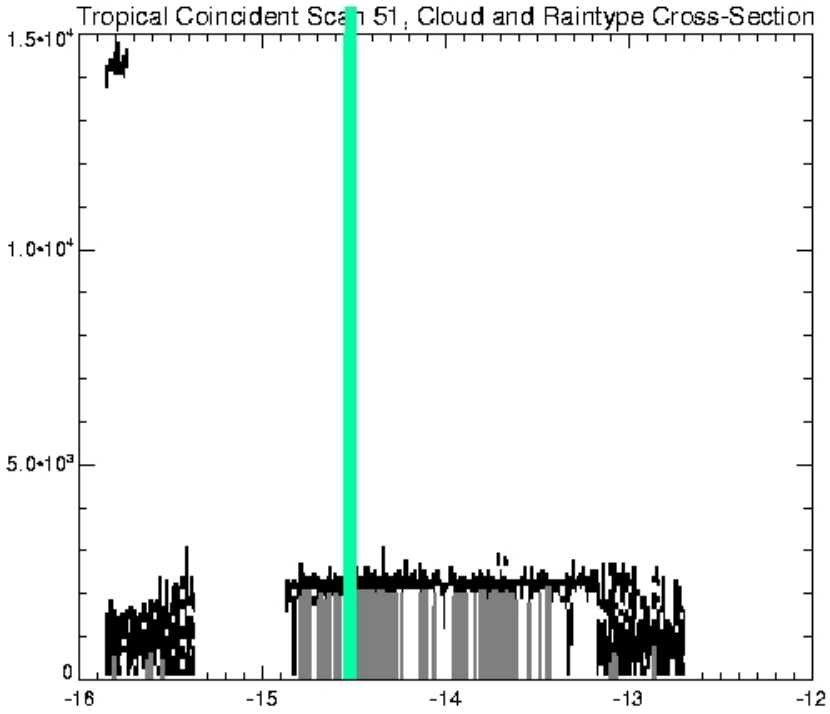

Coincident Scan 52:
GLAS orbital file GLA09_026_2103_002_0407_0_01_0001.DAT
TRMM orbital file 2A23.031118.34247.6.HDF

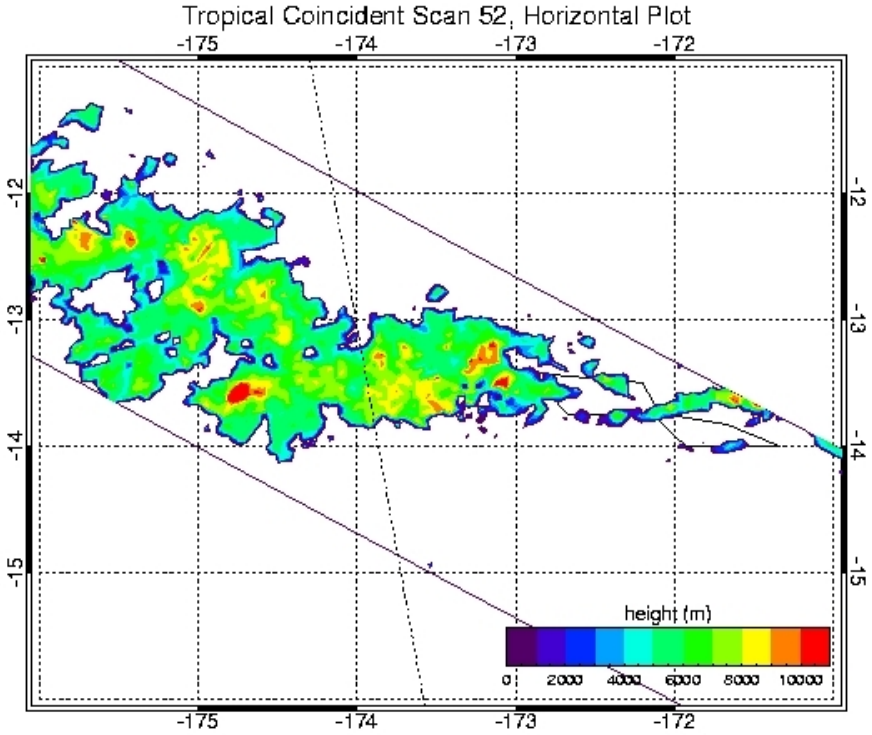

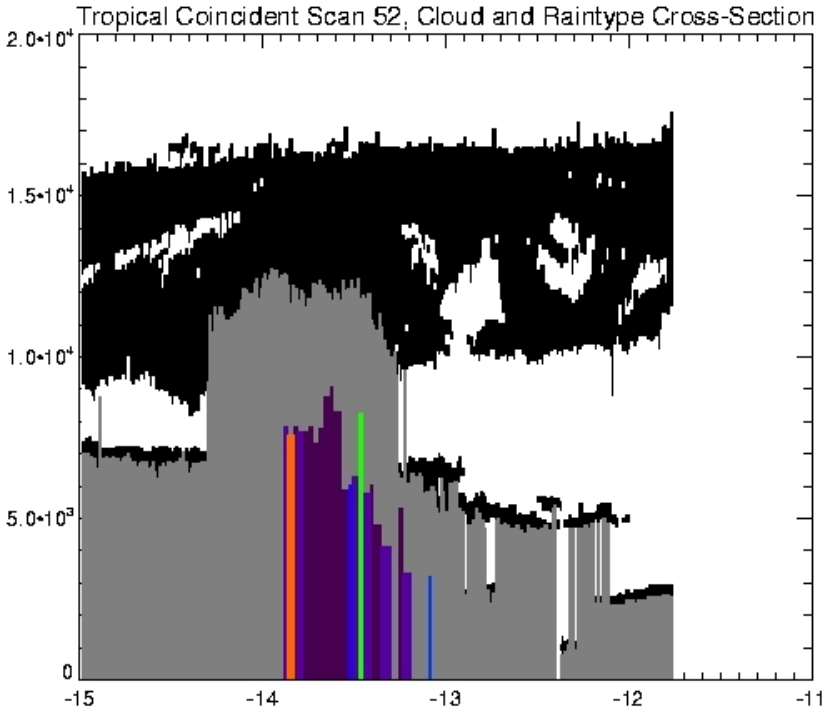

Coincident Scan 53:
GLAS orbital file GLA09_026_2103_002_0407_0_01_0001.DAT
TRMM orbital file 2A23.031118.34248.6.HDF

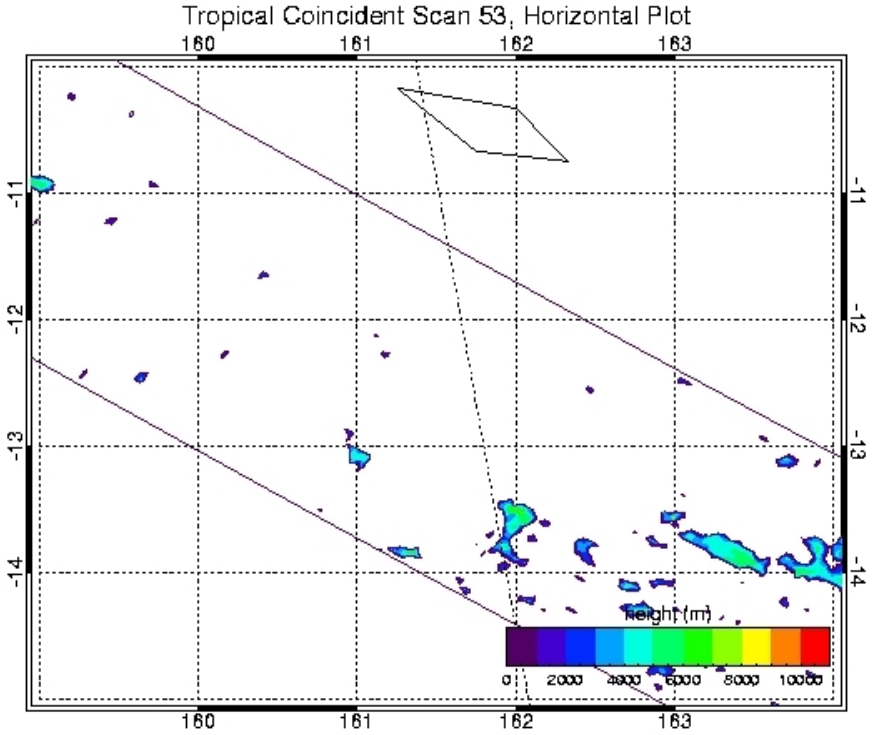

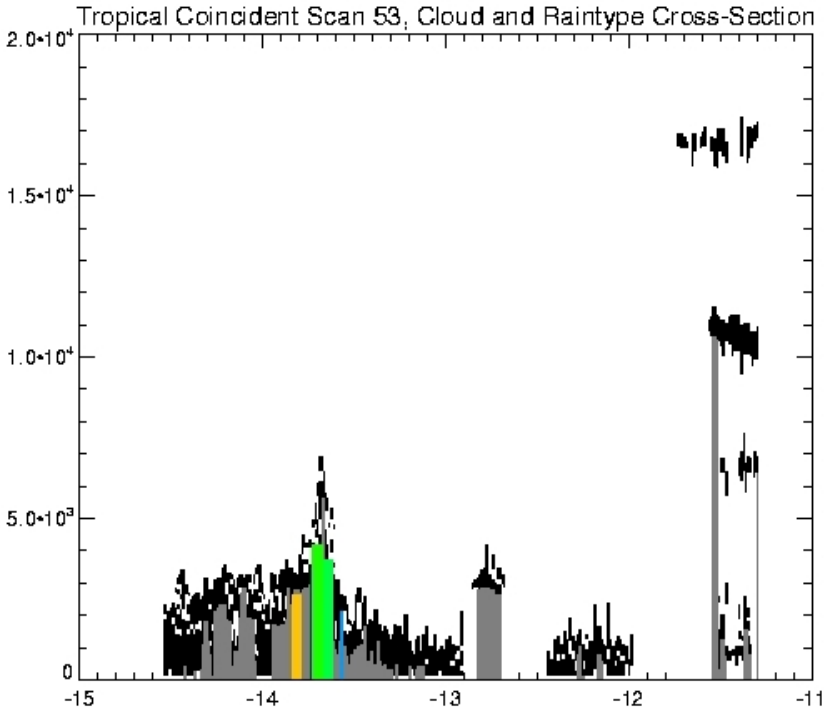

VITA

Name:	Sean Patrick Casey
Address:	Department of Atmospheric Sciences, Texas A&M University, 3150 TAMU, College Station, TX 77843-3150
Email Address:	scasey@ariel.met.tamu.edu
Education:	B.S., Atmospheric Sciences, University of Washington, 2005 M.S., Atmospheric Sciences, Texas A&M University, 2007